Fall 2017

Atomic/molecular layer deposition prepared size-selective catalysts and supported nickel catalysts

Zeyu Shang

ATOMIC/MOLECULAR LAYER DEPOSITION PREPARED SIZE-SELECTIVE

CATALYSTS AND SUPPORTED NICKEL CATALYSTS

by

ZEYU SHANG

A DISSERTATION

Presented to the Faculty of the Graduate School of the

MISSOURI UNIVERSITY OF SCIENCE AND TECHNOLOGY

In Partial Fulfillment of the Requirements for the Degree

DOCTOR OF PHILOSOPHY

in

CHEMICAL ENGINEERING

2017

Approved by:

Dr. Xinhua Liang, Advisor
Dr. Douglas Ludlow
Dr. Manashi Nath
Dr. Ali Rownaghi
Dr. Joseph Smith

PUBLICATION DISSERTATION OPTION

This dissertation consists of the following five articles that have been published or submitted for publication:

Paper I, Pages 17-28, "Encapsulation of supported metal nanoparticles with an ultra-thin porous shell for size-selective reactions" has been published in ***Chemical Communications*** 49(86): 10067-10069, 2013.

Paper II, Pages 29-58, "'Core−shell' nanostructured supported size-selective catalysts with high catalytic activity" has been published in ***Nano Letters*** 17(1): 104-109, 2017.

Paper III, Pages 59-78, "Chemoselective transfer hydrogenation of nitroarenes catalyzed by highly dispersed, supported nickel nanoparticles" has been published in ***ACS Catalysis*** 5(8): 4814-4818, 2015.

Paper IV, Pages 79-120, "Highly active and stable alumina supported nickel nanoparticle catalysts for dry reforming of methane" has been published in ***Applied Catalysis B: Environmental*** 201: 302-309, 2017.

Paper V, Pages 121-145, "Nano-engineered nickel catalysts supported on 4-channel α-Al_2O_3 hollow fibers for dry reforming of methane" was submitted to ***AIChE Journal***.

ABSTRACT

Heterogeneous catalysts are widely used because of their many advantages. In this dissertation, the application of atomic/molecular layer deposition (ALD/MLD) in heterogeneous catalyst synthesis and modification was examined.

A novel nanostructured size-selective catalyst was synthesized by depositing ultra-thin porous shells on the surface of catalysts. The ultra-thin porous shells were formed by oxidation of aluminum alkoxide films deposited by MLD. The catalytic activity of the size-selective catalyst was improved by introducing gaps between the porous shell and catalytic metal nanoparticles. The introduction of gaps greatly reduced the catalyst activity loss, which resulted from the contact areas between the active sites and porous shells.

Ni nanoparticles supported by silica gel particles were prepared by ALD, and the catalyst showed both high activity and selectivity in catalyzing chemoselective transfer reduction of different nitroarenes to produce corresponding aromatic amines.

A highly stable and active Ni/γ-Al$_2$O$_3$ catalyst was synthesized by depositing Ni nanoparticles on porous γ-Al$_2$O$_3$ particles by ALD. The catalyst showed exceptionally high catalytic activity and excellent stability for dry reforming of methane (DRM) reaction. A 4-channel α-Al$_2$O$_3$ hollow fiber was also studied as a support for Ni nanoparticles. The Ni/α-Al$_2$O$_3$ hollow fiber catalyst showed excellent performance in catalyzing the DRM reaction. The performance of the catalyst was further improved by alumina ALD overcoating on Ni nanoparticle surface to increase Ni-support interaction.

ACKNOWLEDGMENTS

I am very grateful to my PhD advisor, Dr. Xinhua Liang, for his guidance, dedication, and patience. The results obtained during this PhD dissertation would not be possible without the discussions we have had and the knowledge that he shared with me. It has been my greatest honor to work with him, an outstanding expert in atomic/molecular layer deposition and heterogeneous catalysis. I also would like to thank him for giving me the chance to participate in scientific conferences to present my research results.

I sincerely thank the rest of my committee members, Dr. Douglas Ludlow, Dr. Manashi Nath, Dr. Ali Rownaghi, and Dr. Joseph Smith, for their excellent suggestions. I would like to acknowledge Dr. Eric Bohannan for XRD analysis, Mr. Brian Porter for XPS analysis, and Dr. Jessica TerBush and Dr. Clarissa Weisner for TEM analysis.

I would like to thank the technician, Mr. Dean Lenz, and staff in the Chemical and Biochemical Engineering Department for their help during my PhD studies at Missouri S&T. I also greatly appreciate the help and kind support from my colleagues in Dr. Liang's group and my friends.

My greatest gratitude is given to my family for their continual encouragement and support through my PhD process, and in the rest of my life. Last but not least, I would like to thank Han Zhang, the love of my life. Her appearance in my life makes me the happiest man in the world. I dedicate this work to her as she always encourages me to be a better man, and to never give up.

TABLE OF CONTENTS

LIST OF ILLUSTRATIONS

LIST OF TABLES

1. INTRODUCTION

1.1. ATOMIC LAYER DEPOSITION

Atomic layer deposition (ALD) is a gas-phase thin film deposition technique with a subnanometer thickness control. ALD was called atomic layer epitaxy (ALE) before the year of 2000.[1-3] Suntola et al.[4] and Aleskovskii et al.[5] are considered the ALD developers, and the ALD technique was patented by Suntola et al. in 1977.[4]

1.1.1. Fundamentals of Atomic Layer Deposition. Different from other deposition techniques [e.g., chemical vapor deposition (CVD) and physical vapor deposition (PVD)], ALD relies on sequential binary, self-limiting gas-solid surface reactions, and the gas phase precursors were introduced into the deposition reactor alternately. The exposure steps of different precursors were separated by a purging step to prevent the gas-phase reaction between the precursors. In each precursor exposure step, gas precursor molecules could react with the substrate surface sites until the surface is saturated with new functional groups. Since there is only a limited number of active sites on the substrate and the precursor cannot react with the newly formed surface species, only a monolayer of surface species could form through the reaction of precursor and the substrate surface sites. Therefore, the reaction process is self-limiting, which is the reason why the deposited film thickness could be controlled in a molecular level by ALD. Even though ALD was first applied to deposit thin films on flat surfaces, it has been successfully employed to uniformly deposit conformal films on high aspect ratio structures.

The desired film thickness could be achieved by repeating ALD coating cycles. Typically, one ALD coating cycle consists of four steps: (1) exposing the substrates to the first precursor, (2) vacuuming the reactor to purge out the first precursor, (3) exposing the substrates to the second precursor, and (4) vacuuming the reactor. These four steps referred to one "ALD cycle". Figure 1.1 schematically shows the Al_2O_3 ALD process. The two precursors for Al_2O_3 ALD are trimethylaluminum (TMA) and water. TMA can react with water to form Al_2O_3, described by the following reaction:[6]

$$2Al(CH_3)_3 + 3H_2O \rightarrow Al_2O_3 + 6CH_4 \tag{1}$$

In Al_2O_3 ALD, this reaction is divided into two half-reactions, listed as follows:[7]

$$\text{-OH}^* + Al(CH_3)_3 \rightarrow \text{-OAl(CH}_3)_2^* + CH_4 \tag{2}$$

$$\text{-OAlCH}_3^* + H_2O \rightarrow \text{-OAlOH}^* + CH_4 \tag{3}$$

where the asterisks (*) indicates the surface species. Typically, the substrate surface is covered by some functional groups, such as hydroxyl (-OH) groups. In the first half-reaction, the substrate surface is exposed to TMA molecules and they are adsorbed on the substrate surface and react with the surface -OH groups. The O-H bond will be replaced by an O-Al bond, CH_4 will be produced as a by-product, and -CH_3 surface groups will form. The reaction process will continue until all the surface -OH groups reacted with TMA precursors, and the substrate surface will be saturated with -CH_3 groups. Since only limited number of -OH groups on the substrate surface, the gas-solid surface reaction is self-limiting. The following purging process removes any by-product and unreacted precursors. In the second half-reaction, the substrate surface is exposed to the second precursor, water

vapor, which can react with the $-CH_3$ surface groups. In this half-reaction, all $-CH_3$ surface groups are removed, the $-OH$ surface groups are regenerated, and CH_4 is produced as by-product. The second half-reaction is also self-limiting. The followed evacuation process can remove all unreacted precursors and any by-products. One conformal layer of Al_2O_3 film with a thickness of ~0.1 nm can be deposited after one cycle of alumina ALD applied.
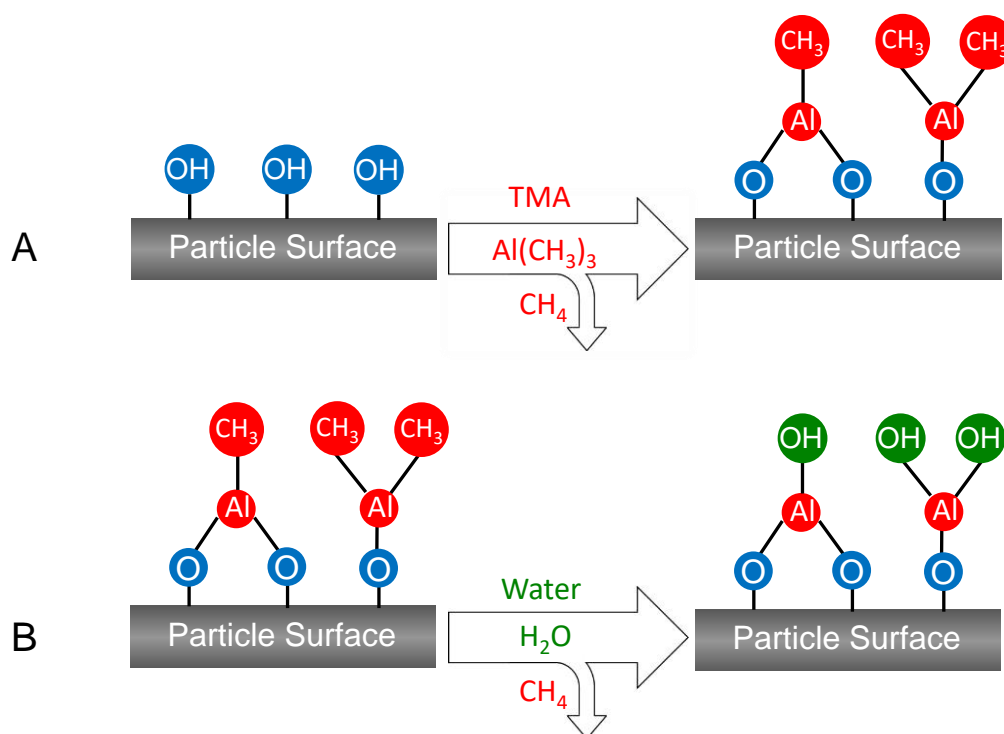
Figure 1.1. Schematic representation of one cycle of Al_2O_3 ALD using TMA and water as precursors.

After one cycle of Al_2O_3 ALD, the surface -OH groups can be regenerated, which can be employed for more cycles of ALD. ALD has been employed in a wide range of research fields and industrial applications, such as batteries,[8, 9] fuel cells,[10, 11] semiconductors,[12, 13] and catalysis.[14-16]

1.1.2. Thin Film Coating by ALD. ALD film components are determined by both precursors. Different metal-containing films can be deposited by employing different precursors. Organometallic and halide metallic compounds are widely employed as the ALD first precursors. The metal oxide ALD films can be deposited using water as the second precursor. For example, TMA and water are employed as precursors for alumina ALD, and titanium tetrachloride and water can be used as precursors for titania ALD.[17, 18] Phosphine can be employed to deposit metal phosphide films as the second precursor. For example, gallium phosphide film can be deposited using trimethylgallium and phosphine as precursors. Hydrogen sulfide and ammonia were employed as the second precursor to deposit metal sulfide and metal nitride films, respectively.[19, 20]

Different metal thin films can also be deposited using different precursors. There are three main mechanisms employed for metal ALD. These mechanisms are based on fluorosilane elimination, combustion, and hydrogen reduction. Metal tungsten film was successfully deposited based on the fluorosilane elimination mechanism using tungsten hexafluoride and disilane as precursors.[21] Some metal films (e.g., ruthenium[22] and platinum[23]) can be deposited based on a combustion mechanism using organometallic compound and oxygen as precursors. Organometallic precursors and hydrogen were

successfully employed to deposit iron, cobalt, nickel, and copper metal films according to the hydrogen reduction chemistry.[24]

1.1.3. Metal Nanoparticles by ALD. The layer-by-layer deposition fashion of ALD could yield uniform and smooth films, such as alumina. However, the deposition may not be uniform due to the lack of active surface sites on the starting substrate or aggregation of the deposited materials. These mechanisms have been used to deposit noble metal nanoparticles on oxide surfaces using ALD.[25-28] Small and highly dispersed noble metal nanoparticles (e.g., Pd,[29, 30] Ru,[30] and Pt[31, 32]) were successfully synthesized by ALD as catalysts with considerably high activity. Some other transition metal nanoparticles (e.g., Ni[33] and Co[34]) were also successfully synthesized by ALD and employed as catalysts for different reactions.

1.2. MOLECULAR LAYER DEPOSITION

Similar to ALD, molecular layer deposition (MLD) is a layer-by-layer, self-limiting gas phase thin film coating technique. The precursors of MLD contain some organic components, which can be part of the deposited films. Therefore, MLD was employed to deposit organic or hybrid organic-inorganic films, and the film thickness can be precisely controlled in nanometers.[35-37] The organic polymer MLD films deposition process was first developed by researchers in Japan.[37, 38]

1.2.1. Dense Film Coating by MLD. Different polymer (e.g., polyamide,[39] polyurea,[40] polyurethane,[41] polyimide[42, 43], and polyazomethine[44]) films were successfully

deposited by MLD. Acyl chlorides and amines were employed as precursors for different polyamide MLD.[35, 45] For example, Nylon 66 film was deposited using adipoyl chloride and 6-hexanediamine as precursors by MLD.[35] Ethylenediamine and 1,4-phenylene diisocyanate were employed as precursors for ployurea MLD.[40] Lee et al.[41] demonstrated the MLD deposition of polyurethane using 1,4-phenylene diisocyanat and 2-butyne-1,4-diol. Polyimides MLD using pyromellitic dianhydride and different diamines[42, 43] and polyazomethine MLD using terephthalaldehyde and p-phenylenediamine as precursors were also developed.[44]

Additionally, the hybrid organic-inorganic MLD has been successfully demonstrated using an inorganic precursor and an organic precursor.[46] Aluminum alkoxide (alucone) MLD was first realized using TMA and ethylene glycol as precursors.[36] A lot of other metal alkoxide films were also realized by MLD, such aszinc alkoxide (zincone) MLD using diethyl zinc and ethylene glycol as precursors.[47, 48]

1.2.2. Ultra-Thin Porous Films Synthesis by Oxidation of Hybrid Films Deposited by MLD. Hybrid organic-inorganic alucone MLD films were successfully employed to form microporous-mesoporous films by removing the organic component inside the hybrid films.[49, 50] The organic components in the MLD film can be removed ether by mild water etching or high-temperature calcination in air.[49] Liang et al.[49] demonstrated that 50 cycles of alucone MLD could result in an 8 nm thick porous film, and the film thickness could be precisely controlled down to subnanometer by applying different MLD cycles. The pore size in the porous film can be tuned by choosing different MLD precursors

and varying oxidation conditions. The porous alumina shell synthesized by MLD was successfully employed to improve the stability of metal nanoparticles supported on different substrates.[51, 52]

1.3. SIZE-SELECTIVE REACTIONS

Size-selective catalysis, also called shape-selective catalysis, is different from traditional selective catalysis, which is mainly due to the interaction between the active sites and reactant molecules or intermediate species. The size-selective catalysis results from the molecular-sieving effect during the reaction where the reactants, products, or the intermediate species are distinguished from their molecular size or shape. The size selectivity can be classified into three different types: reactant size selectivity, product size selectivity, and transition-state size selectivity. Reactant size selectivity is based on the mass transfer limitation of the reactant molecules that limits larger molecules from passing through the pores of the catalyst to reach the active sites. Product size selectivity refers to product molecules mass transfer limitation, where products with larger molecule size can be formed on the active sites, but they are too large to diffuse out of the pores as a product. The transition-state size selectivity is related to the spatial limitation of transition state species that causes the large intermediate species, which cannot fit in the pores, to not form. The size-selective catalysis was exploited in different areas, such as isomerization,[53] hydroxylation,[54] alkylation,[55] and hydrogenation[56].

Zeolite 13X was first employed as a size-selective catalyst in 1960,[57] and more types of molecular sieves (e.g., ferrierite,[58] ZSM-5,[59] and mordenite[55]) were employed as size-selective catalysts afterward. In recent years, non-zeolitic size-selective catalysts were extensively investigated.[60]

Metal nanoparticle catalyst is one important branch of heterogeneous catalysts, and has been employed in hydrogenation, oxidation, combustion, and other areas because of its many advantages, including the ease of separating the catalyst by filtration after a reaction and its reusability.[61-63] However, compared to some other catalysts (e.g., enzyme and organometallic catalysts), it is generally difficult for metal nanoparticles catalysts to selectively convert certain molecules in reactant mixtures to desired products.[64] Many methods, such as modifying the catalyst surface,[65, 66] tuning reaction conditions,[67] and designing enzyme mimics[68] were successfully employed to improve the catalyst selectivity. Another important strategy to improve the catalyst selectivity is to synthesize size-selective or shape-selective catalysts.

One important strategy for designing size-selective catalysts is developing "core-shell" nanostructured catalysts with porous shells encapsulating metal nanoparticles. The porous shell only allows smaller molecules to diffuse through it to realize the size-selectivity. Many methods were applied to synthesize porous shells, and these porous shells were employed to encapsulate different metal nanoparticles catalysts to improve the thermal stability and sintering resistance of the catalysts.[69-71] Mesoporous titania,[72] mesoporous silica,[73, 74] zeolites,[75-77] and metal-organic frameworks (MOFs)[78] have well-

defined porous structures and have been employed to encapsulate metal nanoparticle catalysts. Among them, mesoporous materials are not appropriate for size-selective catalysis of fine chemicals, since the pore sizes are too large. Zeolites and MOFs have inherent micropore systems of molecular dimensions, which allows for size-selective catalysis. For example, Nishiyama et al.[75] synthesized 40 μm thick silicalite-1 zeolite coatings on spherical Pt/TiO_2 particles that were 0.5 mm in diameter for size-selective hydrogenation of 1-hexene over dibranched 3,3-dimethylbut-1-ene. Lu et al.[78] embedded Pt nanoparticles in a zeolitic imidazolate framework (ZIF-8) MOFs with a thickness about 200 nm and demonstrated that the porous shell greatly increased the catalyst selectivity of hydrogenation of n-hexene over cis-cyclooctene. However, the catalyst activity decreased a lot after being encapsulated in the porous shell. This decrease is due to the combined effect of the mass diffusion limitation caused by the relative thick porous shell and blockage of active sites due to the contact areas between the porous shell and the catalytic sites. Li et al.[79, 80] successfully embedded metal nanoparticles into single crystal hollow shells as yolk-shell structured size-selective catalysts with a shell thickness down to 20 nm. However, in all the above mentioned examples, the methods used to synthesize porous coatings were based on liquid-phase methods. It is difficult to apply liquid methods to fabricate porous shell on porous substrates. Therefore, current research activities of size-selective catalysts are mainly focused on encapsulating unsupported or dense substrate-supported metal nanoparticle catalysts. However, the metal nanoparticles are normally dispersed on high surface area supports so that the resulting metal nanoparticles have a

large fraction of their atoms on the surface. It is highly desirable to develop a size-selective

catalyst with high surface area catalyst substrate, ultra-thin and well-defined porous shell,

and few contact areas between the active sites and porous shell. As mentioned earlier, ultra-

thin porous shell with well-defined porous structure was successfully deposited on porous

substrate by oxidation of hybrid MLD films.[51] MLD is an ideal ultra-thin film deposition

technique for porous substrates due to its advantages, such as its self-limiting nature and

gas-phase-based deposition procedure.

1.4. CHEMOSELECTIVE TRANSFER HYDROGENATION OF NITROARENES

Aromatic amines are useful intermediates in the preparation of dyes,

pharmaceuticals, and agricultural chemicals, which can be obtained by the hydrogenation

of aromatic nitro compounds. Different metal catalysts and reducing agents were available

for this purpose. However, the selective reduction of a nitro group in the presence of other

reducible functional groups in a molecule is a challenging task. In addition, reduction of

aromatic nitro compounds often stops at an intermediate stage, yielding hydroxylamines,

hydrazines, azoarenes, or azoxyarenes as by-products.[81-83] Different metal nanoparticles

(e.g., Au,[84] Ag,[85] Fe,[86] Fe-Ni,[87] Ni-B,[88] Ru,[89] and Pd[90]) were employed for the reduction of

nitro groups. Among these catalysts, gold catalysts showed the highest activity and

selectivity. However, gold is very expensive and is relatively rare in the earth's crust. Ni is

also a good catalyst for the reduction of nitroarenes and showed high selectivity toward

aromatic amines. However, the conventional liquid-phase-based methods prepared Ni

catalysts showed much lower activity as compared to gold catalysts. It is desirable to develop an efficient, cost-effective, and chemoselective catalyst for hydrogenation of nitroarenes. Recently, small Ni nanoparticle catalysts were successfully synthesized by the ALD technique and showed excellent performance in propylene hydrogenolysis reactions. It was demonstrated that smaller metal nanoparticles showed higher activity for hydrogenation of nitroarenes.[91] Therefore, it is expected that nickel nanoparticles deposited by ALD would have excellent properties for the reduction of nitro groups.

1.5. DRY REFORMING OF METHANE

Methane, as a major component of natural gas, is released as a waste product or simply burnt off from the petroleum extraction process. However, the emission of methane or carbon dioxide (one combustion product of methane) is harmful to the environment, since both carbon dioxide and methane are greenhouse gases. Therefore, the utilization of methane becomes important. Methane reforming reactions are important applications of methane and widely studied to produce hydrogen and syngas (mixture of carbon monoxide and hydrogen). Two typical methane reforming reactions are methane steam reforming (MSR, $CH_4 + H_2O \rightarrow 3H_2 + CO$) and methane reforming with carbon dioxide ($CH_4 + CO_2 \rightarrow 2H_2 + 2CO$), which is also called dry reforming of methane (DRM). In MSR reaction, with the reaction process, additional hydrogen can be produced by a water gas shift reaction ($CO + H_2O \rightleftharpoons CO_2 + H_2$). Therefore, the H_2/CO ratio in the MSR product is typically higher than 3. Due to the high H_2/CO ratio, MSR was widely employed to produce hydrogen.

However, in Fischer−Tropsch synthesis (FTS), an important application of syngas, lower H_2/CO is more beneficial.[92, 93] Typically, in the product of DRM reaction, the H_2/CO ratio is lower than 1 due to the accompanied reverse water-gas shift reaction ($CO_2 + H_2 \rightleftharpoons CO + H_2O$). In addition, the main greenhouse gas, carbon dioxide, can be converted into syngas in the DRM reaction. Therefore, the DRM reaction has become more and more important and has received more attention. Different transition metals (e.g., Rh,[94, 95] Pt,[96, 97] Ir,[98] Pd,[99] Ru,[100, 101] and Ni[102, 103]) were employed as catalysts for the DRM reaction. Among them, noble metal catalysts showed better resistance to coking, as compared to Ni-based catalysts.[104, 105] However, due to the limited availability and high cost of noble metals, it is considered desirable to develop Ni-based catalysts. Many methods were employed to synthesize supported Ni nanoparticle catalysts. The Ni nanoparticles synthesized by conventional methods were typically large. Gould et al.[52] deposited highly dispersed Ni nanoparticles (~3 nm) on γ-Al_2O_3 nanoparticles by ALD and the catalyst showed high activity in catalyzing the DRM reaction.

The main disadvantage of using Ni catalysts for methane reforming reactions is deactivation, which is caused by both coking and sintering of Ni nanoparticles to form larger particles with lower catalytic activity.[106] Coking could be decreased by running the reaction at high temperatures and using small Ni particles because their step edges are small enough to limit carbon nucleation and growth.[107, 108] Therefore, the inhibition of the sintering of Ni nanoparticles is very important for improving the catalyst activity and stability. The small Ni nanoparticles synthesized by ALD should be beneficial for the

catalyst performance. In addition, porous materials should be better catalyst support as compared to nonporous materials since the porous structures could limit the Ni nanoparticles sintering.

Another possible solution to retard the sintering and coking is to improve the Ni-support interaction of the catalyst.[109, 110] Many methods were employed to enhance the Ni-support interaction to improve the catalyst performance in the DRM reaction. For example, Pan et al.[111] employed plasma treatment on the catalyst during preparation of Ni/SiO_2 catalyst, and the Ni-support interaction was strengthened. Smaller-sized Ni nanoparticles and higher Ni dispersion were achieved, and the catalyst performance in the DRM reaction also improved due to the plasma treatment. Different promoters were also employed to improve the Ni-support interaction. For example, Rezaei et al.[112] employed La_2O_3 to modify the Ni/ZrO_2 catalyst using the impregnation method. The Ni-support interaction and Ni dispersion were increased due to the La_2O_3 promoter. The promoted catalyst showed higher activity and stability in the DRM reaction than the Ni/ZrO_2 catalyst. Roh et al.[113] employed CaO to promote the Ni/Al_2O_3 catalyst using the impregnation method, and the promoted catalyst showed improved catalytic activity and stability in the DRM reaction. The better performance of the promoted catalyst is due to the strengthened Ni-support interaction, improved Ni dispersion, and higher coking resistance caused by the strong basicity due to the addition of CaO.

The DRM reaction is an endothermic reaction and is always carried out at elevated temperatures. Alumina was widely used to fabricate the catalyst support. However, alumina

has various phases, and most of them suffer phase change at elevated temperature. For example, gamma-alumina, a widely used catalyst support, suffers phase changes at temperatures ranging from 770 ℃ to 1030 ℃, which is always accompanied with a decrease of surface area.[114, 115] Therefore, alumina in those unstable phases are not suitable for fabricating the industrial catalyst support, especially for DRM reaction. Alpha-alumina, the most stable phase of alumina, was widely used as the catalyst support for industrial catalysts and would not suffer phase change at elevated temperatures.[116] Al-Megeren et al.[116] compared several industrial reforming catalysts and found that a catalyst with 10 holes showed the highest geometric surface area to volume ratio of 2.013×10^3 m^2/m^3. Ceramic hollow fibers attracted a lot of attention due to their high geometric surface area to volume ratio. Recently, a new type of α-Al_2O_3 ceramic hollow fiber with a four-channel configuration was developed.[117] The fibers showed higher mechanical strength as compared to conventional one-channel hollow fibers. In addition, the four-channel hollow fiber should have higher geometric surface area to volume ratio as compared to conventional one-channel hollow fiber with the same outer diameter considering the inner surfaces of the four channels. In this dissertation, both porous gamma-alumina particles and four-channel α-Al_2O_3 hollow fibers were studied as Ni nanoparticles support for DRM.

1.6. DISSERTATION SUMMARY

Section 1 includes five papers. In Paper I, the synthesis of a novel nanostructured size-selective catalyst with an ultra-thin porous shell and porous substrates was introduced.

The ultra-thin porous alumina shell was obtained from the thermal decomposition of an alucone film deposited by MLD. The size selectivity of the catalyst was realized by the size-discrimination effect of the porous alumina shell, which was verified by examining the liquid-phase hydrogenation of n-hexene versus cis-cyclooctene.

In Paper II, an improved size-selective catalyst based on the catalyst reported in Paper I with gaps between the metal nanoparticles and the shells was synthesized. The gaps greatly reduced the catalyst activity loss caused by the contact areas between the catalytic sites and the shells. The gaps were introduced by depositing a sacrificial layer of self-assembled monolayers (SAMs) before the deposition of porous shells on the catalyst surface. Evaluations of the activity and selectivity of the catalysts were made by catalytic hydrogenation of n-hexene versus cis-cyclooctene.

In Paper III, a highly active and selective porous silica-gel-particle-supported nickel nanoparticle catalyst was synthesized by ALD for chemoselective transfer hydrogenation of nitroarenes. The synthesized catalyst showed very high activity and selectivity in catalyzing hydrogenation of different nitroarenes to corresponding aromatic amines. The catalyst can be isolated by a magnet and rinsed thoroughly for reuse. The catalyst showed excellent reusability.

In Paper IV, a highly stable and active nickel nanoparticle catalyst supported on porous gamma-alumina particles was synthesized by ALD for DRM reaction. The catalyst can be activated during the DRM reaction, and the activated catalyst showed exceptionally high catalytic activity and excellent stability in DRM reaction for over 300 h at

temperatures that ranged from 700 °C to 850 °C. The excellent stability of the catalyst resulted from the formation of $NiAl_2O_4$ spinel, which could greatly increase the interaction between the Ni nanoparticles and the substrate. The high catalytic activity was due to the high dispersion of Ni nanoparticles deposited by ALD and the reduction of $NiAl_2O_4$ spinel to metallic Ni during the DRM reaction at 850 °C.

In Paper V, a nickel nanoparticle catalyst supported on a novel structured alpha-alumina hollow fiber with a four-channel configuration was prepared for DRM reactions. The catalyst showed exceptionally high catalytic activity in the DRM reaction. Different cycles (2, 5, and 10) of Al_2O_3 ALD films were applied on the hollow-fiber-supported Ni catalysts to improve the interaction of Ni nanoparticles and the support. Both the catalyst activity and stability were improved with the deposition of Al_2O_3 ALD films. Among the overcoated catalysts, the catalyst with 5 cycles of Al_2O_3 ALD showed the best performance.

In Section 2, the findings of this dissertation are summarized and future work directions are discussed.

PAPER

I. ENCAPSULATION OF SUPPORTED METAL NANOPARTICLES WITH AN ULTRA-THIN POROUS SHELL FOR SIZE-SELECTIVE REACTIONS

Zeyu Shang[1], Rajankumar L. Patel[1], Brian W. Evanko, and Xinhua Liang*

Department of Chemical and Biochemical Engineering, Missouri University of Science

and Technology, Rolla, Missouri 65409, USA.

*Tel: 1-573-341-7632; E-mail: liangxin@mst.edu

[1]Both authors contributed equally to this work.

ABSTRACT

A novel nanostructured catalyst with an ultra-thin porous shell obtained from the thermal decomposition of an aluminium alkoxide film deposited by molecular layer deposition for size-selective reactions was developed. The molecular sieving capability of the porous metal oxide films was verified by examining the liquid-phase hydrogenation of n-hexene versus cis-cyclooctene.

Heterogeneous catalysts are widely used (e.g., producing fertilizers, making gasoline from petroleum, and controlling automotive exhaust pollution via the catalytic muffler). However, heterogeneous catalysts cannot selectively convert specific molecules in the reactants mixture to catalyze only desired reactions.[1] Size-selective catalysts with a metal core and porous oxide shell have a promising structure that can increase the reaction selectivity through reactant molecular discrimination.[1-2]

Current research activities in this area are mainly focused on encapsulating unsupported catalysts or nanoparticles supported on dense catalyst supports.[2-3] Nishiyama et al.[2a] applied an aqueous solution of fumed silica, ethanol, and tetrapropylammonium hydroxide (TPAOH) to synthesize silicalite-1 coatings on spherical Pt/TiO$_2$ particles with a diameter of 0.5 mm under hydrothermal conditions. The thickness of the silicalite-1 layer was about 40 μm. Yang et al.[2b] developed a size-selective catalyst with a core-shell structure, where a Pd-containing silica core was surrounded by a silica shell in the presence of a cationic surfactant. This catalyst showed good activity and selectivity in the benzyl alcohol aerobic oxidation. Lu et al.[3] encapsulated unsupported surfactant-capped Pt nanoparticles by a zeolitic imidazolate framework (ZIF-8) with an average pore size of about 1.2 nm and a film thickness of about 200 nm. The ZIF-8 porous coating greatly increased the selectivity towards hydrogenation of n-hexene over cis-cyclooctene. However, compared to the naked catalyst, there was a 60% conversion loss for n-hexene hydrogenation mainly due to the mass diffusion barrier from the relatively thick ZIF-8 coating.

Normally, heterogeneous catalysts consist of small metal particles dispersed on a high surface area porous oxide support. The support maximizes the number of metal atoms at a surface, since metal atoms in the bulk are not involved in catalytic reactions. Traditional methods like hydrothermal synthesis[4] and sol-gel processes[5] can prepare inorganic coatings with few defects, such as zeolite membranes and mesoporous films. However, it is difficult for these methods to deposit ultra-thin porous films inside the porous structure of the catalyst supports and control the thickness of the films with nanometer precision.

It is highly desirable to develop a new strategy to prepare an ultra-thin porous film with controllable pore size and a limited mass diffusion barrier. Lu et al.[6] showed that ultra-thin porous alumina films could be formed from dense atomic layer deposited (ALD) alumina films by thermal treatment at 700 ℃. The pore size was about 2 nm. The formation of the porous structure was a result of the heat treatment process and there was no control over pore size. Canlas et al.[7] prepared shape-selective sieving layers on an oxide catalyst surface by grafting the catalyst particles with bulky single-molecule sacrificial templates with submonolayer coverage, then partially overcoating the catalyst with alumina through ALD. The number of the nanocavities was controlled by the number of template molecules grafted on the catalyst surface. The size of the nanocavities was controlled by the size of the template molecule and the thickness of ALD films. Although they achieved good conversion and selectivity for photooxidation of certain alcohols, their technique requires rigid molecules with certain surface orientations as sacrificial templates and many steps are needed to prepare the shape-selective sieving layers.

Recently, one novel method was developed by Liang et al. to prepare ultra-thin porous aluminium oxide films formed from the calcination of aluminium alkoxide (alucone) films, which were deposited by molecular layer deposition (MLD) using trimethylaluminium (TMA) and ethylene glycol (EG) as precursors.[8] The average pore size of porous alumina was about 0.6 nm (more than 95%).[8] MLD is a layer-by-layer gas phase thin film coating technique, which has been utilized to deposit pure polymer films or hybrid polymer films with nanometer-sized control of film thickness and well controlled film composition.[9] The self-limiting nature of MLD makes it ideal for coating porous substrates where line-of-sight gas phase deposition methods fail. Herein, we prepared Pt/SiO_2 catalysts encapsulated by an ultra-thin porous alumina film by MLD, as schematically shown in Fig. 1. Due to the conformal oxide coverage and sub-nanometer pores, the reaction rates of larger reactants should be slowed because they diffuse much more slowly than the smaller reactants through the oxide layer. Since the porous film is only several nanometers thick, the mass diffusion barrier for the smaller molecules is minimal. The combination of the catalytic properties of Pt nanoparticles and the molecular sieving capability of the porous oxide films was evaluated by examining the liquid-phase hydrogenation of n-hexene versus cis-cyclooctene.

The Pt nanoparticles were deposited on mesoporous silica particles by ALD using methylcyclopentadienyl-(trimethyl) platinum(IV) ($MeCpPt-Me_3$) and oxygen as precursors in a fluidized bed reactor, as described in detail elsewhere.[10] The silica particles are 30-75 μm in diameter with an average pore size of 15 nm and a Brunauer-Emmett-
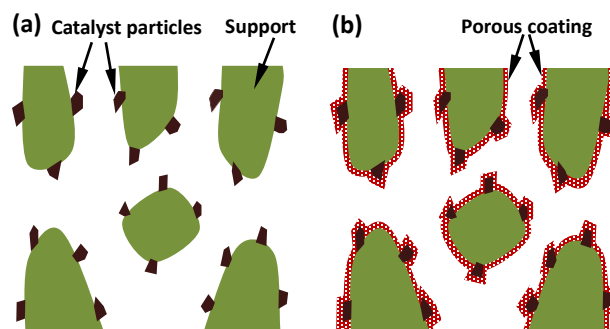
Fig. 1. Schematic representation of supported metal catalysts (a) before and (b) after a porous coating on all surfaces of the catalyst particles.

Teller (BET) surface area of 270 m^2/g. Three cycles of Pt ALD were carried out at 300 ℃ to obtain a Pt loading of 2.2 wt.%, as measured by inductively coupled plasma-atomic emission spectroscopy (ICP-AES). One cross-sectional scanning transmission electron microscopy (STEM) image of Pt/SiO$_2$ is displayed in Fig. 2a. The white points in the picture are Pt nanoparticles. The Pt nanoparticles are uniformly dispersed on the surface of silica gel particles and inside of the porous structures. The average Pt particle size is about 2 nm. The Pt/SiO$_2$ particles were coated with three thicknesses of alucone MLD films, deposited with 20, 30, and 40 cycles of alternating reactions of TMA and EG in a fluidized bed reactor at 160 ℃.[11] Three corresponding thicknesses (~2, 3, and 4 nm) of porous alumina films were then formed by oxidation at 400 ℃ in air, as described elsewhere.[8] During the oxidation process, the samples were heated in air from room temperature to 400 ℃ at a rate of 1 ℃/min, kept at 400 ℃ for one hour, and then cooled to room temperature at the same rate. The organic component was removed completely and highly porous

alumina films were formed. The carbon chain length of the polymer component determines

pore size, so MLD precursors with different carbon chain lengths could lead to porous

metal oxide films with different pore sizes. The mass fraction of Pt in the catalyst decreased

slightly as the number of MLD cycles increased, as shown in Fig. 2b, because the alumina

film increased the catalyst weight.
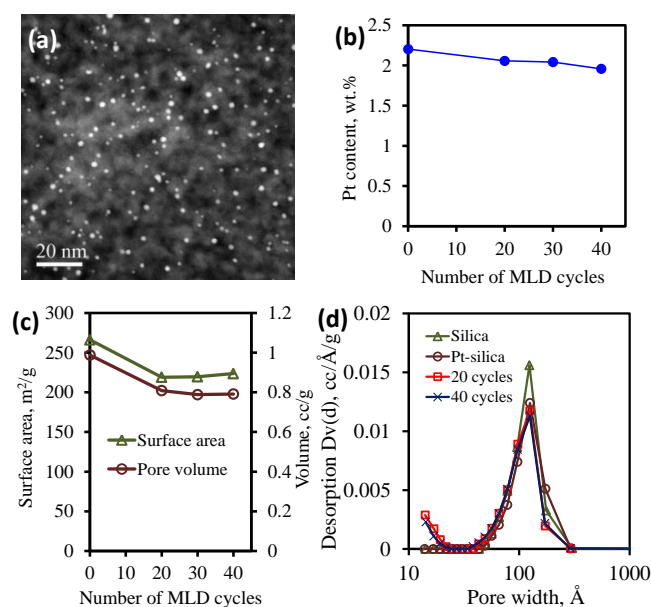
Fig. 2. (a) Cross-sectional STEM image of the Pt nanoparticles on silica gel particles, (b) Pt content, (c) surface area and pore volume, and (d) pore size distribution of the Pt/SiO$_2$ particles coated with different thicknesses of porous alumina films.

A Quantachrome Autosorb-1 was used to obtain nitrogen adsorption and desorption

isotherms of catalyst particles at -196 ºC. The specific surface areas of the samples were

calculated using the BET method in the relative pressure range of 0.05–0.25. The total pore volumes were calculated from the adsorption quantity at a relative pressure of $P/P_0 = 0.99$. The pore size distribution curves were derived from the adsorption branches of the isotherms using the Barrett–Joyner–Halenda (BJH) method. As shown in Fig. 2c, the surface area of the Pt/SiO_2 particles decreased from 266 to 219 m^2/g with 20 cycles of MLD coating, and slightly increased with the further deposition of MLD films. This increase is due to the contribution of the higher surface area porous alumina films, which can have a surface area as high as 1000 m^2/g.[8] The pore volume of the Pt/SiO_2 particles decreased from 0.99 to 0.81 cm^3/g with 20 cycles of MLD coating, and slightly decreased again to 0.79 cm^3/g with the further deposition of MLD films. As shown in Fig. 2d, the average pore size of the silica gel particles was about 15 nm. The number of mesopores decreased with the deposition of Pt nanoparticles, but there was no further decrease with the deposition of porous alumina films. Clearly, a large number of micropores were formed after MLD coating, compared to silica gel or Pt/SiO_2 particles. The average pore size of the porous film was estimated to be 0.6 nm.[8]

The catalytic hydrogenation of olefins (n-hexene >99%, and cis-cyclooctene >95%) was carried out in an ethyl acetate solution under a static hydrogen atmosphere at 35 ºC. The reactions were conducted in unstirred mini-batch reactors assembled from 3/8 inch stainless steel Swagelok® parts. Port connectors sealed with a cap on one end and one three-way valve on the other end gave a reactor volume of about 2 mL. In a typical run, n-hexene or cis-cyclooctene (0.08 g), ethyl acetate (0.78 g) and the Pt catalysts (~0.006 g) were added

to the reactor. All catalysts had an identical Pt loading even though the total mass within the reactor increases as the number of MLD cycles increases. The mass ratio of Pt to olefin was 0.15%. The residual air in the reactor was expelled by flushing with hydrogen. The reactor was first pressurized with hydrogen to 20 psi and depressurized to atmosphere pressure. This process was repeated 50 times. After this flushing process, more than 99.999% of air was replaced by hydrogen gas. The control experiments indicated that the mass loss of the reactants and the solvent during this flushing process was less than 0.5 wt.%. The reaction was carried out at 1 atm of hydrogen and 35 ℃ for 24 hours. The amount of hydrogen in the closed system was more than enough for the hydrogenation reaction. After the reaction, the catalyst powder was filtered off and the filtrate was analysed using a gas chromatograph (Agilent, 6890N) equipped with a 30 m DB-5 column and FID detector to determine the conversion and selectivity.

The control experiments indicated that there was no catalytic activity of olefin hydrogenation for both silica gel particles and alumina ALD films. The catalytic activity resulted solely from Pt. The results are listed in Fig. 3. For the uncoated Pt/SiO$_2$ catalyst, the conversion of n-hexene and cis-cyclooctene was 9.1% and 6.9%, respectively. The conversion of n-hexene decreased with ~2 nm of porous alumina film (20 cycles of MLD), and decreased slightly more with further increases in film thickness. The conversion of n-hexene fell to 4.5% after the catalyst was coated with ~4 nm of alumina film. In contrast, the conversion of cis-cyclooctene decreased almost linearly as the thickness of the porous alumina films increased, and no obvious cis-cyclooctene conversion (<0.02 %) was

observed with ~4 nm of alumina films. Clearly, the naked Pt nanoparticles displayed indiscriminate catalysis of olefin hydrogenation. In contrast, the Pt nanoparticles encapsulated with a porous alumina shell showed selectivity for catalytic hydrogenation of n-hexene versus cis-cyclooctene due to the size discrimination of the ultra-thin porous layer.
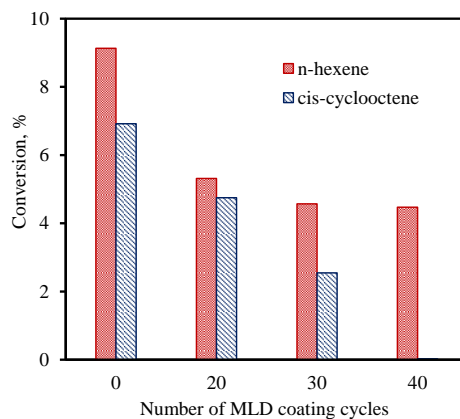
Fig. 3. Size-selective hydrogenation of n-hexene and cis-cyclooctene catalyzed by Pt/SiO₂ particles coated with different thicknesses of porous alumina films.

Previous studies of H_2 chemisorption indicated that the Pt dispersion decreased when the Pt nanoparticles were encapsulated with porous alumina films due to the contact points between Pt particles and the porous metal oxide films.[12] About 42% of the Pt surface area was lost with the deposition of 40 cycles of MLD films.[12] In this study, the reduction of the conversion of n-hexene was 51% with the deposition of 40 cycles of MLD films on

Pt/SiO$_2$, compared to the naked Pt/SiO$_2$. It is believed that the decline in the conversion of n-hexene was mainly caused by the loss of Pt metal surface, rather than the mass diffusion limitation resulting from the thin porous oxide films. The porous structure allows smaller reactants to access the encapsulated active sites, and inhibits or prevents the reactants with larger molecular size from accessing the Pt sites. Since the film is ultra-thin, the reactants and products of small molecules can pass freely through the porous films. The molecular size of H$_2$ is so small, that the size effects for H$_2$ molecules can be neglected. The size-selectivity effect results mainly from the difference in the molecular size of olefins.

In summary, a novel strategy to prepare a supported size-selective metal nanoparticle catalyst with an ultra-thin porous shell was developed. The thickness of the porous oxide films could be well controlled at subnanometer scale by applying the MLD technique. The pore size of the film was about 0.6 nm. The size selective effect of the porous alumina films was verified by the liquid-phase hydrogenation of n-hexene versus cis-cyclooctene. This catalyst showed great selectivity in the hydrogenation of olefins. Importantly, the mass diffusion limitation was not significant due to the ultra-thin films. The success of making these materials by MLD opens up a new method for preparing size-selective catalysts.

ACKNOWLEDGMENTS

NOTES AND REFERENCES

1. P. Collier, S. Golunski, C. Malde, J. Breen and R. Burch, *J. Am. Chem. Soc.*, 2003, **125**, 12414.

2. (a) N. Nishiyama, K. Ichioka, D. H. Park, Y. Egashira, K. Ueyama, L. Gora, W. D. Zhu, F. Kapteijn and J. A. Moulijn, *Ind. Eng. Chem. Res.*, 2004, **43**, 1211; (b) H. Q. Yang, Y. Z. Chong, X. K. Li, H. Ge, W. B. Fan and J. G. Wang, *J. Mater. Chem.*, 2012, **22**, 9069.

3. G. Lu, S. Z. Li, Z. Guo, O. K. Farha, B. G. Hauser, X. Y. Qi, Y. Wang, X. Wang, S. Y. Han, X. G. Liu, J. S. DuChene, H. Zhang, Q. C. Zhang, X. D. Chen, J. Ma, S. C. J. Loo, W. D. Wei, Y. H. Yang, J. T. Hupp and F. W. Huo, *Nat. Chem.*, 2012, **4**, 310.

4. Z. P. Lai, G. Bonilla, I. Diaz, J. G. Nery, K. Sujaoti, M. A. Amat, E. Kokkoli, O. Terasaki, R. W. Thompson and M. Tsapatsis, *Science*, 2003, **300**, 456.

5. D. Zhao, P. Yang, N. Melosh, J. Feng, B. F. Chmelka and G. D. Stucky, *Adv. Mater.*, 1998, **10**, 1380.

6. J. L. Lu, B. S. Fu, M. C. Kung, G. M. Xiao, J. W. Elam, H. H. Kung and P. C. Stair, *Science*, 2012, **335**, 1205.

7. C. P. Canlas, J. L. Lu, N. A. Ray, N. A. Grosso-Giordano, S. Lee, J. W. Elam, R. E. Winans, R. P. Van Duyne, P. C. Stair and J. M. Notestein, *Nat. Chem.*, 2012, **4**, 1030.

8. X. H. Liang, M. Yu, J. H. Li, Y. B. Jiang and A. W. Weimer, *Chem. Commun.*, 2009, **46**, 7140.

9. (a) T. Yoshimura, S. Tatsuura and W. Sotoyama, *Appl. Phys. Lett.*, 1991, **59**, 482 (b) A. A. Dameron, D. Seghete, B. B. Burton, S. D. Davidson, A. S. Cavanagh, J. A. Bertrand and S. M. George, *Chem. Mater.*, 2008, **20**, 3315.

10. X. H. Liang, Y. Zhou, J. H. Li and A. W. Weimer, *J. Nanopart. Res.*, 2011, **13**, 3781.

11. X. H. Liang, D. M. King, P. Li, S. M. George and A. W. Weimer, *AIChE J.*, 2009, **55**, 1030.

12. X. H. Liang, J. H. Li, M. Yu, C. N. McMurray, J. L. Falconer and A. W. Weimer, *ACS Catal.*, 2011, **1**, 1162.

II. "CORE−SHELL" NANOSTRUCTURED SUPPORTED SIZE-SELECTIVE CATALYSTS WITH HIGH CATALYTIC ACTIVITY

Zeyu Shang, and Xinhua Liang*

Department of Chemical and Biochemical Engineering, Missouri University of Science

and Technology, Rolla, Missouri 65409, United States

*E-mail: liangxin@mst.edu

ABSTRACT

We report the synthesis of a highly active, supported nanostructured metal nanoparticle catalyst with an ultra-thin porous shell and gaps between the metal nanoparticles and the shell for size-selective reactions. The size-selectivity of the catalysts could be realized through the porous shell. The gaps were able to reduce catalytic activity loss due to the contact areas between the shell and the catalytic sites. Evaluations of the activity and selectivity of the catalysts were made by catalytic hydrogenation of n-hexene versus cis-cyclooctene. Further verification of the high catalytic activity of the nanostructured catalysts was by oxidation of carbon monoxide.

Keywords: atomic/molecular layer deposition, hydrogenation, porous films, size selective, supported catalysts

Heterogeneous catalysts are widely used because of their many advantages, including the ease of separating the catalysts by filtration after a reaction, and their reusability.[1-3] However, compared to other catalysts (e.g., enzyme and organometallic catalysts), it is generally difficult for a heterogeneous catalyst to selectively convert certain molecules in a reactant mixture to desired products.[4, 5] A size-selective catalyst, that has a metal core and a porous oxide shell, is one kind of catalyst that can increase reaction selectivity through reactant molecular discrimination.[5-16] Its porous structure allows smaller reactants to access the encapsulated active sites, and to inhibit or prevent larger molecular reactants from accessing the active sites. Zeolites,[8-13] metal organic frameworks (MOFs),[15] mesoporous titania,[17] and mesoporous silica,[18-22] that have well-defined porous structures, have been used to encapsulate metal nanoparticle catalysts to form a porous core-shell structure (called "core-shell" elsewhere in this paper). Zeolites have an inherent microporous system of molecular dimensions, that allow size-selective catalysis, but their shells are relatively thick (normally ≥200 nm). For example, Nishiyama et al.[8] applied ethanol, tetrapropylammonium hydroxide (TPAOH), and a fumed silica aqueous solution to synthesize 40 μm thick silicalite-1 coatings on spherical Pt/TiO_2 particles that were 0.5 mm in diameter. Lu et al.[15] encapsulated unsupported surfactant-capped Pt nanoparticles in a zeolitic imidazolate framework (ZIF-8), that had an average pore size of 1.2 nm and a thickness of about 200 nm, and demonstrated that the porous coating greatly increased the selectivity of hydrogenation of n-hexene over that of cis-cyclooctene. However, the conversion of n-hexene decreased significantly, from 16.6% (the naked catalyst) to 7.3%

(the size-selective catalyst). A decrease in catalytic activity has been commonly observed in "core-shell" structured size-selective catalysts.[5, 10, 12] We believe that this was because of the combined effect of the thickness of the porous shell and blockage of active sites due to the contact areas between the porous shell and the catalytic sites. The above-mentioned examples were based on the liquid phase methods used to prepare relatively thick porous shells. Mesoporous silica shells can be prepared as thin as 10 nm,[18] but their layers are not normally selective, since pore sizes are too large. Current research activities that have been studying size-selective catalysts have mainly focused on encapsulating unsupported catalysts or nanoparticles supported on dense catalyst supports. However, the metal nanoparticles that are used in industry are normally dispersed on high surface area supports so that the resulting metal nanoparticles have a large fraction of their atoms on the surface. It is difficult to use liquid methods to apply such porous shells to catalyst particles that have highly porous supports. In addition, the catalytic activity of the catalysts would be significantly reduced because of the mass transport limitations posed by the thick porous shell and the contact areas between the active sites and the porous shell.

Recently, we synthesized a size-selective catalyst with an ultra-thin porous alumina shell coated on Pt/SiO_2.[23] Ultra-thin porous alumina films were formed from the oxidation of hybrid organic/inorganic aluminum alkoxide (alucone) films deposited by molecular layer deposition (MLD), which is a layer-by-layer gas phase thin film coating technique. Advantages of such a "core-shell" nanostructured catalyst are that the porous films can be deposited conformally on highly porous 3D structures and the thickness of the porous films

can be precisely controlled at an angstrom level by varying the number of MLD coating cycles. Since the pore size of the porous films is mainly determined by the carbon chain length of the organic components in the MLD precursor, the pore size could be finely tuned by choosing precursors with carbon chains of suitable lengths. In our previous study,[23] various thicknesses of porous alumina films were deposited on Pt and its high surface area silica support. Compared to a naked catalyst, this new nanostructured catalyst, with a porous shell formed from 40 cycles of alucone MLD, showed significant improvement in selectivity toward hydrogenation of n-hexene, as compared to cis-cyclooctene, due to the size discrimination of the porous shell. However, there was still about a 51% loss for the n-hexene conversion, although this was lower than the results reported by other groups.[15] Since the porous alumina shell is ultra-thin, the mass transport limitation should not have much influence. It is hypothesized that the reduction in activity was mainly caused by a decrease in the active sites due to the contact areas between the porous shell and the catalytic metal nanoparticles. This could also be a common reason for the catalytic activity loss of the core-shell catalysts that had been prepared by conventional liquid phase methods.

To reduce the contact areas, we propose a new approach to overcome this dilemma. The idea is to introduce a sacrificial layer of self-assembled monolayers (SAMs) using thiols, which could be selectively deposited on the surface of the metal nanoparticles (e.g., Pd, Au and Pt).[24-27] For example, Cargnello et al.[28] employed thiols to form a protective layer on Pd nanoparticles to synthesize a Pd@CeO$_2$ core-shell structured catalyst. For this

report, we selectively deposited thiol SAMs on metal nanoparticles before depositing MLD layers on both the catalytic metal particles and the catalyst support. The SAMs and the organic components of the MLD film can be removed by oxidation in air. After the oxidation process, microporous structures in MLD films and gaps between the porous shell and the metal nanoparticles would form, as schematically shown in Figure 1. In this way, the contact areas between the shell and the metal nanoparticles could be greatly reduced. For this study, Pt nanoparticles were chosen as the catalysts, since they are very active in a wide range of catalytic reactions. Hexanethiol was used to form SAMs on the surface of the Pt nanoparticles. This nanostructured catalyst was employed to catalyze the carbon monoxide (CO) oxidation reaction and hydrogenation reactions of n-hexene and cis-cyclooctene. CO-chemisorption was also employed to verify the high Pt dispersion of the size-selective catalysts with gaps.

Platinum nanoparticles were deposited on porous γ-alumina particles by atomic layer deposition (ALD) in a fluidized bed reactor,[29, 30] as described in detail elsewhere.[31] The Pt loading was 2.4 wt.%, determined by inductively coupled plasma-atomic emission spectroscopy (ICP-AES). The dispersion of Pt particles and the particle size distribution were observed by cross-sectional scanning transmission electron microscopy (STEM), as shown in Figure 2a. The small white spots in that figure are Pt nanoparticles with an average particle size of 1.6 nm. Pt nanoparticles were uniformly deposited on both surfaces and inside the porous structures of the γ-alumina particles.
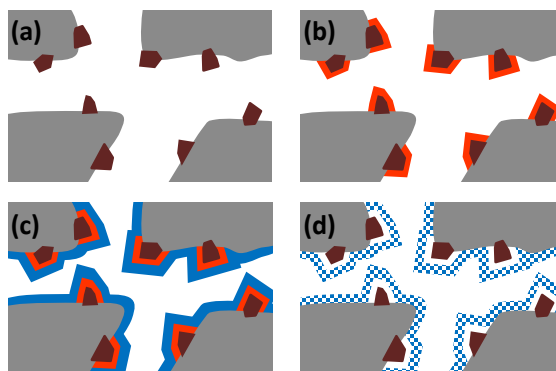
Figure 1. Schematic representation of supported metal catalysts: (a) Pt deposited on porous γ-alumina particles, (b) SAMs selectively deposited on the surface of Pt nanoparticles, (c) alucone MLD film coated on the surfaces of Pt particles and catalyst support, and (d) porous films and gaps formed after removal of organic components.

SAMs were deposited on the surfaces of Pt nanoparticles by immersing the Pt/γ-alumina particles in a 10 mM ethanol solution of hexanethiol for 24 hours. Alucone MLD films were coated on SAMs-treated Pt/γ-alumina particles, as described previously.[32] Different cycles (30, 40, and 50) of alucone MLD layers were applied. The SAMs and the organic components in the films were removed by oxidation in air at 400 °C. Catalysts were formed that had three corresponding thicknesses of ultra-thin porous shells and gaps between the Pt nanoparticles and the porous shells. Details of catalyst preparation processes are presented in Supporting Information.

The surface areas and pore volumes decreased slightly with the deposition of Pt nanoparticles and decreased further with SAMs coated on the surfaces of the Pt nanoparticles (Figure 2b). This decrease was due to the blockage by the SAMs of some micropores (Figure 2c) and the mesopore size reductions in the catalyst support (Figure S1

in the Supporting Information). The pore volumes and surface areas decreased further after 30 cycles of MLD coating deposited on the SAMs-treated sample. This trend continued with an increase in the number of MLD cycles (Figure S2 in the Supporting Information). After oxidation, as shown in Figure 2b, the sample with 30 cycles of MLD films had a larger surface area and pore volume than the SAMs-treated sample did. This increase was due to the fact that both the SAMs and the organic components in the MLD films were removed during the oxidation process. The pore size of the porous shell was about 0.6 nm, as we reported earlier.[33] Similar results were observed for the samples coated with a larger number of MLD coating cycles.
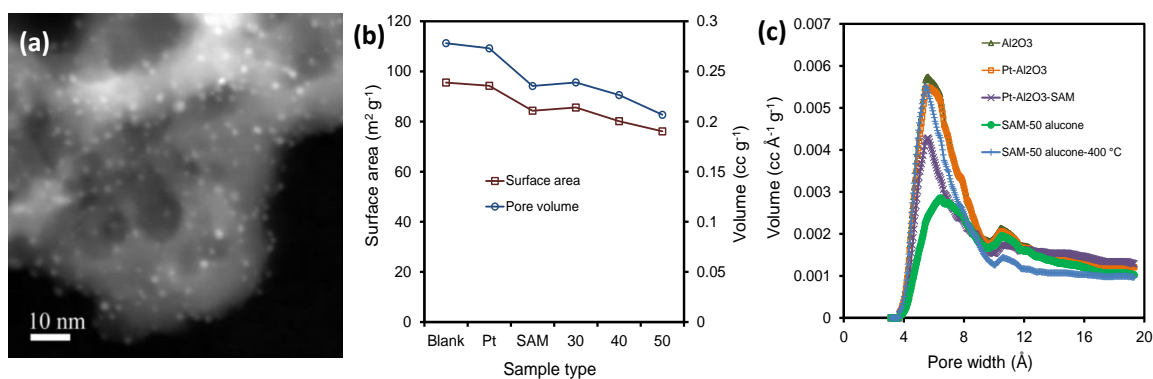
Figure 2. (a) STEM image of Pt/γ-alumina, (b) surface area and pore volume (after oxidation for all MLD coated samples), and (c) micropore size distribution of the γ-alumina particles, Pt/γ-alumina particles, and SAMs-treated Pt/γ-alumina particles with and without porous films and gaps between Pt nanoparticles and porous shells.

The experimental details of hydrogenation reactions are shown in the Supporting Information. Control experiments indicated that both γ-alumina particles and porous alumina shells from alucone MLD films showed no catalytic activity for olefin hydrogenation. The results for catalytic hydrogenation reactions are shown in Figure 3. For the naked sample, the reaction rates of n-hexene and cis-cyclooctene were 28.5 mmol·h^{-1}g$_{Pt}^{-1}$ and 10.9 mmol·h^{-1}g$_{Pt}^{-1}$, respectively. The difference in the reaction rates was due to the chemical properties of these two different olefins. The reaction rates of both n-hexene and cis-cyclooctene decreased (26.7 mmol·h^{-1}g$_{Pt}^{-1}$ and 7.3 mmol·h^{-1}g$_{Pt}^{-1}$, respectively) after the deposition of 30 cycles of alucone MLD and decreased further with the increase in the number of MLD cycles. The decrease in the cis-cyclooctene reaction rate was due to the size-selective effect of the porous shell, since the molecular size of cis-cyclooctene was close to, or larger than, the pore size of the porous films. The sample with 30 cycles of alucone MLD still showed activity in catalyzing the hydrogenation of cis-cyclooctene, indicating that the porous films formed from 30 cycles of alucone MLD were not thick enough or did not completely cover the Pt nanoparticles. The growth rate of MLD films on SAMs treated Pt/alumina would be slower than that of MLD on metal oxide surfaces. This should be due to the lack of functional groups on the Pt nanoparticles, which are necessary to initiate the alucone MLD coating process. Therefore, the first few cycles of coating deposited preferentially onto the most energetic (e.g., edge) sites, rather than uniformly blanketing the Pt particles entirely. With the deposition of SAMs on Pt/alumina, the surface functional groups of the sample may be reduced and a longer nucleation period would be

needed. Another possibility is that there were some defects in the thin porous films due to the high temperature oxidation process to remove the SAMs and the organic components in the MLD films. With the increase in the number of MLD coating cycles, the porous films will be thicker with stronger mechanical properties. For the sample coated with 40 cycles of alucone MLD, the reaction rates of n-hexene and cis-cyclooctene decreased to 23.3 mmol·h^{-1}g$_{Pt}$$^{-1}$ and 1.9 mmol·h^{-1}g$_{Pt}$$^{-1}$, respectively. When the catalyst was coated with 50 cycles of alucone MLD, the reaction rate of n-hexene decreased to 23.2 mmol·h^{-1}g$_{Pt}$$^{-1}$ (a loss of about 19%), while the reaction rate of cis-cyclooctene decreased to 0.6 mmol·h^{-1}g$_{Pt}$$^{-1}$ (a loss of about 95%), as compared to the naked catalyst.
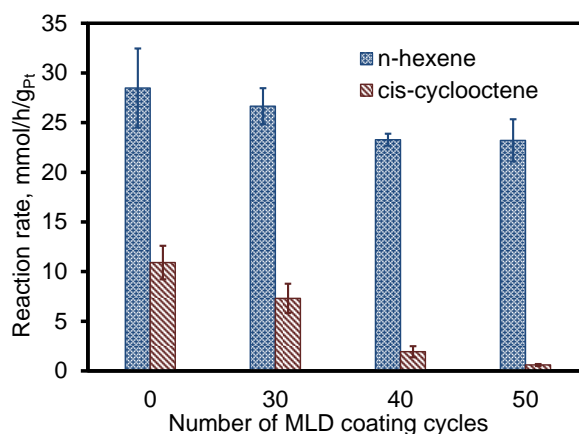
Figure 3. Hydrogenation results of n-hexene and cis-cyclooctene catalyzed by naked Pt/γ-alumina particles and coated with different thicknesses of porous films (with gaps).

Clearly, the naked Pt catalysts showed indiscriminate catalysis of olefin hydrogenation. However, the Pt catalysts, coated with a porous alumina shell, displayed selectivity for catalytic hydrogenation of n-hexene over that of cis-cyclooctene due to the size discrimination of the ultra-thin porous shell. In the work of Lu et al.,[15] the n-hexene conversion loss was about 56% (decreased from 16.6% to 7.3%) with the same reaction conditions used in this study. In our previous work,[23] the n-hexene conversion loss was 51% after 40 cycles of alucone MLD was deposited on the catalysts without gaps between the Pt nanoparticles and the shell. In this current work, the new nanostructured catalysts showed much higher catalytic activity while maintaining a strong size-selective effect. To further verify this, another series of samples were prepared with a porous alumina shell, but without the introduction of gaps. These samples were prepared by directly coating various thicknesses of alucone MLD films on Pt/γ-alumina particles. A catalyst with porous films (formed from 50 cycles of alucone MLD) was employed to catalyze the hydrogenation reactions for both n-hexene and cis-cyclooctene. The catalyst with 50 cycles of alucone MLD coating showed reaction rates of 14.3 mmol·h^{-1}g$_{Pt}^{-1}$ and 0.5 mmol·h^{-1}g$_{Pt}^{-1}$ for n-hexene and cis-cyclooctene, respectively. This catalyst showed good selectivity, as compare to that of the naked catalyst. However, the decrease in the n-hexene reaction rate was about 50%, which was consistent with our previously reported results.[23] This indicated a significant catalytic activity loss, as compared to that of the catalysts with gaps. For the catalysts with gaps, when the cycles of the alucone MLD increased from 40 to 50, there was almost no change in the reaction rate of n-hexene. This indicated that there was a

negligible mass diffusion limitation caused by the porous shell. The activity losses of the coated samples were caused by the contact areas between the Pt nanoparticles and the porous shells. The reaction rate loss of n-hexene was about 19%, so there was still about a 19% loss of the Pt metal surface. This could indicate that the porous shell was not free standing.

The porous alumina supported catalysts, with and without gaps, were all employed for the oxidation reactions of carbon monoxide. The experimental details of CO oxidation reactions are shown in the Supporting Information. The results of CO oxidation reactions catalyzed by the naked catalyst and coated catalysts with gaps are shown in Figure 4. For the uncoated catalyst, the CO conversion reached 100% at 215 °C, and for all of the coated catalysts with gaps, the CO conversion reached 100% at 223 °C (8 °C higher than the uncoated catalyst). The molecule sizes of carbon monoxide and oxygen were so small that the porous shell would not limit significant mass transport. In contrast, the coated catalysts without gaps showed a significant reduction in activity. As shown in Figure S4 in the Supporting Information, the CO conversion reached 100% at 234 °C for the samples with 30 and 40 cycles of MLD coating (without gaps). This was 19 °C higher than that of the naked sample, while the conversion of the sample with 30 cycles of coating was higher than that of the sample with 40 cycles of coating when the reaction temperature was lower than 200 °C. This indicated that the sample with 30 cycles of MLD coating had fewer contact areas. The CO conversion reached 100% at 247 °C for the sample with 50 cycles of MLD coating (without gaps), which was 32 °C higher than that of the naked sample,

and 13 °C higher than that of the samples with 30 and 40 cycles of MLD coating. This was due to the fact that the sample with 50 cycles of coating had more contact areas than the samples with 30 and 40 cycles. These results are consistent with those of a previous work.[34] Liang et al.[34] encapsulated Pt/silica with a similar porous alumina shell by MLD, and used these samples for a CO oxidation reaction; after 20 MLD cycles, the temperature for a 100 % CO conversion had increased 50 °C, as compared to that of the naked catalyst.

In order to observe the porous films and the gaps between the Pt nanoparticles and the porous shell, Pt nanoparticles were deposited on dense alumina nanoparticles by ALD. Larger Pt nanoparticles were synthesized by applying four cycles of Pt ALD on the substrate for the ease of observing Pt nanoparticles and porous films by TEM. As shown in Figure S5a in Supporting Information, the Pt nanoparticles (average particle size of ~3 nm) dispersed uniformly on the substrate surface. SAMs were deposited on the Pt nanoparticles supported on the dense alumina nanoparticles, following the same steps mentioned above. Then, 50 cycles of alucone MLD films were employed on the SAMs treated Pt/dense-alumina nanoparticles. After the removal of SAMs and organic components in the alucone MLD films by oxidation, gaps (~0.4 nm) between the Pt nanoparticles and porous alumina films could be observed (Figure S5b-d in the Supporting Information). In contrast, for the sample with a porous alumina shell but without gaps, as expected, no gaps between the Pt nanoparticles and the porous alumina films were observed by TEM (Figure S5e in the Supporting Information).
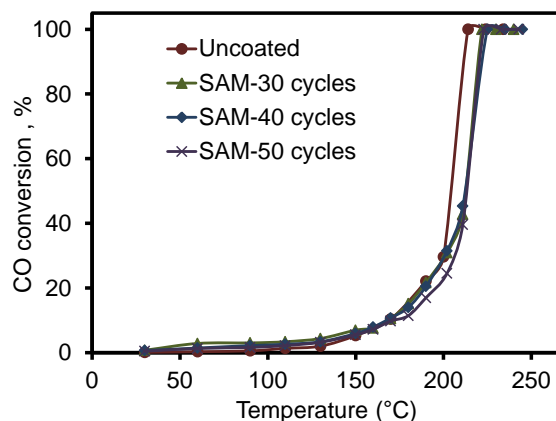
Figure 4. CO conversion of CO oxidation catalyzed by naked Pt/γ-alumina particles and coated with different thicknesses of porous films (with gaps).

To further verify that the catalysts with gaps had fewer contact areas than the catalysts without gaps, a CO-chemisorption test was employed on the naked catalyst, and on the 50 cycles of alucone MLD coated catalysts with and without gaps. The naked catalyst showed a Pt dispersion of 61.5%. The Pt dispersions were 48% and 30.6% for the coated catalysts with and without gaps, respectively. These Pt dispersion results were consistent with the results of n-hexene hydrogenation. The coated catalyst with gaps showed a higher Pt dispersion, as compared to the catalyst without gaps, indicating that the introduction of gaps could reduce the contact areas between the Pt nanoparticles and porous alumina films.

This series of tests indicated that the contact areas between the Pt particles and the porous films caused a lower catalytic activity of the catalyst, when the porous films were directly coated on the metal nanoparticle surfaces. Also, the porous alumina films should

be deposited on nanoparticles, on both the support surface and inside the porous structure of the support. Otherwise, the Pt activity of the catalyst would not decrease that much. The introduction of gaps greatly reduced the contact areas between the porous shell and the Pt nanoparticles and, thus, maintained the high catalytic activity of the catalysts for olefin hydrogenation and CO oxidation.

The SAMs were attached to catalytic centers by sulfur-platinum bonds, which may have decreased the catalytic activity of the catalyst.[35] We employed X-ray photoelectron spectroscopy (XPS) to detect different elements on the catalyst surface. Figure S6 in the Supporting Information shows the XPS spectra for thiol-treated porous γ-alumina support, and thiol-treated Pt/γ-alumina before and after oxidation. In all three samples, sulfur could be detected, but the sulfur peaks were very weak. High resolution XPS on sulfur was also employed to investigate and determine sulfur bonding status (Figure 5). A sulfur peak was observed at 169 eV on the thiol-treated γ-alumina sample (this was a sulfur-oxygen bond),[36] which could have been due to the fact that the physisorbed thiol had not been completely removed in the rinsing process. For the thiol-treated Pt/γ-alumina sample, before oxidation, one peak of sulfur was observed at 162.5 eV, representing a sulfur-metal bond.[36, 37] This peak was from the SAMs formed on the Pt surface. After oxidation, all of the sulfur attached to the Pt particles was removed, as shown in Figure 5. A sulfur peak was observed at 169 eV for the thiol-treated Pt/γ-alumina sample, after oxidation. This was due to the fact that the oxidized sulfur was trapped in the porous structure of the porous γ-alumina catalyst support or the porous shells, or both. Also, the carbon peak was weaker

(Figure S7 in the Supporting Information), indicating the removal of the organic components during oxidation. Clearly, after the oxidation process, the sulfur was removed from the Pt nanoparticles surfaces, which did not affect the catalytic activity of the catalyst.
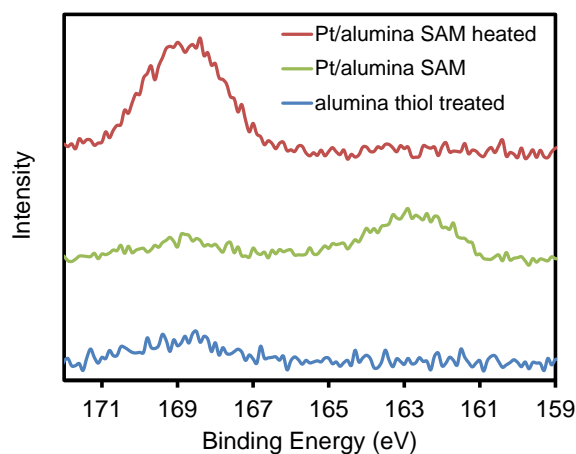
Figure 5. High resolution XPS spectra of sulfur (2p) of thiol treated porous γ-alumina support and thiol treated Pt/γ-alumina before and after oxidation.

In summary, a novel supported nanostructured metal catalyst was developed with an ultra-thin porous shell and gaps between the metal particles and the shell. The film thickness could be precisely controlled by varying the number of MLD coating cycles. The gaps were formed by introducing one sacrificial layer of SAMs, which were selectively deposited on the surfaces of the metal nanoparticles before the alucone MLD films were deposited on catalyst particles. The SAMs and the organic components of the MLD films could be removed by oxidation in the air. The selectivity and activity of the catalysts were

tested by hydrogenation reactions of n-hexene and cis-cyclooctene. This new nanostructured catalyst showed higher catalytic activity than the catalysts without the introduction of gaps did. The success of this gap forming strategy provides a new method for retaining the activity of size-selective catalysts, especially those consisting of a metal core and oxide shell structures.

ACKNOWLEDGMENTS

REFERENCES

1.   Corma, A.; Das, D.; Garcia, H.; Leyva, A. *J. Catal.* **2005**, *229*, 322-331.

2.   Mori, K.; Hara, T.; Mizugaki, T.; Ebitani, K.; Kaneda, K. *J. Am. Chem. Soc.* **2004**, *126*, 10657-10666.

3.   Choi, E.; Lee, C.; Na, Y.; Chang, S. *Org. Lett.* **2002**, *4*, 2369-2371.

4.   de Jong, K. P., *Synthesis of Solid Catalysts*; Wiley-VCH: Weinheim, Germany, 2009.

5.   Collier, P.; Golunski, S.; Malde, C.; Breen, J.; Burch, R. *J. Am. Chem. Soc.* **2003**, *125*, 12414-12415.

6.   vanderPuil, N.; Creyghton, E. J.; Rodenburg, E. C.; Sie, T. S.; vanBekkum, H.; Jansen, J. C. *J. Chem. Soc., Faraday Trans.* **1996**, *92*, 4609-4615.

7.   Khan, E. A.; Rajendran, A.; Lai, Z. P. *Ind. Eng. Chem. Res.* **2010**, *49*, 12423-12428.

8.   Nishiyama, N.; Ichioka, K.; Park, D. H.; Egashira, Y.; Ueyama, K.; Gora, L.; Zhu, W. D.; Kapteijn, F.; Moulijn, J. A. *Ind. Eng. Chem. Res.* **2004**, *43*, 1211-1215.

9.   Hojholt, K. T.; Laursen, A. B.; Kegnaes, S.; Christensen, C. H. *Top. Catal.* **2011**, *54*, 1026-1033.

10.   Laursen, A. B.; Hojholt, K. T.; Lundegaard, L. F.; Simonsen, S. B.; Helveg, S.; Schueth, F.; Paul, M.; Grunwaldt, J. D.; Kegnaes, S.; Christensen, C. H.; Egebald, K. *Angew. Chem., Int. Ed.* **2010**, *49*, 3504-3507.

11.   Mielby, J.; Abildstrom, J. O.; Wang, F.; Kasama, T.; Weidenthaler, C.; Kegnaes, S. *Angew. Chem., Int. Ed.* **2014**, *53*, 12513-12516.

12.   Li, S. W.; Tuel, A.; Laprune, D.; Meunier, F.; Farrusseng, D. *Chem. Mater.* **2015**, *27*, 276-282.

13.   Li, S. W.; Boucheron, T.; Tuel, A.; Farrusseng, D.; Meunier, F. *Chem. Commun.* **2014**, *50*, 1824-1826.

14.   Qiao, Z. A.; Zhang, P. F.; Chai, S. H.; Chi, M. F.; Veith, G. M.; Gallego, N. C.; Kidder, M.; Dai, S. *J. Am. Chem. Soc.* **2014**, *136*, 11260-11263.

15.   Lu, G.; Li, S. Z.; Guo, Z.; Farha, O. K.; Hauser, B. G.; Qi, X. Y.; Wang, Y.; Wang, X.; Han, S. Y.; Liu, X. G.; DuChene, J. S.; Zhang, H.; Zhang, Q. C.; Chen, X. D.; Ma, J.; Loo, S. C. J.; Wei, W. D.; Yang, Y. H.; Hupp, J. T.; Huo, F. W. *Nat. Chem.* **2012**, *4*, 310-316.

16.   Yang, H. Q.; Chong, Y. Z.; Li, X. K.; Ge, H.; Fan, W. B.; Wang, J. G. *J. Mater. Chem.* **2012**, *22*, 9069-9076.

17.   Zhang, Z. W.; Zhou, Y. M.; Zhang, Y. W.; Xiang, S. M.; Zhou, S. J.; Sheng, X. L. *RSC Adv.* **2014**, *4*, 7313-7320.

18.   Xu, Y.; Ma, J. Q.; Xu, Y. F.; Xu, L.; Xu, L.; Li, H. X.; Li, H. *RSC Adv.* **2013**, *3*, 851-858.

19.   Forman, A. J.; Park, J. N.; Tang, W.; Hu, Y. S.; Stucky, G. D.; McFarland, E. W. *ChemCatChem* **2010**, *2*, 1318-1324.

20. Lee, I.; Zhang, Q.; Ge, J. P.; Yin, Y. D.; Zaera, F. *Nano Res.* **2011**, *4*, 115-123.

21. Layan Savithra, G. H.; Bowker, R. H.; Carrillo, B. A.; Bussell, M. E.; Brock, S. L. *ACS Appl. Mater. Interfaces* **2013**, *5*, 5403-5407.

22. Joo, S. H.; Park, J. Y.; Tsung, C. K.; Yamada, Y.; Yang, P. D.; Somorjai, G. A. *Nat. Mater.* **2009**, *8*, 126-131.

23. Shang, Z. Y.; Patel, R. L.; Evanko, B. W.; Liang, X. H. *Chem. Commun.* **2013**, *49*, 10067-10069.

24. Kahsar, K. R.; Schwartz, D. K.; Medlin, J. W. *J. Am. Chem. Soc.* **2014**, *136*, 520-526.

25. Vericat, C.; Vela, M. E.; Benitez, G.; Carro, P.; Salvarezza, R. C. *Chem. Soc. Rev.* **2010**, *39*, 1805-1834.

26. Schreiber, F. *Prog. Surf. Sci.* **2000**, *65*, 151-256.

27. Love, J. C.; Wolfe, D. B.; Chabinyc, M. L.; Paul, K. E.; Whitesides, G. M. *J. Am. Chem. Soc.* **2002**, *124*, 1576-1577.

28. Cargnello, M.; Wieder, N. L.; Montini, T.; Gorte, R. J.; Fornasiero, P. *J. Am. Chem. Soc.* **2010**, *132*, 1402-1409.

29. Liang, X. H.; Zhou, Y.; Li, J. H.; Weimer, A. W. *J. Nanopart. Res.* **2011**, *13*, 3781-3788.

30. Wang, X. F.; Zhao, H. Y.; Wu, T. P.; Liu, Y. Z.; Liang, X. H. *Catal. Lett.* **2016**, *146*, 2606-2613.

31. Liang, X. H.; Hakim, L. F.; Zhan, G. D.; McCormick, J. A.; George, S. M.; Weimer, A. W.; Spencer, J. A.; Buechler, K. J.; Blackson, J.; Wood, C. J.; Dorgan, J. R. *J. Am. Ceram. Soc.* **2007**, *90*, 57-63.

32. Liang, X. H.; King, D. M.; Li, P.; George, S. M.; Weimer, A. W. *AIChE J.* **2009**, *55*, 1030-1039.

33. Liang, X. H.; Yu, M.; Li, J. H.; Jiang, Y. B.; Weimer, A. W. *Chem. Commun.* **2009**, *46*, 7140-7142.

34. Liang, X. H.; Li, J. H.; Yu, M.; McMurray, C. N.; Falconer, J. L.; Weimer, A. W. *ACS Catal.* **2011**, *1*, 1162-1165.

35. Marshall, S. T.; O'Brien, M.; Oetter, B.; Corpuz, A.; Richards, R. M.; Schwartz, D. K.; Medlin, J. W. *Nat. Mater.* **2010**, *9*, 853-858.

36. Love, J. C.; Wolfe, D. B.; Haasch, R.; Chabinyc, M. L.; Paul, K. E.; Whitesides, G. M.; Nuzzo, R. G. *J. Am. Chem. Soc.* **2003**, *125*, 2597-2609.

37. Wirde, M.; Gelius, U.; Nyholm, L. *Langmuir* **1999**, *15*, 6370-6378.

SUPPORTING INFORMATION

Experimental

Pt atomic layer deposition (ALD) process: Platinum nanoparticles were deposited on porous γ-alumina particles by ALD in a fluidized bed reactor,[1] as described in detail elsewhere.[2] The alumina particles were about 40 μm in diameter, and their Brunauer-Emmett-Teller (BET) surface area was 95.5 m^2g^{-1}. Methylcyclopentadienyl-(trimethyl) platinum (IV) and oxygen were the precursors for Pt ALD. One cycle of Pt ALD was applied at 300 °C. For the γ-Al_2O_3 nanoparticles supported Pt nanoparticles, four cycles of Pt ALD were applied at the same temperature using the same precursors.

Self-assembled monolayers (SAMs) coating: SAMs were deposited on the surface of the Pt nanoparticles by immersing the Pt/γ-alumina particles in a 10 mM ethanol solution of hexanethiol for 24 hours. Then, the samples were rinsed (using ethanol to remove non-chemisorbed thiols) and dried under a nitrogen flow.

Aluminum alkoxide (alucone) molecular layer deposition (MLD) process: The alucone MLD films were coated on Pt/γ-alumina particles and SAMs-treated Pt/γ-alumina particles by alternatively introducing trimethylaluminum (TMA) and ethylene glycol (EG) into the fluidized bed reactor at 160 °C. Different cycles (30, 40, and 50) of alucone MLD films were applied.

Formation of porous alumina films: The SAMs and organic components in the films were removed by oxidation in air at 400 °C. During the oxidation process, the samples were heated from room temperature to 400 °C, at a rate of 1 °C min^{-1}, and cooled down to room temperature, at the same rate, after being kept at 400 °C for one hour. The catalysts formed with three corresponding thicknesses of ultra-thin porous shells and gaps between the Pt nanoparticles and the porous shells.

Hydrogenation of olefins: The nanostructured catalysts were applied for hydrogenation reactions of n-hexene (>99%) and cis-cyclooctene (>95%). The hydrogenation reactions occurred in an unstirred mini batch reactor (about 2 mL) assembled from Swagelok® stainless steel parts. The reactor was connected to a three-way valve, with one port connected to a regulated hydrogen cylinder and the other port opened to air. In a typical test, n-hexene or cis-cyclooctene (~0.08 g), ethyl acetate (~0.78 g), and the catalysts (~0.007 g) were added to the reactor. The mass ratio of Pt to olefin was about 2/1000. All catalysts had an identical Pt loading, even though the total catalyst mass within the reactor increased as the number of MLD cycles increased.

The reactor was first opened to a regulated hydrogen cylinder that pressurized the reactor to 20 psi (relative pressure) and then opened it to air to depressurize the reactor to atmospheric pressure. After flushing the reactor with hydrogen (following the above steps) for 30 times, 99.999% of the air in the reactor was replaced by hydrogen gas. Control experiments indicated that no catalytic reactions occurred during this flushing process, and the losses of reactants and the solvent were negligible. The reaction was carried out at 1 atm of hydrogen and 35 °C for 24 hours. After the reaction, the catalysts were filtered off and the filtrate was analyzed to determine the reaction rate and selectivity, using a gas chromatograph (Agilent, 6890N), equipped with a 30 m DB-5 column and a FID detector.

CO oxidation reactions: The CO oxidation reactions were carried out in a fixed bed quartz reactor with quartz wool supporting the catalysts. Similar to the hydrogenation reactions, different amounts of catalysts (with different thicknesses of coating) were used for the reactions to assure an identical Pt loading. The catalysts (~35 mg) were diluted with 0.5 g of quartz sands (60-120 mesh) to make certain that the catalysts were uniformly distributed. The temperature was measured with a thermal couple. First, the catalysts were oxidized at 400 °C for 30 min in 10% O_2/90% He and then reduced in 50% H_2/50% He (total 50 sccm) for 30 min at the same temperature. Then, the reactor was cooled to 30 °C in a helium flow. A gas mixture, with 4% CO, 4% O_2 and 92% He of a total flow rate of 50 sccm, was introduced into the reactor for CO oxidation reaction. MKS® mass flow controllers were used to control the gas flow rate. Reactions were at a temperature of 30 °C to a temperature at which the CO conversion reached 100%. Reaction products were

analyzed by an online gas chromatograph (SRI 8610C) equipped with a 6 feet HAYESEP

D column, a 6 feet MOLECULAR SIEVE 13X column, and a FID detector.

Characterization

Nitrogen adsorption and desorption: The nitrogen adsorption and desorption

isotherms of catalyst particles were obtained at -196 °C. The surface areas of the samples

were calculated using the BET method in a relative pressure range of 0.05–0.25. The size

distributions of micropores and mesopores were determined using the Horvath and

Kawazoe (HK) method and the Barrett-Joyner-Halenda (BJH) method, respectively. The

total pore volume was calculated from the adsorption quantity at a relative pressure of

P/P_0= 0.99.

With the deposition of Pt nanoparticles on the porous γ-alumina support, the pore

volume and surface area of the sample decreased slightly from 0.28 cm^3g^{-1} to 0.27 cm^3g^{-1},

and from 95.5 m^2g^{-1} to 94.3 m^2g^{-1}, respectively (Figure 2b). The surface area and pore

volume decreased (84.3 m^2g^{-1} and 0.23 cm^3g^{-1}) with SAMs coating on the surface of the Pt

nanoparticles. These decreases in the pore volume and surface area were due to the

blockage of small pores (Figure 2c) and the reduction in size of the mesopores in the

catalyst support (Figure S1) caused by the SAMs. The pore volume and surface area further

decreased after 30 cycles of MLD coating were deposited on the SAMs-treated sample.

This trend continued with increases in the number of MLD cycles (Figure S2). As shown

in Figure S1, the pore volume and the size of larger pores decreased with increases in the

number of MLD cycles. The total pore volume for micropores also decreased with MLD

coating (Figure S3), since the MLD films had a dense structure before oxidation. As shown in Figure 2b, the sample with 30 cycles of MLD coating after oxidation had a larger surface area (85.6 m^2g^{-1}) and pore volume (0.24 cm^3g^{-1}) than the SAMs-treated sample and the sample coated with 30 cycles of MLD films before oxidation. This increase was due to the fact that both the SAMs and the organic components of the MLD films were removed during the oxidation process. The pore size of the porous shell was about 0.6 nm, as we reported earlier.[3] Similar results were observed for the samples coated with a larger number of MLD coating cycles. The pore volume and surface area decreased with an increase in the number of MLD coating cycles. As shown in Figure 2c, more micropores (about 0.6 nm in diameter) were observed after the oxidation process. These new pores could have resulted partly from the porous shell formed after oxidation and partly from the intrinsic pores recovered after the SAMs were removed. The γ-alumina support itself has micropores with 0.6 nm in diameter (Figure S3), and this is the reason why the micropore size distribution of the catalyst did not change after the deposition of porous alumina film.

Transmission electron microscopy (TEM) on dense alumina supported samples: In order to observe the porous films and the gaps between the Pt nanoparticles and the porous shell, Pt nanoparticles were deposited on dense alumina nanoparticles by ALD. Larger Pt nanoparticles were synthesized by applying four cycles of Pt ALD on the substrate for ease in observing the Pt nanoparticles and porous films with TEM. As shown in Figure S5a, Pt nanoparticles (average particle size ~3 nm) were uniformly dispersed on the substrate surface. SAMs were deposited on the Pt nanoparticles supported on the dense alumina

nanoparticles, following the same steps mentioned above. Then, 50 cycles of alucone MLD films were employed on the SAMs-treated Pt/dense-alumina nanoparticles. After removal of the SAMs and organic components from the alucone MLD films by oxidation, gaps (~0.4 nm) between the Pt nanoparticles and porous alumina films could be observed (Figure S5b-d). For comparison, another sample of porous alumina coated Pt/dense-alumina nanoparticles without gaps was synthesized and no gaps between the Pt nanoparticles and the porous alumina films could be observed after oxidation (Figure S5e). For the porous alumina coated Pt/dense-alumina nanoparticles without gaps, the porous film could be observed on the Pt nanoparticles with a film thickness of about 2 nm, which was thinner than the expected value (~5 nm). This could be due to the lack of functional groups on the Pt nanoparticles, which are necessary to initiate the alucone MLD coating process. Therefore, the first few cycles of coating deposited preferentially onto the most energetic (e.g., edge) sites rather than uniformly blanketing the Pt particles entirely. There could be one nucleation period, which would slow down the MLD film growth rate. The porous film, formed on the coated sample with gaps, was thinner than the coated samples without gaps. This could be due to the fact that after the SAMs deposition, the surface functional groups of the sample were reduced and a longer nucleation period was needed. This could also explain why more alucone MLD cycles were needed to achieve the high selectivity of the catalyst with SAMs, as compared to the catalyst without SAMs in our previous report.[4]

CO-chemisorption: CO-chemisorption was carried out using a Micromeritics AutochemII 2920 to investigate the Pt dispersion of the naked catalyst and the catalysts coated with porous alumina films formed from 50 cycles of alucone MLD coating, both with and without gaps. All three catalysts were reduced at 350 °C for 0.5 h and degassed at the same temperature in pure He for 1.5 h. The CO adsorption isotherms were obtained at 50 °C and the stoichiometry of Pt:CO was assumed to be 1:1.

X-ray photoelectron spectroscopy (XPS) analysis: The XPS spectra of hexanethiol-treated porous γ-alumina, hexanethiol-treated Pt/γ-alumina particles (before and after oxidation) were recorded with a Kratos Axis 165 X-ray photoelectron spectrometer, using a monochromatic Al Kα radiation (hν = 1486.6 eV), at a take-off angle of 0°. The survey scan spectra and C (1s), S (2p) core level spectra were recorded at a pass energy of 160 eV and 40 eV, respectively. All binding energy values were corrected based on C 1s signal at 284.5 eV.
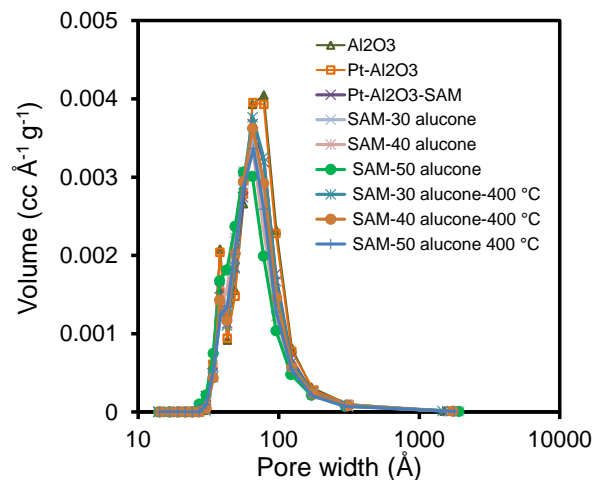
Figure S1. Pore size distribution (for pore sizes larger than 2 nm) of the Pt/γ-alumina particles coated with SAMs and different thicknesses of MLD films (before and after oxidation).
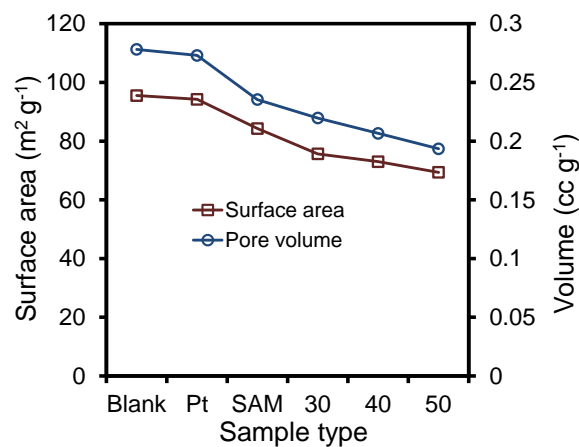
Figure S2. Surface areas and pore volumes of the naked Pt/γ-alumina particles and coated with different thicknesses of MLD films (without oxidation).
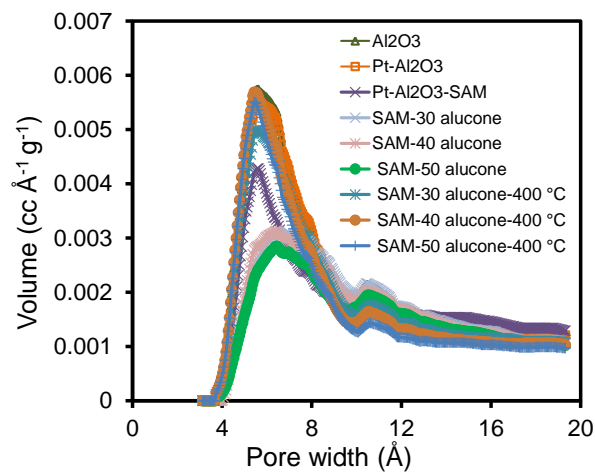
Figure S3. Pore size distribution (for pore sizes smaller than 2 nm) of the Pt/γ-alumina particles coated with SAMs and different thicknesses of MLD films (before and after oxidation).
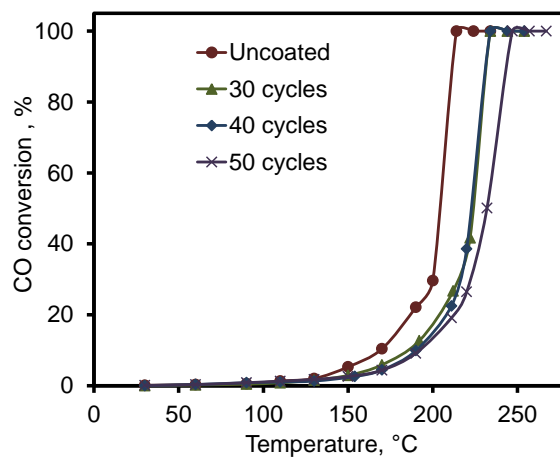
Figure S4. CO conversion of CO oxidation catalyzed by naked Pt/γ-alumina particles and coated with different thicknesses of porous films (without gaps).
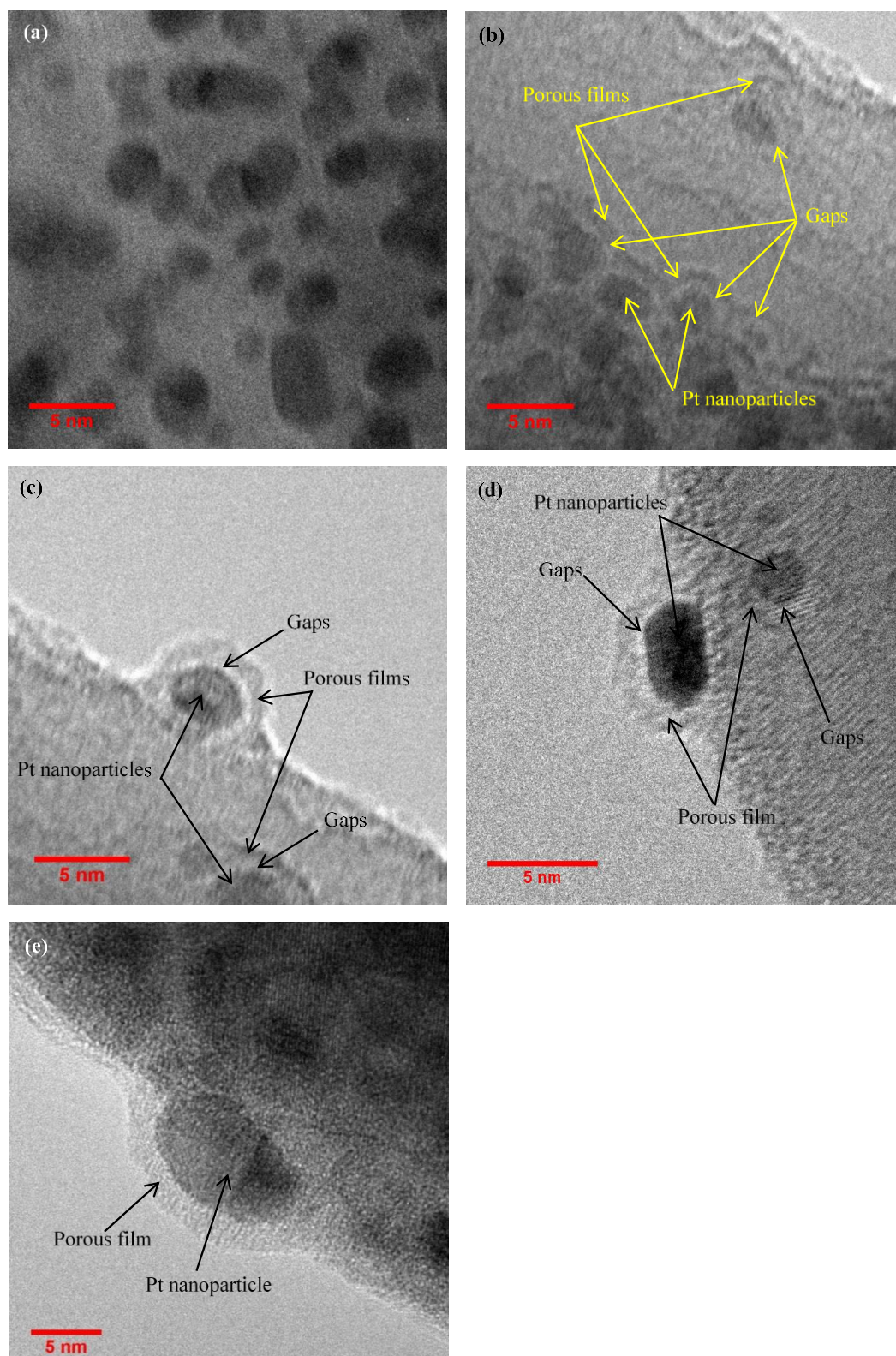
Figure S5. TEM images of (a) Pt/dense-alumina nanoparticles, (b, c, d) Porous alumina coated Pt/dense-alumina nanoparticles with gaps, and (e) Porous alumina coated Pt/dense-alumina nanoparticles without gaps.
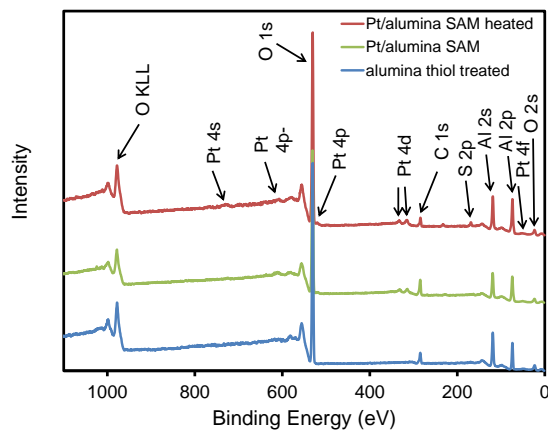
Figure S6. XPS spectra survey scan of thiol-treated porous γ-alumina support, and thiol-treated Pt/γ-alumina before and after oxidation.
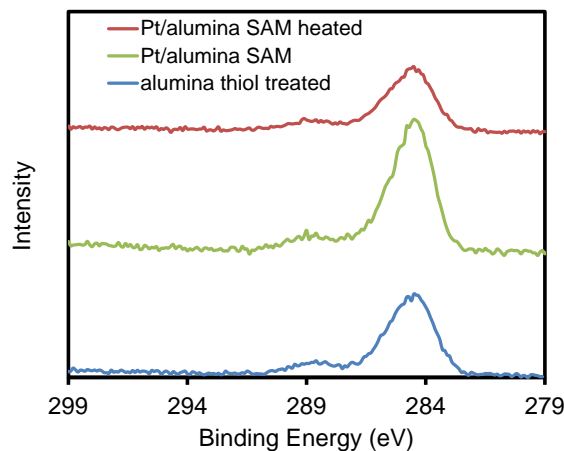
Figure S7. XPS spectra high resolution of carbon (1s) of thiol-treated porous γ-alumina, and thiol-treated Pt/γ-alumina before and after oxidation.

REFERENCES

1. Liang, X. H.; Zhou, Y.; Li, J. H.; Weimer, A. W. *J. Nanopart. Res.* **2011**, *13*, 3781-3788.

2.   Liang, X. H.; Hakim, L. F.; Zhan, G. D.; McCormick, J. A.; George, S. M.; Weimer, A. W.; Spencer, J. A.; Buechler, K. J.; Blackson, J.; Wood, C. J.; Dorgan, J. R. *J. Am. Ceram. Soc.* **2007**, *90*, 57-63.

3.   Liang, X. H.; Yu, M.; Li, J. H.; Jiang, Y. B.; Weimer, A. W. *Chem. Commun.* **2009**, *46*, 7140-7142.

4.   Shang, Z. Y.; Patel, R. L.; Evanko, B. W.; Liang, X. H. *Chem. Commun.* **2013**, *49*, 10067-10069.

III. CHEMOSELECTIVE TRANSFER HYDROGENATION OF NITROARENES CATALYZED BY HIGHLY DISPERSED, SUPPORTED NICKEL NANOPARTICLES

Chengjun Jiang,[†,§] Zeyu Shang,[‡, §] and Xinhua Liang*[,‡]

[†] Department of Chemical and Biological Engineering, Zhejiang University of Science & Technology, Hangzhou, Zhejiang 310023, People's Republic of China

[‡] Department of Chemical and Biochemical Engineering, Missouri University of Science and Technology, Rolla, Missouri 65409, United States

[§] C.J. and Z.S. contributed equally.

* E-mail: liangxin@mst.edu

ABSTRACT

A recyclable highly dispersed Ni/SiO_2 catalyst was prepared by atomic layer deposition. Chemoselective reduction of nitroarenes was studied using the prepared Ni/SiO_2 as the catalyst and hydrazine hydrate as a hydrogen donor. Different kinds of nitroarenes were converted to the corresponding anilines with high yields. The high activity of the catalysts could be resulted from the highly dispersed Ni nanoparticles.

Keywords: atomic layer deposition (ALD), nickel nanoparticles, heterogeneous catalysis, chemoselective, transfer hydrogenation, nitroarenes

1. INTRODUCTION

Aromatic amines are useful intermediates in the preparation of dyes, pharmaceuticals, and agricultural chemicals, which can be obtained by the reduction of aromatic nitro compounds. A variety of procedures involving metal catalysts and other reducing agents are available for this purpose.[1-4] However, the selective reduction of a nitro group in the presence of other reducible functional groups in a molecule is a challenging task. In addition, reduction of aromatic nitro compounds often stops at an intermediate stage, yielding hydroxylamines, hydrazines, azoarenes, or azoxyarenes as by-products.[5-7] Recently, many catalysts involving metal nanoparticles (e.g., Au,[8-10] Ag,[11] Fe,[12] Fe-Ni,[13] Ni-B,[14, 15] Ru,[16, 17] and Pd[18, 19]) have been employed for the reduction of nitro groups. Among the catalysts, gold showed the highest activity and selectivity. However, gold is a noble metal and very expensive. Nickel and iron are good reducing agents and much cheaper than gold. Various liquid phase based methods were applied to prepare Ni and Fe nanoparticle catalysts for the reduction of nitroarenes. These catalysts showed relatively high selectivity toward aromatic amines, but the activity was much lower than that of gold.[12-14] It is very important that an efficient, cost-effective and chemoselective catalyst be developed for the hydrogenation of nitroarenes.

Atomic layer deposition (ALD) is a layer-by-layer gas phase process, which has been employed to uniformly deposit conformal films on porous nanostructures.[20, 21] The growth of these films can be controlled at atomic level through self-limiting, sequential binary reactions on the substrate surface. ALD also allows the uniform deposition of highly

dispersed metal nanoparticles (2 nm or smaller). Metal nanoparticles, such as Pt and Pd, have been successfully deposited on a porous substrate by ALD.[22, 23] This is very important for the metal nanoparticles in catalysis application, especially for supported catalysts.[22] These advantages have expanded the ALD applications in the catalysis area. As a part of our effort in this area, we demonstrated excellent performance of platinum nanoparticles deposited by ALD for different liquid phase catalytic reactions.[24, 25] Recently, Gould et al.[26] demonstrated that Ni nanoparticles deposited by ALD had excellent performance in propylene hydrogenolysis reactions. It was demonstrated that smaller metal nanoparticles showed higher activity for hydrogenation of nitroarenes.[11, 27] It is expected that nickel nanoparticles, deposited by ALD, would have excellent properties for the reduction of NO_2 groups.

Here, we report the chemoselective reduction of aromatic nitro compounds to corresponding anilines by highly dispersed ALD nickel nanoparticles, supported on SiO_2 in combination with a convenient hydrogen donor. The reaction conditions were optimized using different amounts of hydrazine hydrate. Reduction reactions of different nitroarenes were studied to evaluate the performance of the catalysts.

2. EXPERIMENTAL SECTION
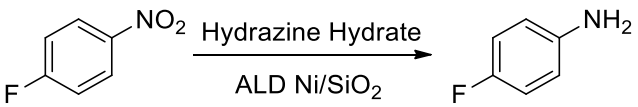
2.1. Materials. All solvents, hydrazine hydrate and reactants were provided by J&K Chemical. Silica nanoparticles (20 to 30 nm in diameter) and silica gel particles were purchased from US Research Nanomaterials and Sigma Aldrich, respectively. The silica

gel particles were 30-75 μm in diameter with an average pore size of 15 nm and a Brunauer-Emmett-Teller (BET) surface area of about 270 m^2/g. Bis(cyclopentadienyl)nickel was purchased from Alfa Aesar.

2.2. Ni nanoparticles Deposited on SiO2 by ALD. Ni ALD was carried out using bis(cyclopentadienyl)nickel ($NiCp_2$) and hydrogen as precursors at 300 °C in a fluidized bed reactor. The ALD reactor system was described in detail previously.[28] Both silica nanoparticles (20-30 nm) and porous silica gel particles were used as substrates. In this study, one cycle of Ni ALD was applied on silica gel particles and different cycles of Ni ALD were applied on silica nanoparticles. The details of Ni ALD are introduced in the Supporting Information.

2.3. General Procedure of Nitroarenes Reduction with Hydrazine Hydrate Catalyzed by Ni/SiO2. Hydrazine hydrate was chosen as the hydrogen donor for the reduction of aromatic nitro compounds. Ni supported on silica gel particles was applied to catalyze the reaction. In a typical reaction, nitroarenes (6 mmol), NH_2NH_2 (4-8 equivalents), ethanol (10 mL) and Ni/SiO$_2$ catalysts (10 mg) were added into a sealed copper tube with an open end and 12 mL in volume. The reaction was carried out at atmospheric pressure and an appropriate temperature (see Table 1). The products of the reaction were monitored by a LC-20AT high-performance liquid chromatography (HPLC) equipped with a Hypersil ODS (C18) column and SPD-20A/20AV UV-VIS detector. Methanol and water (80% methanol and 20% water) were employed as the mobile phase at a flow rate of 1 mL/min. The mixture was separated at 25 °C with 254 nm as the detection

Table 1. Evaluation of the Effects of Hydrazine Amounts and Solvent on the Reduction of 4-Fluoronitrobenzene to p-Fluoroaniline Catalyzed by One Cycle of Ni ALD-Deposited on Silica Gel Particles.[a]

Entry	Catalyst	Tem(°C)	Solvent	NH_2NH_2	Selectivity(%)	Yield(%)
1	No catalyst	100	EtOH	4 eq.	0	0
2	Ni/SiO_2	60	EtOH	4 eq.	98.1	59.2
3	Ni/SiO_2	80	EtOH	4 eq.	97.8	75.8
4	Ni/SiO_2	100	EtOH	4 eq.	98.2	95.0
5	Ni/SiO_2	120	EtOH	4 eq.	97.9	71.7
6	Ni/SiO_2	100	EtOH	6 eq.	98.1	96.5
7	Ni/SiO_2	100	EtOH	8 eq.	98.2	97.8
8	Ni/SiO_2	100	THF	8 eq.	97.5	92.7
9	Ni/SiO_2	100	CH_3OH	8 eq.	97.9	94.2
10	Ni/SiO_2	100	t-BuOH	8 eq.	98.5	95.8
11	Recycle1	100	EtOH	8 eq.	98.5	95.7
12	Recycle2	100	EtOH	8 eq.	98.0	95.2
13	Recycle3	100	EtOH	8 eq.	97.8	94.3
14	Recycle4	100	EtOH	8 eq.	97.2	94.0

[a]Reaction conditions: 6 mmol nitroarenes, 4-8 equivalents NH_2NH_2, 10 mL solvent and 10 mg Ni/SiO_2 catalysts (except entry 1) were added into the reactor. The reactions were carried out at different temperatures for 8 hr.

wavelength. The identities of all products were compared with authentic samples. For the recycling studies of 4-fluoronitrobenzene reduction with hydrazine hydrate, the reaction conditions were as follows: 6 mmol of 4-fluoronitrobenzene, 10 mg of Ni/SiO_2, 48 mmol of hydrazine hydrate (in each cycle), and 10 mL of ethanol, for 8 hr at 100 °C. After each

run, the catalyst (Ni/SiO$_2$) was isolated by a magnet and rinsed thoroughly with ethanol, since the Ni/SiO$_2$ particles were highly magnetic.

2.4. Catalyst Characterization. Inductively coupled plasma-atomic emission spectroscopy (ICP-AES) was employed to analyze the Ni content of the catalysts. The Ni particles were directly observed by high resolution transmission electron microscopy (HRTEM). X-ray photoelectron spectroscopy (XPS) was applied to verify the composition of Ni on the silica particles. Fourier transform infrared spectroscopy (FTIR) was employed to verify the complete removal of the organic ligand from the ALD precursor.

3. RESULTS AND DISCUSSION

3.1. Characterization of Ni/SiO$_2$. The ICP-AES result showed that the Ni loading of one cycle of Ni ALD on the silica gel particles was 0.73 wt.%. Figure 1 shows the HRTEM images of ALD deposited Ni nanoparticles (2 cycles and 15 cycles) on 20-30 nm silica nanoparticles and the size distribution of Ni nanoparticles. The average size of Ni nanoparticles was 2.4 nm and 2.6 nm for the 2 cycle- and 15 cycle-sample, respectively. This particle size was similar to the values reported by Gould et al.[26] We believe that the average size of Ni nanoparticles deposited on silica gel particles, with only 1 cycle of Ni ALD, should be about 2.4 nm, or even smaller. The TEM images also indicated that the Ni nanoparticles were highly dispersed on the silica support. Figure S1 shows the Ni (2p) high resolution XPS spectrum for Ni supported on a silica gel sample. Carbon peaks were also observed on the survey scan of the XPS spectrum (Figure S2). To verify whether there

were substantial organic ligands from the Ni precursor left on Ni particles, FTIR was applied to analyze the organic groups. Figure S3 shows that there were no characteristic peaks for the cyclopentadienyl group. This means that all organic groups of the precursor were removed during the ALD hydrogen reduction process.

3.2. Catalytic Reduction of 4-Fluoronitrobenzene. To optimize the reaction conditions, the reduction of 4-fluoronitrobenzene was initially investigated with different amounts of hydrazine, and different solvents at different temperatures (Table 1). Ni/silica gel particles were used as catalysts in all catalytic reactions. The recyclability of the catalyst was also investigated by recycling the catalyst for reduction of 4-fluoronitrobenzene. As shown in Table 1, the control experiment shows that no reaction was processed without a catalyst. Temperature was a key factor in the reduction of 4-fluoronitrobenzene. At 60 °C, when 4 equivalents of hydrazine hydrate were added, the selectivity to p-fluoroaniline was 98.1%, and the yield was only 59.2%. The yield increased with increases of temperature up to 100 °C (75.8% at 80 °C and 95.0% at 100 °C). However, both selectivity and yield decreased at 120 °C, which was due to some side reactions at higher temperatures. Based on this initial study, 100 °C was selected as the reaction temperature in the following studies. At 100 °C, the yield increased to 96.5% and 97.8% when the hydrazine amount was increased to 6 and 8 equivalents, respectively. Solvents normally have a significant influence on the performance of the catalyst.[29, 30] In this study, different solvents (Tetrahydrofuran (THF), methanol, and tertiary butanol) were used for this reaction. The selectivity and yield showed no significant differences, which indicated that the solvents
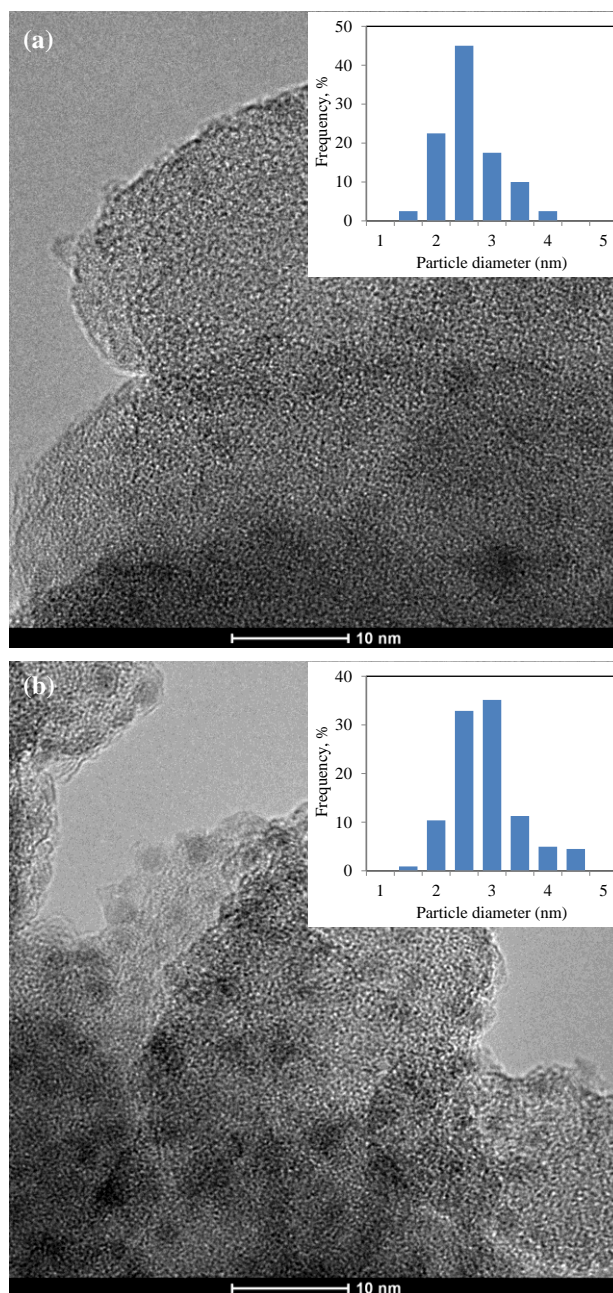
Figure 1. HRTEM images of (a) 2 cycles and (b) 15 cycles of ALD deposited Ni nanoparticles on 20-30 nm silica particles. The inset images show the size distribution of Ni nanoparticles.

would not affect this reaction in this catalytic system. The ALD prepared Ni/SiO$_2$ catalysts were highly magnetic. Therefore, the catalyst particles could be easily collected using a

magnet for separation. The catalyst particles were recycled four times. Both the selectivity and yield only slightly decreased after cycling, as shown in Table 1, which indicated that the ALD prepared Ni/SiO$_2$ catalysts could maintain good activity and stability in the liquid phase reactions.

3.3. Reduction of Nitro Compounds into Amines with Hydrazine Hydrate Catalyzed by Ni/SiO$_2$. In order to investigate and determine the scope and limitations of this reductive methodology, a series of nitroarenes were examined. As shown in Table 2, for a reaction time of 8 hr, the selectivity and yield of most nitroarene reduction reactions were higher than 90%. For example, the selectivity and yield of aniline was 95.2% and 93.8%, respectively. Turnover frequency (TOF), which is defined as the reactant molecules reacting per active site in unit time, was calculated to investigate and determine the activity of the catalyst (Table 2). The conversion of nitroarenes was close to 100% for 8 hr of reaction; thus, it would not be accurate to calculate TOF at that high conversion. To calculate an accurate TOF, reactions were also carried out for 2 hr. The active metal surface area (ASA) and dispersion of the catalysts were calculated by using the measured size of Ni nanoparticles in Equations 1 and 2:[26]

$$\text{ASA}\,[m^2/g] = \frac{L \times f}{d \times z} \tag{1}$$
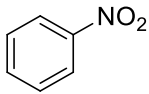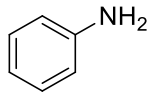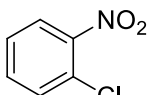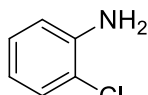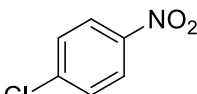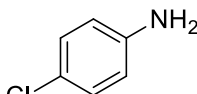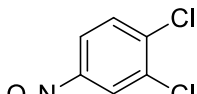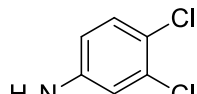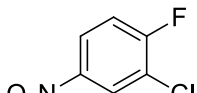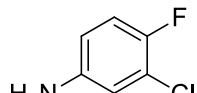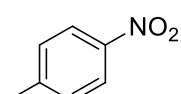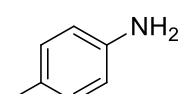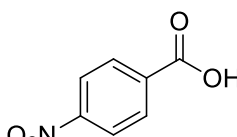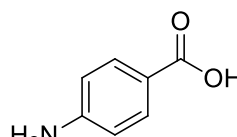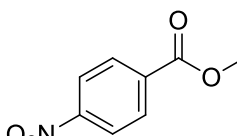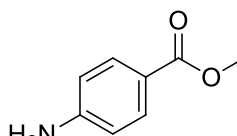
$$\text{Dispersion}\,[\%] = \frac{ASA \times M}{N \times A \times L} \tag{2}$$

where L is the weight fraction of metal loading, f is the particle shape correction factor (f = 6 for a sphere), d is the average diameter of the supported particles measured by TEM (assume the size of Ni particles on silica gel is 2.4 nm), z is the metal density, M is the

formula weight of the supported metal, N is Avogadro's number and A is the metal atomic

surface area (for Ni, $A = 6.494$ Å^2/atom). Base on Equation 1, the ASA for the Ni/SiO$_2$

catalyst is 2.05 m^2/g. The metal dispersion was then calculated from Equation 2 to be 42%.

Based on the conversion and reaction time (conversion at a reaction time of 2 hr), TOF was

calculated. As shown in Table 2, almost all of the TOF of entry 1-8 were higher than 0.7 s^{-1}, which is pretty high in the reduction of nitroarene systems.

Liu et al.[9] applied Au/meso-CeO$_2$ as the catalyst for the reduction of nitrobenzene

and got a TOF of 20 h^{-1} (5.56×10^{-3} s^{-1}). Petkar et al.[13] employed Fe-Ni bimetallic system

to catalyze the reduction of aromatic nitro compounds and got a TOF of 4.76×10^{-3} s^{-1} for

nitrobenzene. As shown in Table 2, the TOF of nitrobenzene in our system was 0.78 s^{-1},

which was more than two orders of magnitude higher than the reported values. The high

catalytic activity of the catalysts could be due to the highly dispersed Ni nanoparticles

prepared by ALD. In the above-mentioned previous studies, the metal nanoparticles

catalysts were normally prepared by the liquid impregnation method and the metal

nanoparticles were very large. In our current study, the Ni nanoparticles were prepared by

ALD and the particle sizes were smaller than 3 nm. The effect of particle size on the

catalytic activity was reported previously. Mahata et al.[27] reported that smaller Ni

nanoparticles showed higher activity for hydrogenation of nitroarenes. Shimizu et al.[11] also

demonstrated that catalyst activity increased with the decrease in silver nanoparticle size

for hydrogenation of nitroarenes. In addition, Gould et al. reported that the surface

Table 2. Chemoselective Reduction of Nitro Compounds to Amines with Hydrazine Hydrate Catalyzed by 1 Cycle of Ni ALD-Deposited on Silica Gel Particles.

$$R\!-\!NO_2 \xrightarrow[\text{ALD Ni/SiO}_2]{\text{Hydrazine Hydrate}} R\!-\!NH_2$$

Entry	Reactant	Product	Selectivity (%)[a]	Yield (%)[b]	TOF (s^{-1})[c]
1	nitrobenzene	aniline	95.2 (95.8)	93.8 (45.4)	0.78
2	2-chloronitrobenzene	2-chloroaniline	94.2 (94.5)	92.7 (42.7)	0.75
3	4-chloronitrobenzene	4-chloroaniline	94.0 (95.0)	91.9 (41.5)	0.72
4	3,4-dichloronitrobenzene	3,4-dichloroaniline	95.7 (95.5)	93.7 (42.6)	0.74
5	3-chloro-4-fluoronitrobenzene	3-chloro-4-fluoroaniline	96.0 (96.3)	94.7 (43.3)	0.74
6	4-nitrotoluene	4-aminotoluene	94.8 (94.9)	92.1 (41.1)	0.72
7	4-nitrobenzoic acid	4-aminobenzoic acid	87.1 (89.3)	74.8 (37.4)	0.69
8	methyl 4-nitrobenzoate	methyl 4-aminobenzoate	89.2 (90.5)	76.1 (38.7)	0.71

Reaction conditions: 6 mmol nitroarenes, 48 mmol NH$_2$NH$_2$, 10 mL ethanol and 10 mg Ni/SiO$_2$ catalysts were added into the reactor. The reactions were carried out at 100 °C for 2 hr and 8 hr, respectively. [a]Values in parenthesis are the selectivity of the reactions after 2 hr. [b]Values in parenthesis are the yields of the reactions after 2 hr. [c]TOF values were calculated using the results with reaction time of 2 hr.

structures of the ALD Ni nanoparticles were different from those of the larger Ni particles prepared by incipient wetness method.[26] This could also be a reason for the high catalytic activity of the catalysts.

The hydrogenation of nitroarenes often stops at an intermediate stage, yielding various by-products. For hydrogenation of halogenated nitroarenes, the hydrogenolysis of the C–X, in which X represents halogen, always happens.[31] Due to the high activity of ALD Ni nanoparticles, the hydrogenation of nitroarenes did not stop at the intermediate stage. The Ni nanoparticles also showed no activity in hydrogenolysis of the C-X bond in our current study, since no dehalogenation products were observed. Gawande et al.[32] also reported that no dehalogenation occurred in the hydrogenation of halogenated nitroarenes using Fe3O4-Ni nanoparticles. This was our hypothesis for the high selectivity of our ALD Ni catalysts. More studies are being conducted to reveal the effects of Ni particle size on the activity and selectivity of the reactions.

The ALD catalysts showed excellent selectivity and yield of the reduction of nitroarenes with fluorine and chlorine. In particular, no defluorination and dechlorination by-products were observed (entry 2-5) and the selectivities of all reactions were higher than 94%. This result was very good compared to other reported results with different kinds of catalyst systems in which the selectivity were always lower than 90%, or even lower.[9, 30, 33] The high selectivity of reaction is highly desirable in industry, because these by-products do not need to be separated, which is a costly process. For example, for entry 5, the product is solely 3-chloro-4-fluoro-benzenamine, which is a raw material for norfloxacin. The

effective control of defluorination and dechlorination could help provide high purity raw material for norfloxacin. However, the selectivity and yield of the transfer hydrogenations of p-nitrobenzoic acid and methyl p-nitrobenzoate were lower than 90% and 80%, respectively. This was largely possible due to the existence of other electron-withdrawing groups on the reactants molecules. Compared to the reported catalytic systems, our catalytic system is much simpler in terms of both catalyst preparation and experimental procedure. It is an efficient, cost-effective and chemoselective catalyst for the reduction of nitroarenes.

4. CONCLUSIONS

Highly dispersed nickel nanoparticles were deposited on both porous silica gel particles and 20-30 nm dense silica nanoparticles. The prepared Ni/silica gel catalysts can activate hydrazine hydrate as a reducing agent in the transfer hydrogenation of aryl nitro compounds into the corresponding amines with high selectivity and high yield. To the best of our knowledge, this is the first report of ALD prepared nickel nanoparticles for the transfer hydrogenation of aryl nitro compounds. The current work has extended the utility of a readily available catalyst (Ni/SiO$_2$) toward new applications in catalysis and organic chemistry.

ACKNOWLEDGEMENTS

REFERENCES

1. Jagadeesh, R. V.; Surkus, A.-E.; Junge, H.; Pohl, M.-M.; Radnik, J.; Rabeah, J.; Huan, H.; Schünemann, V.; Brückner, A.; Beller, M. *Science* **2013**, *342*, 1073-1076.

2. Junge, K.; Wendt, B.; Shaikh, N.; Beller, M. *Chem. Commun.* **2010**, *46*, 1769-1771.

3. Sakai, N.; Fujii, K.; Nabeshima, S.; Ikeda, R.; Konakahara, T. *Chem. Commun.* **2010**, *46*, 3173-3175.

4. Corma, A.; Concepción, P.; Serna, P. *Angew. Chem., Int. Ed.* **2007**, *46*, 7266-7269.
5. Yu, C.; Liu, B.; Hu, L. *J. Org. Chem.* **2001**, *66*, 919-924.

6. Saha, A.; Ranu, B. *J. Org. Chem.* **2008**, *73*, 6867-6870.

7. Lou, X.-B.; He, L.; Qian, Y.; Liu, Y.-M.; Cao, Y.; Fan, K.-N. *Adv. Synth. Catal.* **2011**, *353*, 281-286.

8. Cardenas-Lizana, F.; Gomez-Quero, S.; Keane, M. A. *Catal. Commun.* **2008**, *9*, 475-481.

9. Liu, X.; Ye, S.; Li, H.-Q.; Liu, Y.-M.; Cao, Y.; Fan, K.-N. *Catal. Sci. Technol.* **2013**, *3*, 3200-3206.

10. Boronat, M.; Concepción, P.; Corma, A.; González, S.; Illas, F.; Serna, P. *J. Am. Chem. Soc.* **2007**, *129*, 16230-16237.

11. Shimizu, K.-i.; Miyamoto, Y.; Satsuma, A. *J. Catal.* **2010**, *270*, 86-94.

12. Dey, R.; Mukherjee, N.; Ahammed, S.; Ranu, B. C. *Chem. Commun.* **2012**, *48*, 7982-7984.

13. Petkar, D. R.; Kadu, B. S.; Chikate, R. C. *RSC Adv.* **2014**, *4*, 8004-8010.

14. Wen, H.; Yao, K.; Zhang, Y.; Zhou, Z.; Kirschning, A. *Catal. Commun.* **2009**, *10*, 1207-1211.

15. Chen, L.-F.; Chen, Y.-W. *Ind. Eng. Chem. Res.* **2006**, *45*, 8866-8873.

16. Antonetti, C.; Oubenali, M.; Raspolli Galletti, A. M.; Serp, P.; Vannucci, G. *Appl. Catal., A* **2012**, *421-422*, 99-107.

17. Kim, J. H.; Park, J. H.; Chung, Y. K.; Park, K. H. *Adv. Synth. Catal.* **2012**, *354*, 2412-2418.

18. Lu, Y.-M.; Zhu, H.-Z.; Li, W.-G.; Hu, B.; Yu, S.-H. *J. Mater. Chem. A* **2013**, *1*, 3783-3788.

19. Hong, Y.; Sen, A. *Chem. Mater.* **2007**, *19*, 961-963.

20. George, S. M. *Chem. Rev.* **2010**, *110*, 111-131.

21. Liang, X. H.; George, S. M.; Weimer, A. W.; Li, N.-H.; Blackson, J. H.; Harris, J. D.; Li, P. *Chem. Mater.* **2007**, *19*, 5388-5394.

22. Liang, X. H.; Zhou, Y.; Li, J.; Weimer, A. W. *J. Nanopart. Res.* **2011**, *13*, 3781-3788.

23. Liang, X. H.; Lyon, L. B.; Jiang, Y.-B.; Weimer, A. W. *J. Nanopart.Rre.* **2012**, *14*, 943.

24. Liang, X. H.; Jiang, C. *J. Nanopart. Res.* **2013**, *15*, 1890.

25. Shang, Z.; Patel, R. L.; Evanko, B. W.; Liang, X. H. *Chem. Commun.* **2013**, *49*, 10067-10069.

26.   Gould, T. D.; Lubers, A. M.; Neltner, B. T.; Carrier, J. V.; Weimer, A. W.; Falconer, J. L.; Medlin, J. W. *J. Catal.* **2013**, *303*, 9-15.

27.   Mahata, N.; Cunha, A.; Orfao, J. J. M.; Figueiredo, J. L. *Appl. Catal., A* **2008**, *351*, 204-209.

28.   Liang, X. H.; Hakim, L. F.; Zhan, G.-D.; McCormick, J. A.; George, S. M.; Weimer, A. W.; Spencer, J. A. II; Buechler, K. J.; Blackson, J.; Wood, C. J.; Dorgan, J. R. *J. Am. Ceram. Soc.* **2007**, *90*, 57-63.

29.   Verho, O.; Nagendiran, A.; Tai, C.-W.; Johnston, E. V.; Bäckvall, J.-E. *ChemCatChem* **2014**, *6*, 205-211.

30.   Wienhöfer, G.; Sorribes, I.; Boddien, A.; Westerhaus, F.; Junge, K.; Junge, H.; Llusar, R.; Beller, M. *J. Am. Chem. Soc.* **2011**, *133*, 12875-12879.

31.   Takasaki, M.; Motoyama, Y.; Higashi, K.; Yoon, S.-H.; Mochida, I.; Nagashima, H. *Org. Lett.* **2008**, *10*, 1601-1604.

32.   Gawande, M. B.; Rathi, A. K.; Branco, P. S.; Nogueira, I. D.; Velhinho, A.; Shrikhande, J. J.; Indulkar, U. U.; Jayaram, R. V.; Ghumman, C. A. A.; Bundaleski, N.; Teodoro, O. M. N. D. *Chem. - Eur. J.* **2012**, *18*, 12628-12632.

33.   Jagadeesh, R. V.; Wienhöfer, G.; Westerhaus, F. A.; Surkus, A.-E.; Junge, H.; Junge, K.; Beller, M. *Chem. - Eur. J.* **2011**, *17*, 14375−14379.

SUPPORTING INFORMATION

Experimental Details

Ni ALD: Ni ALD was carried out using bis(cyclopentadienyl)nickel (NiCp$_2$) and hydrogen as precursors at 300 °C in a fluidized bed reactor, as described previously.[1] The solid NiCp$_2$ precursor was loaded in a heated bubbler and carried by nitrogen gas. Both silica particles (20-30 nm) and porous silica gel particles were used as substrates and

degassed under a nitrogen flow in the reactor before ALD reactions. The particle substrates were fully fluidized under a nitrogen flow, with the flow rate controlled by a mass flow controller. By introducing the $NiCp_2$ precursor into the reactor, the O-H bond of the hydroxyl groups on the substrate was replaced by an O-Ni bond due to the reaction of the $NiCp_2$ precursor and the O-H groups. During the nitrogen purge step, the excess $NiCp_2$ precursor was removed to prevent a chemical vapor deposition reaction of the excess $NiCp_2$ precursor and incoming hydrogen gas. In the next step, hydrogen was introduced to remove the organic ligands on Ni surfaces, reduce the Ni-O to metallic Ni, and regenerate the surface hydroxyl groups. A nitrogen purge process was also applied to remove excess hydrogen. This is the so-called one cycle of Ni ALD.

Characterization Details

XPS analysis: The XPS spectra of Ni on silica gel particles were recorded with a Kratos Axis 165 X-ray photoelectron spectrometer using a monochromatic Al Kα radiation (hν= 1486.6eV), at a take-off angle of 0°. The survey scan spectrum and Ni 2p core level spectrum were recorded at a pass energy of 160 eV and 20 eV, respectively. All binding energy values were corrected to C 1s signal (284.5 eV). As shown in Figure S1, the peaks at 855.7 eV and 860 eV represented NiO; a metallic Ni signal was observed at 853.1 eV.[2,3] This indicated that the Ni nanoparticles were partially oxidized in air. Carbon peaks were also observed from the survey scan data (Figure S2). The carbon was mainly from the background contamination, while some could have been from the organic ligands left on the Ni particles during the ALD process.

FTIR analysis: The FTIR spectrum was recorded using a Nicolet Nexus 470 FT-IR spectrometer. The spectrum was collected in the range of 4000-400 cm^{-1}. The transmittance was measured using a Ni/silica gel-containing potassium bromide pellet. The loading of Ni on silica was 1 wt. %. As shown in Figure S3, there were no characteristic peaks of the cyclopentadienyl group at 3043 and 3100 cm^{-1}.[4] No carbon chain peaks were observed. This indicated that the organic groups of the precursor were removed during the hydrogen reduction process and no substantial organic ligands bonded to Ni nanoparticles. The peak at 3440 cm^{-1} represented the O-H bond and the peak at 1634 cm^{-1} represented a deformation vibration peak of H-O-H from water.[5] The peak at 1870 cm^{-1} was a SiO_2 network vibration peak and the peaks at 1014 cm^{-1} and 563 cm^{-1} were Si-O stretching vibration peaks. The peaks at 966 cm^{-1} and 802 cm^{-1} represented a Si-O in-plane stretching vibration peak and a symmetric stretching vibration peak.[6] The peak at 1700 cm^{-1} represented C=O bond and the peak at 1267 cm^{-1} was the symmetric deformation vibration peak for the C-H bond.[6] These peaks could have been the organic components that had formed in the ALD reactions and were trapped by the porous structure of the substrate.

REFERENCES

1.   Liang, X. H.; Hakim, L. F.; Zhan, G.-D.; McCormick, J. A.; George, S. M.; Weimer, A. W.; Spencer, J. A., II; Buechler, K. J.; Blackson, J.; Wood, C. J.; Dorgan, J. R. *J. Am. Ceram. Soc.* **2007**, *90*, 57-63.

2.   Bakhmutov, V. I. *Solid-State NMR in Materials Science: Principles and Applications*. CRC Press, **2011**.

3.   Machet, A.; Galtayries, A.; Zanna, S.; Klein, L.; Maurice, V.; Jolivet, P.; Foucault, M.; Combrade, P.; Scott, P.; Marcus, P. *Electrochim. Acta.* **2004**, *49*, 3957-3964.

4.   Uusitalo, A.-M.; Pakkanen, T. T.; Iiskola, E. I. *J. Mol. Catal. A: Chem.* **2000**, *156*, 181-193.

5.   Socrates, G. *Infrared and Raman Characteristic Group Frequencies: Tables and Charts*. John Wiley & Sons, **2004**.

6.   Al-Oweini, R.; El-Rassy, H. *J. Mol. Struct.* **2009**, *919*, 140-145.
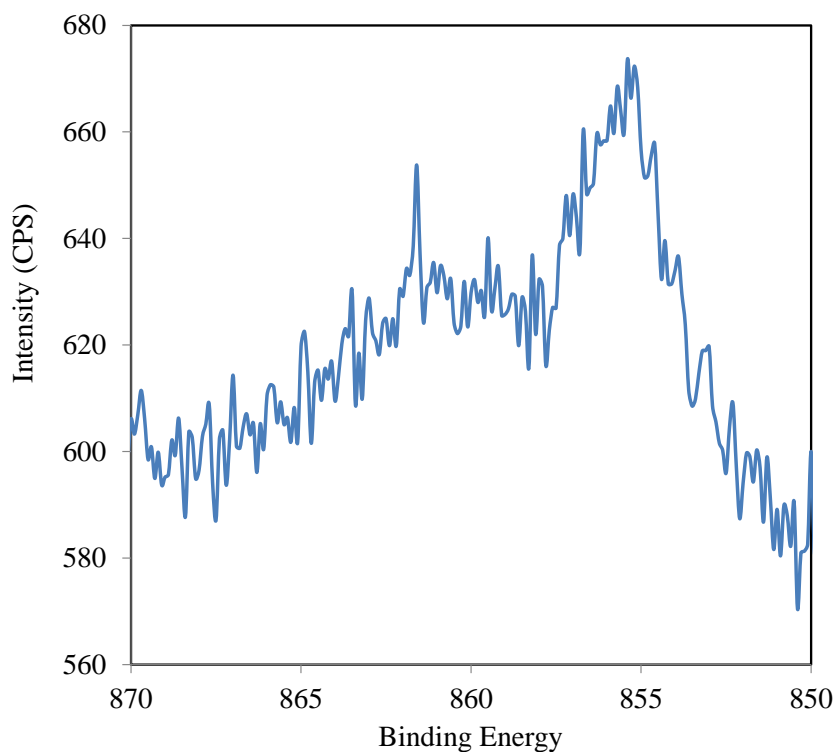
Figure S1. High resolution XPS spectrum of Ni (2p) for Ni supported on silica gel sample.
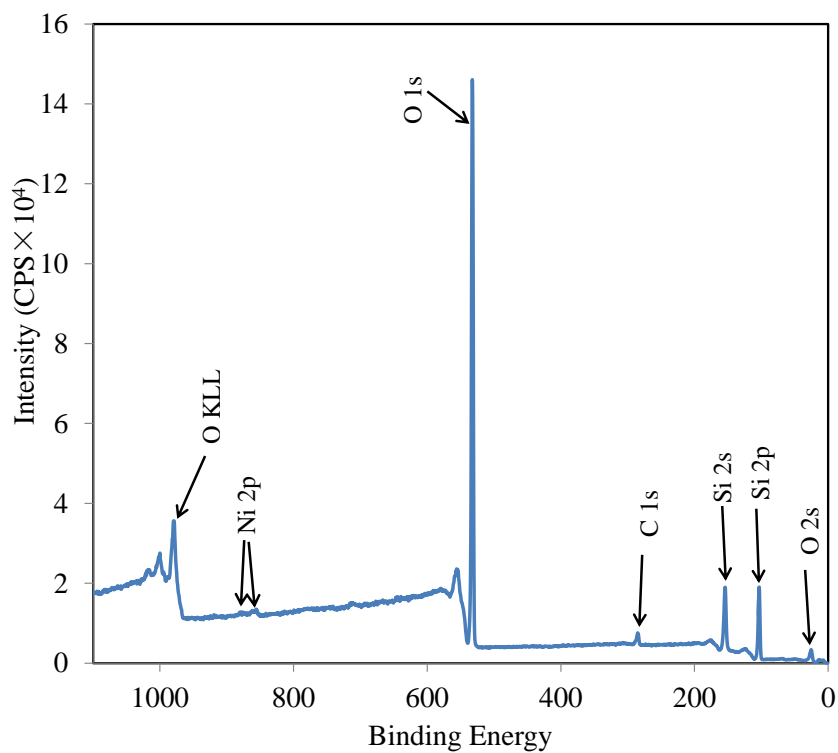
Figure S2. XPS spectrum of survey scan of Ni supported on silica gel sample.
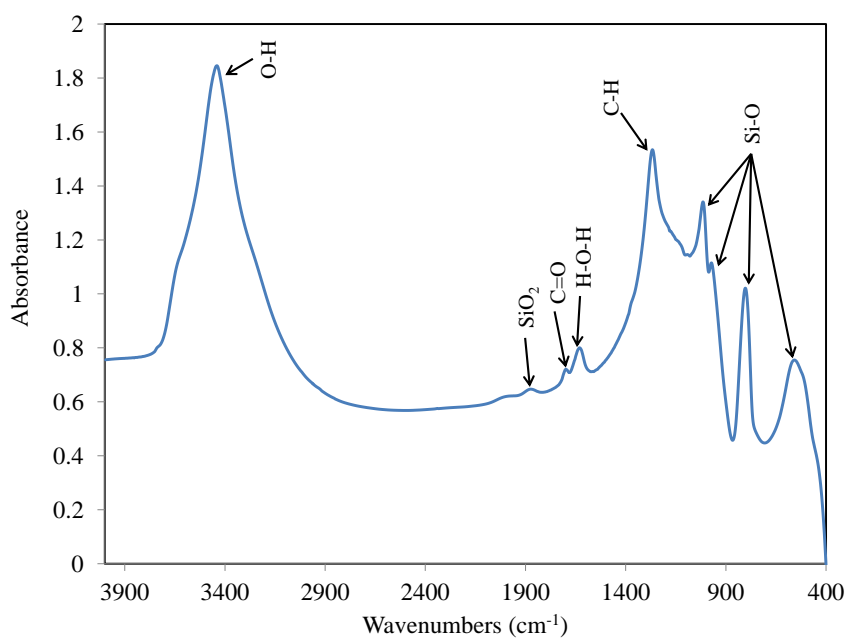
Figure S3. FTIR spectrum of Ni supported on silica gel sample.

IV. HIGHLY ACTIVE AND STABLE ALUMINA SUPPORTED NICKEL NANOPARTICLE CATALYSTS FOR DRY REFORMING OF METHANE

Zeyu Shang[a], Shiguang Li[b], Ling Li[c], Guozhu Liu[c], and Xinhua Liang[a,*]

[a] Department of Chemical and Biochemical Engineering, Missouri University of Science and Technology, Rolla, MO 65409, United States

[b] Gas Technology Institute, 1700 S Mount Prospect Road, Des Plaines, IL 60018, United States

[c] Key Laboratory for Green Chemical Technology of Ministry of Education, School of Chemical Engineering and Technology, Tianjin University, Tianjin 300072, PR China

* E-mail: liangxin@mst.edu

ABSTRACT

A highly stable and extremely active nickel (Ni) nanoparticle catalyst, supported on porous γ-Al_2O_3 particles, was prepared by atomic layer deposition (ALD). The catalyst was employed to catalyze the reaction of dry reforming of methane (DRM). The catalyst initially gave a low conversion at 850 °C, but the conversion increased with an increase in reaction time, and stabilized at 93% (1730 $Lh^{-1}g_{Ni}^{-1}$ at 850 °C). After regeneration, the catalyst showed a very high methane reforming rate (1840 $Lh^{-1}g_{Ni}^{-1}$ at 850 °C). The activated catalyst showed exceptionally high catalytic activity and excellent stability of DRM reaction in over 300 hours at temperatures that ranged from 700 °C to 850 °C. The

excellent stability of the catalyst resulted from the formation of $NiAl_2O_4$ spinel. The high catalytic activity was due to the high dispersion of Ni nanoparticles deposited by ALD and the reduction of $NiAl_2O_4$ spinel to Ni during the DRM reaction at 850 °C. It was verified that $NiAl_2O_4$ can be reduced to Ni in a reductive gas mixture (i.e., carbon monoxide and hydrogen) during the reaction at 850 °C, but not by H_2 alone.

Keywords: atomic layer deposition (ALD), Ni nanoparticle, supported catalyst, $NiAl_2O_4$ spinel, dry reforming of methane (DRM)

1. INTRODUCTION

Methane reforming with carbon dioxide ($CH_4+CO_2 \rightarrow 2H_2+2CO$), also called dry reforming of methane (DRM), obtained considerable attention due to the advances in shale gas recovery [1, 2]. DRM is important because the two main greenhouse gases (carbon dioxide and methane) could be converted to syngas (carbon monoxide and hydrogen) in this reaction process. The H_2/CO ratio is always lower than 1 due to a reverse water-gas shift reaction ($CO_2+H_2 \rightleftharpoons CO+H_2O$). This gas mixture could be used to blend streams from methane steam reformation to produce syngas with the desired H_2/CO ratio, which could be applied in the Fischer−Tropsch (FT) synthesis [3, 4]. Different metal catalysts (e.g., Rh [5, 6], Pt [7, 8], Ir [9], Pd [10], Ru [11, 12], and Ni [13, 14]) were employed to catalyze the DRM reaction. Among them, noble metal catalysts showed better resistance to coking, as

compared to Ni catalysts [15, 16]. However, due to the limited availability and high cost of noble metals, it was considered desirable to develop a Ni-based catalyst.

The main disadvantage of the Ni catalyst for DRM reaction is deactivation, due to coking and sintering of Ni metal nanoparticles to form larger particles with lower catalytic activity [17]. Coking could be decreased by running the reaction at high temperatures and using small Ni particles, because their step edges are small enough to limit carbon nucleation and growth [4, 18]. However, the aggregation of small Ni nanoparticles will be more extreme at higher reaction temperatures. Therefore, there is a trade-off when Ni nanoparticles are used at higher temperatures. The supported Ni catalysts are normally synthesized by an impregnation method using an aqueous solution of nickel nitrate hexahydrate ($Ni(NO_3)_2 \cdot 6H_2O$) [13, 14, 19-21]. The Ni nanoparticles that are synthesized by the impregnation method are relatively large, typically tens of nanometers [22-24]. They have lower Ni surface areas, compared to smaller Ni nanoparticles, and are easier to get coked.

Atomic layer deposition (ALD) is a self-limiting and self-terminating gas phase deposition technique that has been successfully demonstrated for the synthesis of metal nanoparticles (e.g., Pd and Pt) on different substrates [25, 26]. Small Ni nanoparticles (~3 nm) could be synthesized by ALD and have been demonstrated to be an excellent catalyst with high catalytic activity for catalyzing hydrogenation of propylene [27]. In addition, the ALD Ni nanoparticles strongly interacted with the substrate, which was more stable, when compared to the Ni nanoparticles prepared by conventional methods. Alumina was

demonstrated to be a better catalyst support for the Ni catalyst, as compared to some other catalyst supports (e.g., SiO_2 and $MgO-SiO_2$). This could be due to the fact that the alumina support increased the overall basicity of the supported Ni catalyst and there was a stronger metal-support interaction between the Ni and alumina support [28, 29].

Gould et al. [30] deposited Ni nanoparticles (~3 nm) on dense alumina nanoparticles by ALD to catalyze the DRM reaction and applied porous alumina film obtained from aluminum alkoxide (alucone) molecular layer deposition (MLD) films to stabilize the Ni nanoparticles. The idea was to use ALD to prepare highly dispersed Ni nanoparticles with high catalytic activity and to use porous alumina films to encapsulate the Ni nanoparticles for greater thermal stability. Their results showed that five cycles of alucone MLD could increase the thermal stability and steady-state activity of the catalyst. However, previous studies by Liang et al. indicated that the porous alumina film formed from ten cycles of alucone MLD by calcination could not completely encapsulate 1.8 nm average size Pt particles [31]. Similarly, it would be difficult to use porous alumina films obtained from 5 cycles of alucone MLD coating to encapsulate 3 nm Ni nanoparticles. Therefore, the increase in catalyst stability, with five cycles of MLD coating, should not result from stabilization of Ni particles by alumina film encapsulation. The interaction between the Ni nanoparticles and the deposited alumina film could be the key. In the study by Gould et al., dense alumina nanoparticles were used as catalyst support [30]. We hypothesize that the catalytic performance could be very different if we used porous alumina particles as the catalyst support. There will be more interaction between the Ni nanoparticles and the

porous alumina support (as schematically shown in Fig. S1), since there is more interfacial contact between nanoparticles and the concave surface (porous support), compared to the case of a convex surface (dense particle support). Thus,   the thermal stability of the highly dispersed ALD Ni nanoparticles would be improved. In this study, we synthesized a porous γ-Al_2O_3 supported Ni nanoparticles catalyst using the ALD technique. The DRM reaction was initially carried out at 850 °C, to activate the catalyst, and then run at different temperatures. The reduction mechanism of $NiAl_2O_4$ spinel was studied.

2. EXPERIMENTAL

2.1. Materials. Dense alumina nanoparticles (50-100 nm, gamma phase) and porous γ-Al_2O_3 particles were purchased from Sigma-Aldrich and Alfa Aesar, respectively. The porous alumina particles were 40 μm in diameter, with a Brunauer−Emmett−Teller (BET) surface area of 95.5 m^2/g. The dense alumina nanoparticles had a BET surface area of 137 m^2/g. Bis(cyclopentadienyl)nickel ($NiCp_2$) and $Ni(NO_3)_2 \cdot 6H_2O$ were purchased from Alfa Aesar and Fisher Scientific, respectively.

2.2. Catalyst Preparation and Characterization. Ni nanoparticle ALD was carried out using $NiCp_2$ and hydrogen as precursors at 300 °C in a fluidized bed reactor. The ALD reactor system has been previously described in detail [32]. Both porous γ-Al_2O_3 particles and dense alumina nanoparticles were used as the substrates and one cycle of Ni ALD was applied. These two catalysts were labeled as ALD Ni/γ-Al_2O_3, and ALD Ni/NP-Al_2O_3, respectively. To obtain a better characterization result, a porous γ-Al_2O_3 supported

Ni catalyst with four cycles of Ni ALD (a Ni loading of 4 wt. %) was synthesized and labeled as ALD 4-Ni/γ-Al$_2$O$_3$. For comparison, Ni nanoparticles supported on porous γ-Al$_2$O$_3$ particles were also prepared by the incipient wetness (IW) method. An aqueous solution of Ni(NO$_3$)$_2$·6H$_2$O was added to the porous γ-Al$_2$O$_3$ particles and dried at 110 °C, while stirring continuously. The sample was then calcined in air at 550 °C for 6 hours. The catalyst prepared by the IW method was labeled as IW Ni/γ-Al$_2$O$_3$.

The Ni loadings of different catalysts were measured by inductively coupled plasma-atomic emission spectroscopy (ICP−AES, Model ARL 34101, Thermo Electron, Waltham, MA).

The average size and dispersion of the Ni nanoparticles supported on alumina nanoparticles were observed by transmission electron microscopy (TEM) with a FEI Tecnai F20 TEM.

In order to measure the coke content of the used catalyst, derivative thermogravimetric (DTG) analyses of the samples were made using a TA Instruments Q50 thermogravimetric analyzer. The DTG analyses were carried out with an air (40 mL/min) and N$_2$ (40 mL/min) stream. The temperature was increased from room temperature to 200 °C, at a heating rate of 10 °C/min, and kept at 200 °C for 60 min, and then increased to 1000 °C at the same rate.

X-Ray diffraction (XRD) spectra were recorded on a Philips X-Pert Multi-purpose Diffractometer, using Cu Kα 1 radiation (λ=0.15416 nm).

X-ray photoelectron spectroscopy (XPS) measurements were performed using a Kratos Axis 165 X-ray photoelectron spectrometer with a monochromatic Al Kα radiation (hν = 1486.6 eV). All binding energy values were corrected based on a C (1s) peak at 284.5 eV.

H$_2$-temperature programmed reduction (TPR) tests were performed using an AMI-300. Typically, 100 mg of the sample were charged in a quartz tube and reduced up to 900 °C at a heating rate of 10 °C/min in a stream of 10% H$_2$ in Ar. The ALD Ni/γ-Al$_2$O$_3$ and ALD Ni/NP-Al$_2$O$_3$ samples were oxidized at 550 °C for 1 hour before the TPR test.

2.3. General Procedure for Dry Reforming of Methane. Different amounts of various catalysts were loaded into a quartz tube reactor (10 mm diameter) to keep the Ni content consistent (~0.64 mg). Quartz wool was employed to support the catalysts. The catalysts, using porous γ-Al$_2$O$_3$ as supports, were diluted with 0.5 gram of quartz sands (60-120 mesh) and were well distributed in the quartz sands. A thermal couple was applied to measure the temperature. The ALD synthesized catalysts were oxidized at 550 °C to remove any residual organic components from the Ni ALD precursor. All of the catalysts were reduced with 20% H$_2$ and 80% Ar (with a total flow rate of 100 sccm) at 700 °C for 1 hour before the DRM reaction. CH$_4$ and CO$_2$ that were balanced with Ar (20% CH$_4$, 20% CO$_2$, and 60% Ar, with a total flow rate of 100 sccm), were introduced into the reactor at different temperatures for a DRM reaction. The catalysts were regenerated after the reaction and applied to catalyze the DRM reaction again. In a typical regeneration process, the catalyst was first oxidized in 20% O$_2$ and 80% Ar at 700 °C for 1 hour and then reduced

in 20% H_2 and 80% Ar at the same temperature for 1 hour. The gas flow rates were controlled by MKS® mass flow controllers. The reaction products were analyzed by an online gas chromatograph (SRI 8610C) equipped with a 6-foot HAYESEP D column, a 6-foot MOLECULAR SIEVE 13X column, and a thermal conductivity detector (TCD).

3. RESULTS AND DISCUSSION

3.1. Catalytic Performance The ALD Ni/γ-Al_2O_3 catalyst was first employed to catalyze the DRM. Fig. 1 shows the DRM reaction results at different temperatures as catalyzed by ALD Ni/γ-Al_2O_3. In the first cycle (here, one cycle means testing at different temperatures without regeneration), the reaction was carried out at 700 °C, but no conversion was observed. The temperature of the DRM reaction was then increased to 850 °C, while the methane conversion kept increasing during the first 10 hours, and then stabilized at ~93%. This increase could have been due to the activation of the catalyst. After running at 850 °C for 75 hours, the catalyst was regenerated at 700 °C. In the second cycle, the methane conversion was 99% at 850 °C, and did not decrease in 140 hours. This excellent stability could have been due to the fact that the sintering of Ni nanoparticles would be inhibited by the porous structure of the catalyst support and the strong interaction between the Ni nanoparticles and the catalyst support. When the reaction temperature was decreased to 800 °C, the methane conversion decreased to 95%, but only slightly decreased to 93% after 50 hours of reaction. The methane conversion decreased to 72%, after the reaction temperature had decreased to 750 °C, and slightly decreased with an increase in

the reaction time (70% after about 50 hours). The reaction temperature then decreased further to 700 °C, while the methane conversion decreased to 40%, and then decreased slightly to 38% after about 50 hours of reaction. Table 1 shows the methane reforming rate in the DRM reaction, for the second cycle of DRM reaction, which was calculated from the methane conversion (shown in Fig. 1), gas flow rate, and catalyst loading. The methane reforming rate at 850 °C in the second cycle was as high as 1840 $Lh^{-1}g_{Ni}^{-1}$. This value could have been underestimated, since the methane conversion was pretty close to 100%. The third cycle showed results similar to those of the second cycle. This series of experiments, showed that the decreases in methane conversion at each temperature level should not have been due to the sintering. Otherwise, the performance of the catalyst in the third cycle would have been worse than that in the second cycle. It is believed that this decrease resulted from a slight coking on the catalyst. The catalyst color changed to black after the reaction due to coking (Fig. S2).

In previously reported studies of DRM, a reaction was normally carried out in a temperature range of 700 °C to 800 °C [19, 20, 30, 33-35]. Only a few reports studied DRM reactions at 850 °C, since Ni nanoparticles would aggregate to form larger particles at those high temperatures. In this study, it was found that it was beneficial to run the DRM reaction at 850 °C, since the ALD Ni/γ-Al$_2$O$_3$ catalyst can be activated at that high temperature. In Table 1, the activity of the ALD Ni/γ-Al$_2$O$_3$ catalyst was compared with some other Ni/Al$_2$O$_3$ catalysts synthesized by other groups. Wang et al. [36] synthesized a gamma-alumina supported Ni catalyst by a wetness impregnation method and showed methane

reforming rates of 137 $Lh^{-1}g_{Ni}^{-1}$ and 157 $Lh^{-1}g_{Ni}^{-1}$ at 700°C and 800°C, respectively. The porous alumina coated Ni nanoparticles, supported on dense alumina nanoparticles synthesized by Gould et al., gave a methane reforming rate of 700 $Lh^{-1}g_{Ni}^{-1}$ at 700 °C [30]. Baktash et al. [35] synthesized an inverse catalyst with Ni nanoparticles encapsulated with alumina that gave a maximum methane reforming rate of 1500 $Lh^{-1}g_{Ni}^{-1}$ at 800 °C. In our study, the ALD Ni/γ-Al$_2$O$_3$ catalyst showed methane reforming rates of 1840 $Lh^{-1}g_{Ni}^{-1}$ at 850 °C, 1740 $Lh^{-1}g_{Ni}^{-1}$ at 800 °C, and 720 $Lh^{-1}g_{Ni}^{-1}$ at 700 °C even after several hundreds of hours of reaction at high temperatures, which was still higher than the value reported by Gould et al. [30]. Clearly, the porous alumina supported ALD Ni nanoparticles showed much better activity, as compared to other catalysts reported previously.

Table 1. Catalytic activities comparison of different Ni/Al$_2$O$_3$ catalysts in DRM reaction.

Catalyst	Methane reforming rate ($Lh^{-1}g_{Ni}^{-1}$)				References
	850 °C	800 °C	750 °C	700 °C	
ALD Ni/γ-Al$_2$O$_3$	1840	1740	1320	720[a]	This work
Ni/γ-Al$_2$O$_3$	N/A	157	N/A	137	[36]
Inverse Ni/Al$_2$O$_3$ catalyst	N/A	1500	N/A	N/A	[35]
ALD Ni/dense γ-Al$_2$O$_3$	N/A	N/A	N/A	700	[30]

[a] The results were tested after about 250 hours of reaction at high temperatures.

To verify that ALD is a better way to prepare supported Ni nanoparticles catalysts, as compared to the traditional impregnation method, an IW Ni/γ-Al$_2$O$_3$ catalyst was employed to catalyze the DRM reactions (results shown in Fig. 2). The corresponding methane reforming rates of the second cycle of the DRM reaction are shown in Table 2. The reaction was first carried out at 850 °C. The catalyst was activated at the beginning of the reaction, and then, the methane conversion was kept at about 90%. Between each cycle, the catalyst was regenerated by following the same procedures that are mentioned above. In the second cycle, the methane conversion was decreased from 94% to 88% in 48 hours at 850 °C. The methane conversion decreased to 69% after the reaction temperature decreased to 800 °C, and decreased further to 56% in 48 hours. The conversions of methane were lower than 30% and 10% at 750 °C and 700 °C, respectively. This catalyst showed lower stability and much lower activity, as compared to the ALD Ni/γ-Al$_2$O$_3$. In the third cycle, the performance of the catalyst was much worse. The lower catalytic activity and stability of the IW Ni/γ-Al$_2$O$_3$ catalyst could have been caused by two things: (1) the Ni nanoparticles synthesized by the IW method were much larger than the ALD-deposited Ni nanoparticles, which would have had lower catalytic activity due to a lower reactive surface area, and coking formation was easier; and (2) the bonding force between the Ni nanoparticles and the catalyst support for the IW Ni/γ-Al$_2$O$_3$ catalyst could have been weaker than that of the ALD Ni/γ-Al$_2$O$_3$ catalyst, since the Ni nanoparticles strongly interacted with the substrate in the ALD process.

Fig.1. Methane conversion of dry reforming of methane catalyzed by ALD Ni/γ-Al$_2$O$_3$ at different temperatures.

Table 2. Rate of dry reforming of methane and H$_2$/CO ratio catalyzed by three different catalysts at different temperatures.

Catalyst	CH$_4$ reforming rate (L·h^{-1}g$_{Ni}$$^{-1}$)				H$_2$/CO ratio in the product			
	850 °C	800 °C	750 °C	700 °C	850 °C	800 °C	750 °C	700 °C
ALD Ni/γ-Al$_2$O$_3$	1840	1740	1320	720	0.82	0.78	0.68	0.55
IW Ni/γ-Al$_2$O$_3$	1700	1150	480	150	0.70	0.61	0.51	0.38
ALD Ni/NP-Al$_2$O$_3$	1380	850	410	190 (706)[a]	0.74	0.73	0.71	0.65

Note: The results in this table were calculated based on the second cycle of DRM reaction for all three catalysts.

[a] The value in brackets was calculated based on the result of DRM reaction carried out at 700 °C directly after reduction without running at higher temperatures.

To check the effect of porous catalyst support on the DRM reaction, the ALD Ni/NP-Al$_2$O$_3$ sample was also used to catalyze the DRM reaction. As shown in Fig. 3, the

dense substrate supported catalyst showed high catalytic activity at the beginning, but no gradual increase of conversion when the reaction was carried out at 850 °C. This means that the catalysts can be activated very easily. Thus, it is reasonable to hypothesize that there was a much stronger interaction between the Ni nanoparticles and the porous γ-Al$_2$O$_3$ support for ALD Ni/γ-Al$_2$O$_3$ catalyst, as compared to the ALD Ni/NP-Al$_2$O$_3$ catalyst. After 60 hours of reaction at 850 °C, the methane conversion decreased from 89% to 73%. The methane conversion decreased to 52% after the reaction temperature decreased to 800 °C and further decreased with an increase in the reaction time (from 52% to 45% after 50 hours). When the reaction temperature decreased to 750 °C, the methane conversion decreased to 28%, and decreased further to 22% in 50 hours. The reaction temperature was then decreased to 700 °C, and the methane conversion decreased to 11%, and decreased further to 9% in only 5 hours. It is believed that the decreases in catalytic activity at each temperature resulted from both the sintering of Ni nanoparticles and coking on the catalyst. Clearly, the activity and stability of ALD Ni/NP-Al$_2$O$_3$ were much lower than those of the ALD Ni/γ-Al$_2$O$_3$ catalyst, indicating that porous γ-Al$_2$O$_3$ (as compared to dense alumina nanoparticles support) was a better support for the Ni catalyst in the DRM reaction. Between each cycle, the catalyst was regenerated following the same procedures mentioned above. In the second and third cycles, the methane conversion increased at the beginning of each reaction, indicating that activation was needed for the catalyst after regeneration. The catalyst showed similar results, as compared to the first cycle. The decreases in catalytic activity at each temperature resulted from the coking of the catalyst.

The reasons why the catalyst was activated at the beginning of the second and third cycles will be discussed in a later section. The average size of Ni nanoparticles increased from 3 nm to ~37 nm after three cycles of the DRM reactions (Fig. S3). As shown in the TEM image, the alumina nanoparticle supports were sintered to form a larger particle support. The dependence of catalyst coking and Ni nanoparticles sintering on the reaction temperature was also verified (Fig. S4). The sintering of Ni nanoparticles was more severe at 850 °C, as comparted to 700 °C, but coking happened under both temperatures. The DTG results (Fig. S5 and Fig. S6) showed no obvious coke content on the catalyst due to the low content of coke. Carbon nanotubes were observed on the catalyst used at 850 °C (Fig. S7). The corresponding methane reforming rates of the second cycle of the DRM reaction are shown in Table 2. In each cycle, the methane reforming rate at 700 °C was about 190 $Lh^{-1}g_{Ni}^{-1}$, which was lower than the result of about 700 $Lh^{-1}g_{Ni}^{-1}$ reported by Gould et al. [30]. The reason for the lower catalytic activity was believed to be the sintering of Ni nanoparticles in a series of reactions at much higher temperatures, before the reaction at 700 °C. To verify this, another reaction was carried out (directly after the reduction at 700 °C without running at higher temperatures) employing ALD Ni/NP-Al_2O_3 as the catalyst at 700 °C. The result was similar to Gould's result (Fig. S8), and the methane reforming rate was also similar to Gould's result (Table 2).
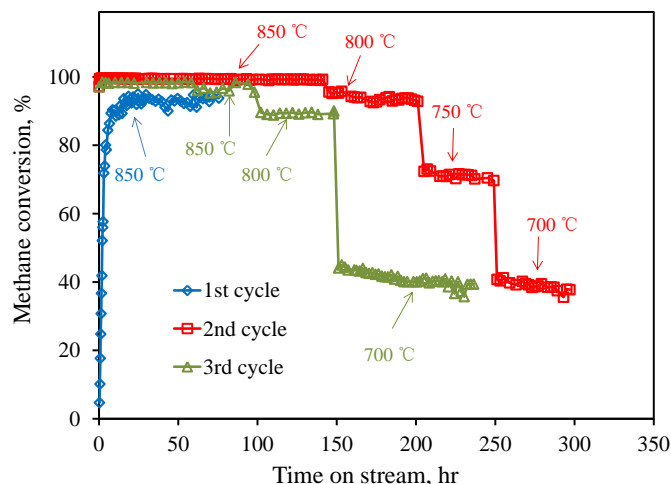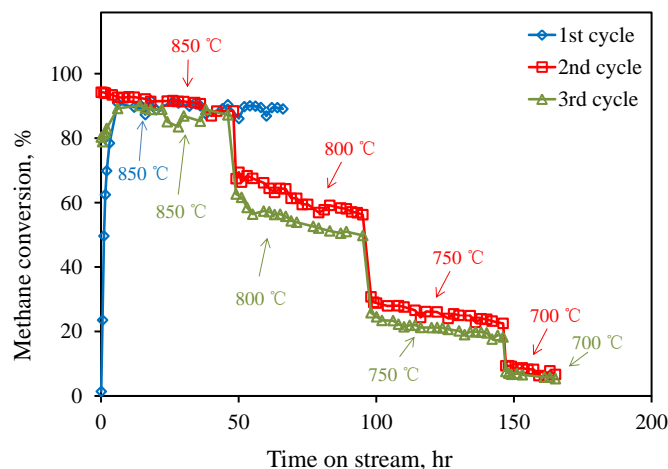
Fig. 2. Methane conversion of dry reforming of methane catalyzed by IW Ni/γ-Al₂O₃ at different temperatures.

Based on this series of experiments, it was clear that the ALD Ni nanoparticles were much more active than the Ni nanoparticles synthesized by the IW method. Also, the porous γ-Al₂O₃ supported ALD Ni nanoparticle catalyst showed higher activity and greater stability, as compared to the dense alumina supported ALD Ni nanoparticle catalyst. The higher activity of the porous γ-Al₂O₃ supported catalyst could have been due to a larger number of Ni-Al₂O₃ interfacial sites formed between the Ni nanoparticles deposited inside the cavities of the porous alumina support, as compared to those of the dense alumina supported catalyst. The greater stability could have been due to the porous structure of the support, which could limit the sintering of the Ni nanoparticles and, thus, inhibit coking during the reaction. Another reason for the greater stability could have been the stronger Ni-support interaction formed by depositing Ni nanoparticles on the porous support, as compared to that of the dense substrates. Similar phenomena have also been reported. Gao

et al. [37] found that the Ni nanoparticles deposited inside the cavities of the Al_2O_3

nanotubes could form more $Ni-Al_2O_3$ interfacial sites and stronger $Ni-Al_2O_3$ interactions,

which showed higher catalytic activity and greater stability in catalyzing hydrogenation of

cinnamaldehyde, as compared to that of the Ni nanoparticles deposited on the outside wall

of the Al_2O_3 nanotubes by ALD. The increase in the catalytic activity of the ALD Ni/γ-

Al_2O_3 catalyst at the beginning of the DRM reaction at 850 °C indicated that an activation

period was needed to reduce the Ni catalyst from NiO or $NiAl_2O_4$ to Ni. This indicated that

the catalysts can be activated at a high temperature first, and then high catalytic activity

can be achieved at a lower reaction temperature (e.g., 700 °C).

The ALD Ni/γ-Al_2O_3 catalyst was first activated by running the DRM reaction at

850 °C for 10 hours, and then the reaction temperature was directly decreased to 700 °C

(Fig. 4). The catalyst showed activity in catalyzing the DRM reaction. In contrast, no

conversion was observed for the same catalyst (after the standard reduction process) when

directly employed to catalyze the DRM reaction at 700 °C. This means that the ALD Ni/γ-

Al_2O_3 catalyst can be activated by the DRM reaction at 850 °C. Between each cycle, the

catalyst was regenerated. In the second and third cycles, the methane conversions increased

at the beginning of the reaction, which indicated that the catalyst had not been fully

activated in the previous cycles of reactions. In the third cycle, the catalyst took a shorter

time to recover, as compared to recovery in the second cycle. This could have been due to

the fact that the catalyst was further activated in the second cycle. Compared to the results

of the first batch of the catalyst (Fig. 1), the initial activity at 700 °C in the third cycle of

the catalyst was higher, but the conversion decreased more quickly with increased reaction time. The reason for the decrease in conversion should not have been the sintering of Ni nanoparticles, since the methane conversion at 700 °C did not decrease much during the first two cycles. This decrease would have been due to the fact that the catalyst was not fully activated. These results supported our hypothesis that catalysts can be activated at a high temperature, and high catalytic activity can be achieved at a lower reaction temperature.
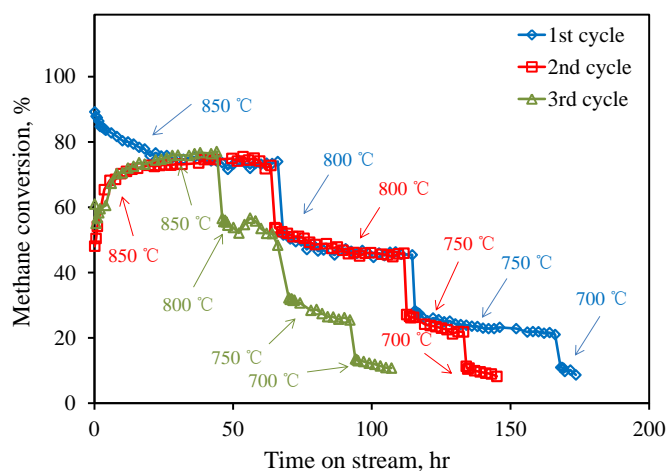
Fig. 3. Methane conversion of dry reforming of methane catalyzed by ALD Ni/NP-Al$_2$O$_3$ at different temperatures.
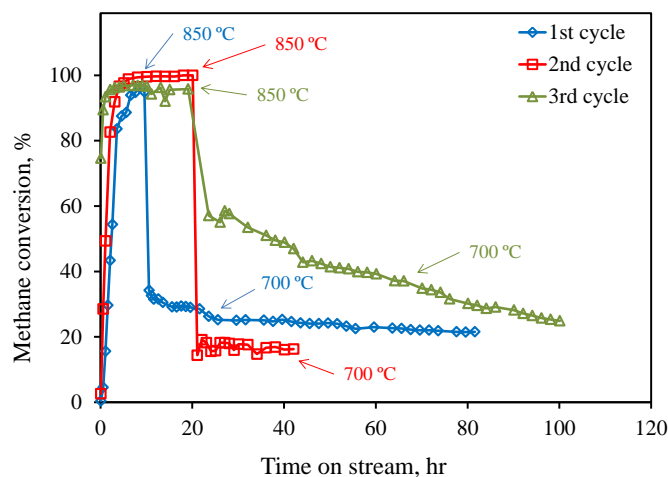
Fig. 4. Methane conversion of dry reforming of methane catalyzed by ALD Ni/γ-Al₂O₃ at 700 °C and 850 °C.

Chen et al. [38] previously reported that alumina supported Ni catalyst (calcined at 750 °C) showed low activity at the beginning of a reaction carried out at 750 °C, but the activity increased with increased reaction time. They claimed that the increase in activity was due to the reduction of NiAl$_2$O$_4$ spinel by hydrogen produced from the DRM reaction. However, from their H$_2$-TPR results, NiAl$_2$O$_4$ spinel can hardly be reduced by hydrogen at 750 °C. Thus, the mechanism of catalyst activation should not be the reduction of NiAl$_2$O$_4$ spinel by hydrogen alone. To verify this, the ALD Ni/γ-Al$_2$O$_3$ catalyst was reduced in 20% H$_2$ and 80% Ar (with a total flow rate of 100 sccm) at 850 °C for 10 hours. It was reported that NiO could be easily reduced under these reduction conditions [13]. The reduced catalyst was applied to catalyze a DRM reaction at 700 °C; however, no conversion was observed at 700 °C. This indicated that hydrogen could not reduce/activate the catalyst at 850 °C, and the amount of reduced Ni and NiO in this catalyst was very small. Thus, the

Ni content should be mainly $NiAl_2O_4$ spinel. The existence of $NiAl_2O_4$ spinel has been verified by XPS and H_2-TPR in a later section. However, in the DRM reaction, the methane conversion reached 90% after reaction at 850 °C for 10 hours. This indicated that catalysts can be activated more easily in a mixed gas atmosphere of reaction products (e.g., H_2 and CO), since the DRM product at 850 °C was mainly H_2 and CO.

To investigate and determine the role of gases in catalyst activation, a catalyst was reduced in different gases and then employed for a DRM reaction. First, one batch of a fresh catalyst was reduced in 16% H_2, 20% CO (H_2/CO ratio was similar to the gas mixture of H_2 and CO in the product of DRM at 850 °C) and 64% Ar (with 100 sccm of total flow rate) at 850 °C for 10 hours. The catalyst was employed to catalyze the DRM reaction at 700 °C. The initial conversion was 22%, but decreased quickly to 7% in 4 hours (Fig. S9). This indicated that the mixture of H_2 and CO was a better activator than H_2 alone. After 4 hours of reaction at 700 °C, the reaction temperature was increased to 850 °C, and the conversion increased to 94% after about 30 hours. The methane conversion at 700 °C, which was lower than that shown in the first batch (Fig. 1), kept decreasing. This could have been due to the fact that 10 hours may not have been long enough for the reduction of the catalyst, or because the amounts of H_2 and CO introduced were not enough for the reduction process, or both. After the catalyst was regenerated, it was applied for use in the DRM reaction at 700 °C. The methane conversion was higher than that in the first cycle, indicating that the catalyst had been further activated during the first cycle of reaction at 850 °C. The fresh catalyst was also reduced in methane and the reduced catalyst showed

activity in catalyzing a DRM reaction (Fig. S10). However, the methane conversion was very low (lower than 2%), indicating that the methane was also a reducing agent of the catalyst, but it was not as good as the mixture of hydrogen and carbon monoxide. It has been demonstrated that the $NiAl_2O_4$ spinel can be reduced by the carbon formed on the surface at a relative high temperature in a chemical-looping combustion reaction [39]. In this study, it is possible that the reduction of $NiAl_2O_4$ spinel in the mixed gases atmosphere of the reaction could have been partly the result of the carbon that formed on the catalyst surface from a Boudouard reaction ($2CO \rightleftharpoons CO_2+C$) and a methane decomposition reaction ($CH_4 \rightarrow 2H_2+C$).

3.2. Catalysts Characterization. ICP-AES results showed that the Ni loadings of ALD Ni/γ-Al_2O_3 and ALD Ni/NP-Al_2O_3 catalysts were both 0.97 wt. %. The Ni loading of the IW Ni/γ-Al_2O_3 sample was 1.15 wt. %. Fig. 5 shows the TEM image of the ALD Ni/NP-Al_2O_3 sample and the size distribution of Ni nanoparticles (inset image). The average Ni nanoparticle size was 3.6 nm, which was similar to the value reported by Gould et al. [30]. Clearly, the Ni nanoparticles were distributed uniformly on the alumina nanoparticle substrate. It is reasonable to expect that the average size of Ni nanoparticles deposited by ALD on porous γ-Al_2O_3 substrate would also be about 3.6 nm. In contrast, the size of Ni particles prepared by the IW method were normally much larger, typically by tens of nanometers [22-24].
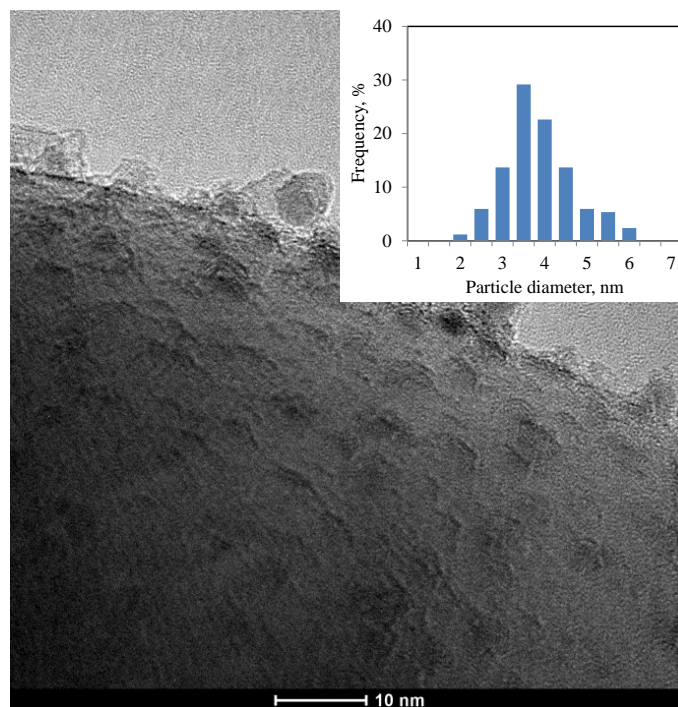
Fig. 5. TEM image of an ALD Ni/NP-Al$_2$O$_3$ catalyst. The inset image shows the size distribution of Ni nanoparticles.

To further verify the effect of the activation of a catalyst on DRM reaction activity, we investigated the Ni redox status of the catalyst before and after reduction. The ALD 4-Ni/γ-Al$_2$O$_3$ sample was first oxidized in air at 550 °C for 1 hour, and then reduced at 850 °C in 45% H$_2$ and 55% CO (with a total flow rate of 100 sccm) for 20 hours and 120 hours, respectively. XPS and XRD tests were applied to these four as-deposited, oxidized and reduced samples. Fig. 6 shows high resolution Ni (2p) XPS spectra of the ALD 4-Ni/γ-Al$_2$O$_3$ catalyst before and after being heated at 550 °C for 1 hour. Metallic Ni was observed in the as-deposited ALD 4-Ni/γ-Al$_2$O$_3$ at 852.8 eV and 853.5 eV [40, 41]. The NiAl$_2$O$_4$ spinel was observed at 856.2 eV [42, 43], and the peak at 861.5 eV represented NiO [44].

The formation of the $NiAl_2O_4$ increased the interaction between Ni nanoparticles and the γ-Al_2O_3 support. The strong interaction between Ni and alumina support improved the dispersion of Ni and retarded the sintering of Ni nanoparticles [38, 45]. This was the reason for the high activity and thermal stability of ALD Ni/γ-Al_2O_3. For the oxidized sample, the metallic Ni could not be observed, while the peaks of NiO and $NiAl_2O_4$ became stronger. This indicated that the metallic Ni oxidized to NiO and $NiAl_2O_4$ during the oxidation process. Compared to the as-deposited sample, the carbon peak of the oxidized sample was weaker, indicating the removal of the residual organic component from the Ni ALD process (Fig. S11). After the oxidized sample was reduced in a mixture of H_2 and CO for 120 hours, the Ni signal could not be detected by XPS. This was due to the fact that the Ni nanoparticles were coated by carbon formed from the Boudouard reaction. This was also verified by high resolution C (1s) XPS analysis (Fig. S11), since the carbon peak was significantly stronger after reduction. Metallic Ni could be observed by XRD in both reduced samples (Fig. S12). Based on the XPS and XRD results, it was verified that the $NiAl_2O_4$ spinel was formed during the ALD process and the spinel could be reduced in a mixture of CO and H_2 at 850 °C.

The samples were also analyzed by H_2-TPR. The ALD Ni/γ-Al_2O_3 and ALD Ni/NP-Al_2O_3 samples were oxidized at 550 °C for 1 hour before the TPR test. As shown in Fig. 7, the H_2-TPR result of the ALD Ni/γ-Al_2O_3 sample analysis showed hydrogen consumption at four temperatures. The peak at 280 °C was attributed to free NiO, since the reduction temperature of a commercial NiO was reported to about 300 °C [46]. The peak

at 570 °C represented the reduction of NiO that interacted with the support. Previous studies had indicated that the reduction peak of NiO that interacted with the support appeared to be within a range of 500-700 °C [47]. Generally, the reduction peak of stoichiometric $NiAl_2O_4$ spinel should be higher than 800 °C; therefore, a peak at 780 °C in this study could be due to the reduction of non-stoichiometric nickel aluminate [46, 48]. The hydrogen consumption near 900 °C was due to reduction of the stoichiometric $NiAl_2O_4$ spinel, and the peak kept increasing until 900 °C. However, due to limitations of the instrument, a higher temperature H_2-TPR test could not be processed. Therefore, the amount of the $NiAl_2O_4$ could not be determined by a H_2-TPR test. As we know, NiO can be reduced at 700 °C, so, it was reasonable to expect that all NiO in the ALD Ni/γ-Al_2O_3 could be reduced at 700 °C. However, the catalyst that reduced at 700 °C showed no activity in catalyzing a DRM reaction at 700 °C, as we discussed earlier. Therefore, the amount of NiO in the catalyst should have been very small and the majority of Ni in the ALD Ni/γ-Al_2O_3 catalyst should have been in the format of $NiAl_2O_4$. Thus, we concluded that the activation of the ALD Ni/γ-Al_2O_3 catalyst was due to the reduction of $NiAl_2O_4$ spinel to metallic Ni in the mixed gases atmosphere of the DRM reaction. Some $NiAl_2O_4$ spinel may have formed again during the regeneration process, since the $NiAl_2O_4$ spinel could form by calcining the catalyst at 600 °C in the presence of O_2 [49]. This could be the reason why the methane conversion increased at the beginnings of the second and third cycles of the DRM reactions catalyzed by ALD Ni/NP-Al_2O_3.
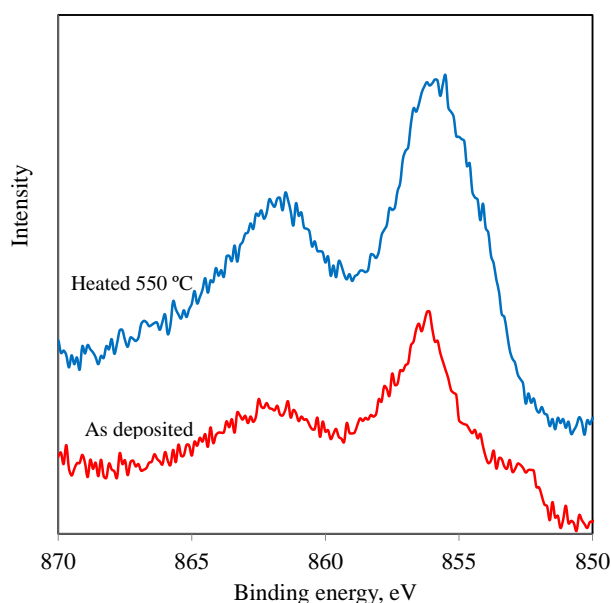
Fig. 6. High resolution XPS spectra of nickel (2p) of the as-deposited ALD 4-Ni/γ-Al$_2$O$_3$ sample, and the sample oxidized at 550 °C for 1 hour.

H$_2$-TPR tests were also employed for the IW Ni/γ-Al$_2$O$_3$ and ALD Ni/NP-Al$_2$O$_3$ samples. As shown in Fig. 7, for the ALD Ni/NP-Al$_2$O$_3$ sample, the peak at 280 °C was attributed to the reduction of free NiO. The peak for the reduction of NiO that interacted with the support at 500 °C was lower than that for the ALD Ni/γ-Al$_2$O$_3$ catalyst (570 °C). This have been due to the different morphology of the substrates. There would be more interaction between the Ni nanoparticles and the porous alumina support (concave surface), compared to the case of dense alumina particle support (convex surface). The reduction of NiAl$_2$O$_4$ spinel can be observed at 860 °C. This temperature was also lower than that of the ALD Ni/γ-Al$_2$O$_3$ catalyst, which indicated weaker interaction between Ni nanoparticles and the catalyst support. The ALD Ni/NP-Al$_2$O$_3$ catalyst showed an activity decrease

during the reaction, which was due to the fact that NiO could be easily reduced to metallic

Ni during the reduction process, and the Ni nanoparticles were easier to get sintered, as

compared to the catalysts supported on a porous substrate.
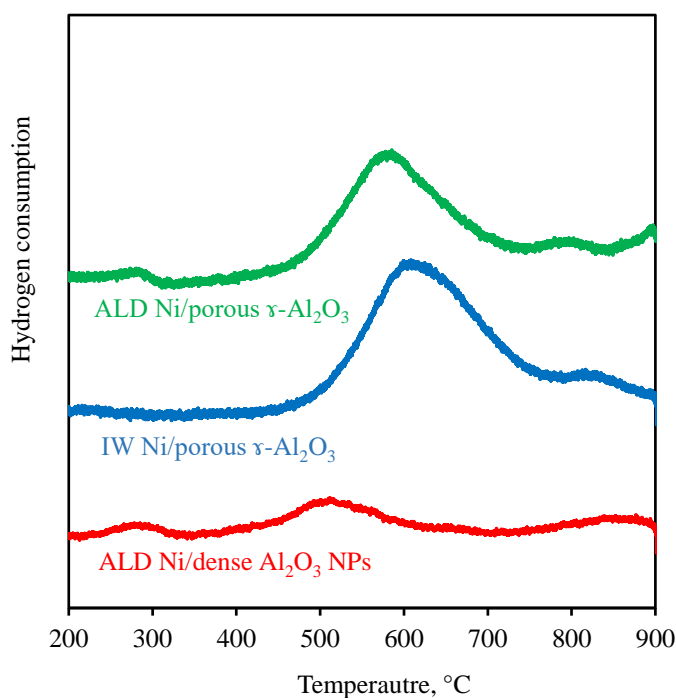
Fig. 7. H$_2$-TPR results of ALD Ni/γ-Al$_2$O$_3$, IW Ni/γ-Al$_2$O$_3$, and ALD Ni/NP-Al$_2$O$_3$ catalysts.

For the IW Ni/γ-Al$_2$O$_3$ sample, no peak for free NiO was observed. This was

different from what was observed for the ALD prepared catalysts. This could be due to the

fact that the Ni nanoparticles synthesis methods were different. Their peaks at 600 °C and

810 °C were attributed to the reduction of NiO that interacted with the support and NiAl$_2$O$_4$

spinel, respectively. The lower reduction temperature of $NiAl_2O_4$ spinel indicated the weaker interaction between the Ni nanoparticles and the catalyst support as compared to the ALD $Ni/\gamma-Al_2O_3$ catalyst. The amount of the $NiAl_2O_4$ spinel was not much, as compared to NiO. During the catalytic reactions, it was found that the catalyst still needed a short activation period. This could have been due to the existence of $NiAl_2O_4$ spinel, which was not reduced during the reduction process at 700 °C, but it could have been reduced during the DRM reaction.

Ni in the format of $NiAl_2O_4$ is not as reactive as metallic Ni for a DRM reaction [38]. In most of the previously reported studies, the Ni/Al_2O_3 catalysts were reduced in H_2 at a relatively low temperature [35, 36, 38]. There was a high possibility that only NiO was reduced, but not the $NiAl_2O_4$ spinel. In the study of Gould et al. [30], the catalyst coated with five cycles of alucone MLD showed a higher steady-state methane reforming rate and better stability, as compared to the uncoated catalyst. More $Ni-Al_2O_3$ interfacial sites could be formed after the deposition of porous alumina films on the alumina nanoparticles supported the Ni catalyst and, thus, increased the interaction of Ni and alumina. This could be the reason why the coated catalyst prepared by Gould et al. showed higher steady-state activity. Even though it is well known that alumina is a better support for the Ni catalyst in high temperature DRM applications, due to the fact that the formation of $NiAl_2O_4$ could help improve the dispersion of Ni and retard the sintering of Ni nanoparticles, no report investigated the activation mechanism of the catalyst in the DRM reaction. Our study

further verified that the activation/reduction of the Ni catalyst was very important for catalytic activity.

4. CONCLUSION

Ni nanoparticles were loaded on both dense alumina nanoparticles and porous alumina substrates. The ALD synthesized porous γ-Al_2O_3 supported Ni nanocatalyst showed both high activity and stability in the DRM reaction. The porous alumina substrate was demonstrated to be a better support for the DRM reaction, as compared to the dense alumina nanoparticles in terms of activity and stability. $NiAl_2O_4$ spinel was formed after Ni nanoparticles were deposited on the porous γ-Al_2O_3 by ALD. $NiAl_2O_4$ spinel could be reduced to metallic Ni in the DRM reaction process by CO and H_2 in the product of the DRM reaction, which could greatly increase catalyst activity. Methane, or the mixture of H_2 and CO, can reduce $NiAl_2O_4$ to Ni at 850 °C, but hydrogen alone cannot. This study indicates that it is feasible to deposit highly dispersed and stable Ni nanoparticles on a porous γ-Al_2O_3 support and then reduce the catalyst with a mixture of H_2 and CO to produce a highly stable and active catalyst for the DRM reaction.

REFERENCES

1.   J. Baltrusaitis, W.L. Luyben, ACS Sustain. Chem. Eng. 3 (2015) 2100-2111.

2.   A.R.S. Darujati, W.J. Thomson, Chem. Eng. Sci. 61 (2006) 4309-4315.

3.   D.A. Wood, C. Nwaoha, B.F. Towler, J. Nat. Gas Sci. Eng. 9 (2012) 196-208.

4.   J.R. Rostrup-Nielsen, J. Sehested, J.K. Norskov, Adv. Catal. 47 (2002) 65-139.

5.   H.Y. Wang, E. Ruckenstein, Appl. Catal. A: Gen. 204 (2000) 143-152.

6.   R. Wang, H.Y. Xu, X.B. Liu, Q.J. Ge, W.Z. Li, Appl. Catal. A: Gen. 305 (2006) 204-210.

7.   A.M. O'Connor, Y. Schuurman, J.R.H. Ross, C. Mirodatos, Catal. Today 115 (2006) 191-198.

8.   S. Damyanova, B. Pawelec, K. Arishtirova, M.V.M. Huerta, J.L.G. Fierro, Appl. Catal. B: Environ. 89 (2009) 149-159.

9.   M. Wisniewski, A. Boreave, P. Gelin, Catal. Commun. 6 (2005) 596-600.

10.   P.G. Schulz, M.G. Gonzalez, C.E. Quincoces, C.E. Gigola, Ind. Eng. Chem. Res. 44 (2005) 9020-9029.

11.   C. Carrara, J. Munera, E.A. Lombardo, L.M. Cornaglia, Top. Catal. 51 (2008) 98-106.

12.   J.X. Chen, C.C. Yao, Y.Q. Zhao, P.H. Jia, Int. J. Hydrogen Energy 35 (2010) 1630-1642.

13.   M.M. Barroso-Quiroga, A.E. Castro-Luna, Int. J. Hydrogen Energy 35 (2010) 6052-6056.

14.   S. Therdthianwong, A. Therdthianwong, C. Siangchin, S. Yongprapat, Int. J. Hydrogen Energy 33 (2008) 991-999.

15.   J.R. Rostrupnielsen, J.H.B. Hansen, J. Catal. 144 (1993) 38-49.

16.   Z.Y. Hou, P. Chen, H.L. Fang, X.M. Zheng, T. Yashima, Int. J. Hydrogen Energy, 31 (2006) 555-561.

17.   F. Pompeo, N.N. Nichio, M.G. González, M. Montes, Catal. Today 107-08 (2005) 856-862.

18.   H.S. Bengaard, J.K. Norskov, J. Sehested, B.S. Clausen, L.P. Nielsen, A.M. Molenbroek, J.R. Rostrup-Nielsen, J. Catal. 209 (2002) 365-384.

19.   A. Kambolis, H. Matralis, A. Trovarelli, C. Papadopoulou, Appl. Catal. A: Gen. 377 (2010) 16-26.

20.   B.Q. Xu, J.M. Wei, H.Y. Wang, K.Q. Sun, Q.M. Zhu, Catal. Today 68 (2001) 217-225.

21.   C. Courson, E. Makaga, C. Petit, A. Kiennemann, Catal. Today 63 (2000) 427-437.

22.   T. Sekino, T. Nakajima, S. Ueda, K. Niihara, J. Am. Ceram. Soc. 80 (1997) 1139-1148.

23.   D.J. Lensveld, J.G. Mesu, A.J. van Dillen, K.P. de Jong, Microporous Mesoporous Mater. 44 (2001) 401-407.

24.   P. Azadi, R. Farnood, E. Meier, J. Phys. Chem. A 114 (2010) 3962-3968.

25.   X.H. Liang, L.B. Lyon, Y.-B. Jiang, A.W. Weimer, J. Nanopart. Res. 14 (2012) article No. 943.

26.   X.H. Liang, Y. Zhou, J.H. Li, A.W. Weimer, J. Nanopart. Res. 13 (2011) 3781-3788.

27.   T.D. Gould, A.M. Lubers, B.T. Neltner, J.V. Carrier, A.W. Weimer, J.L. Falconer, J.W. Medlin, J. Catal. 303 (2013) 9-15.

28.   A. Takano, T. Tagawa, S. Goto, J. Chem. Eng. Jpn. 27 (1994) 727-731.

29.   F. Frusteri, G. Italiano, C. Espro, F. Arena, Catal. Today 171 (2011) 60-66.

30. T.D. Gould, A. Izar, A.W. Weimer, J.L. Falconer, J.W. Medlin, ACS Catal. 4 (2014) 2714-2717.

31. X.H. Liang, J.H. Li, M. Yu, C.N. McMurray, J.L. Falconer, A.W. Weimer, ACS Catal. 1 (2011) 1162-1165.

32. X.H. Liang, L.F. Hakim, G.-D. Zhan, J.A. McCormick, S.M. George, A.W. Weimer, J.A. Spencer II, K.J. Buechler, J. Blackson, C.J. Wood, J. Am. Ceram. Soc. 90 (2007) 57-63.

33. J.M. Wei, B.Q. Xu, J.L. Li, Z.X. Cheng, Q.M. Zhu, Appl. Catal. A: Gen. 196 (2000) L167-L172.

34. Z.W. Li, L.Y. Mo, Y. Kathiraser, S. Kawi, ACS Catal. 4 (2014) 1526-1536.

35. E. Baktash, P. Littlewood, R. Schomacker, A. Thomas, P.C. Stair, Appl. Catal. B: Environ. 179 (2015) 122-127.

36. S.B. Wang, G.Q.M. Lu, Appl. Catal. B: Environ. 16 (1998) 269-277.

37. Z. Gao, M. Dong, G.Z. Wang, P. Sheng, Z.W. Wu, H.M. Yang, B. Zhang, G.F. Wang, J.G. Wang, Y. Qin, Angew. Chem. Int. Ed. 54 (2015) 9006-9010.

38. Y.G. Chen, J. Ren, Catal. Lett. 29 (1994) 39-48.

39. T. Mattisson, M. Johansson, E. Jerndal, A. Lyngfelt, Can. J. Chem. Eng. 86 (2008) 756-767.

40. G. Ertl, R. Hierl, H. Knozinger, N. Thiele, H.P. Urbach, Appl. Surf. Sci. 5 (1980) 49-64.

41. A.B. Mandale, S. Badrinarayanan, S.K. Date, A.P.B. Sinha, J. Electron Spectrosc. Relat. Phenom. 33 (1984) 61-72.

42. L. Salvati Jr, L.E. Makovsky, J.M. Stencel, F.R. Brown, D.M. Hercules, J. Phys. Chem. 85 (1981) 3700-3707.

43. C.P. Li, A. Proctor, D.M. Hercules, Appl. Spectrosc. 38 (1984) 880-886.

44. A.N. Mansour, Surf. Sci. Spectra 3 (1994) 231-238.

45. Z.Y. Hou, O. Yokota, T. Tanaka, T. Yashima, Catal. Lett. 89 (2003) 121-127.

46. J.M. Rynkowski, T. Paryjczak, M. Lenik, Appl. Catal. A: Gen. 126 (1995) 257-271.

47. P. Kim, J.B. Joo, H. Kim, W. Kim, Y. Kim, I.K. Song, J. Yi, Catal. Lett. 104 (2005) 181-189.

48. N. Ichikuni, D. Murata, S. Shimazu, T. Uematsu, Catal. Lett. 69 (2000) 33-36.

49. G.H. Li, L.J. Hu, J.M. Hill, Appl. Catal. A: Gen. 301 (2006) 16-24.

SUPPLEMENTARY INFORMATION

Ni ALD: Ni ALD was carried out using bis(cyclopentadienyl)nickel ($NiCp_2$) and hydrogen as precursors at 300 °C in a fluidized bed reactor, as described in detail previously [1]. The solid $NiCp_2$ precursor was loaded into a heated bubbler and carried by nitrogen gas into the reactor. Both dense alumina nanoparticles (BET surface area of 137 m^2/g) and porous γ-alumina particles (BET surface area of 95.5 m^2/g) were used as substrates for Ni ALD and degassed under a nitrogen flow in the reactor before ALD reactions. The particle substrates were fully fluidized during precursor dose time and nitrogen flush time. By introducing the $NiCp_2$ precursor into the reactor, the O-H bond of the hydroxyl groups on the substrate was replaced by an O-Ni bond, due to the reaction of the $NiCp_2$ precursor with the OH groups. During the nitrogen purge step, the excess $NiCp_2$ precursor was removed to prevent a chemical vapor deposition reaction between the excess $NiCp_2$ precursor and the incoming hydrogen gas. In the next step, hydrogen was introduced to remove organic ligands on Ni surfaces, and to regenerate the surface hydroxyl groups.

A nitrogen purge process was also applied to remove excess hydrogen. This is the so-called "one cycle of Ni ALD". In this study, one cycle of Ni ALD was applied on both substrates, and the Ni loading was 0.97 wt. %. A longer Ni precursor dose time was used for porous γ-alumina particles. These two catalysts were labeled as ALD Ni/γ-Al$_2$O$_3$, and ALD Ni/NP-Al$_2$O$_3$, respectively. To obtain a better characterization result, a porous γ-Al$_2$O$_3$ supported Ni catalyst, with a Ni loading of 4.0 wt. %, was synthesized using four cycles of Ni ALD and labeled as ALD 4-Ni/γ-Al$_2$O$_3$.

Effect of reaction temperature on catalyst coking and Ni nanoparticles sintering: To study the effects of reaction temperature on catalyst coking and Ni nanoparticles sintering, the DRM reactions were carried out at two different temperatures. Fig. S4 shows the Ni nanoparticle size distribution of the ALD Ni/NP-Al$_2$O$_3$ catalyst after 50 hours of DRM reaction at 700 °C (increased from ~3.6 nm to 13.5 nm) and after 50 hours of DRM reaction at 850 °C (increased from ~3.6 nm to 19.0 nm), respectively. This indicated that the Ni nanoparticles were sintered at both 700 °C and 850 °C, and the sintering at 850 °C was more severe than that at 700 °C. The coking content was measured by derivative thermogravimetry (DTG) analysis. Fig. S5 shows the DTG results for the three samples (fresh catalyst, and catalysts used at 700 °C and 850 °C). The weight loss at about 250 °C for all three samples was attributed to the removal of physically bonded water. The slight weight loss at 580 °C could have been the expulsion of residual water, since this weight loss was observed for all three samples and, also, on γ-Al$_2$O$_3$ nanoparticles (Fig. S6). A weight loss at 700 °C could only be observed for the catalyst used at 850 °C. This

weight loss was the oxidation of filament carbon (e.g., carbon nanotubes). This result was consistent with the results of a TEM observation that carbon nanotubes could only be observed for the catalyst used at 850 °C (Fig. S7), but could not be observed for the catalyst used at 700 °C. The amorphous carbon on Ni nanoparticles was also observed for both catalysts by TEM, as shown in Fig. S4. After 50 hours of DRM reaction at 700 °C and 850 °C, the average carbon thicknesses for Ni nanoparticles were about 1.7 nm and 2.3 nm, respectively. Thus, the amorphous carbon content could be estimated based on the coking thickness, the size of Ni nanoparticles, and the total loading of Ni nanoparticles. The content was lower than 0.25% for both samples. This could have been the reason that no amorphous carbon was detected by DTG analysis due to the content being too low. The coking on the catalyst was very light during the DRM reaction. Since the ALD Ni/γ-Al$_2$O$_3$ catalyst showed a higher stability, as compared to the ALD Ni/NP-Al$_2$O$_3$ catalyst, it was reasonable to expect that the coking of ALD Ni/γ-Al$_2$O$_3$ catalyst would be even lighter than that of the ALD Ni/NP-Al$_2$O$_3$ catalyst.

X-ray photoelectron spectroscopy (XPS) analysis: The XPS spectra were recorded with a Kratos Axis 165 X-ray photoelectron spectrometer using a monochromatic Al Kα radiation (hν = 1486.6 eV), at a take-off angle of 0°. The survey scan spectra and C (1s), Ni (2p) core level spectra were recorded at a pass energy of 80 eV and 20 eV, respectively. All binding energy values were corrected based on a C (1s) signal at 284.5 eV. Three samples were analyzed: as-deposited ALD 4-Ni/γ-Al$_2$O$_3$, oxidized ALD 4-Ni/γ-

Al_2O_3, and the oxidized sample reduced in 45% H_2 and 55% CO (with a total flow rate of 100 sccm) at 850 °C for 120 hours.

X-Ray diffraction (XRD) analysis: Powder XRD spectra were recorded by a Philips X-Pert Multi-purpose Diffractometer, using Cu Kα 1 radiation (λ=0.15416 nm) at 45 kV tube voltage, and 40 mA tube current with a scanning speed of 1.5°/min between 5° and 90° 2θ. Four samples were analyzed: as-deposited ALD 4-Ni/γ-Al_2O_3, oxidized ALD 4-Ni/γ-Al_2O_3, and the oxidized sample reduced in 45% H_2 and 55% CO (with a total flow rate of 100 sccm) at 850 °C for 20 hours and 120 hours, respectively. As shown in Fig. S12, the spectra of the as-deposited ALD sample and the sample oxidized at 550 °C showed almost no difference, and did not conclusively demonstrate the existence of NiO and $NiAl_2O_4$. The XPS results verified the existence of $NiAl_2O_4$ spinel in the ALD prepared Ni nanoparticle catalyst supported on porous γ-alumina particles (discussed in the main manuscript). After 20 hours of reduction in 45 % H_2 and 55% CO (with a total flow rate of 100 sccm), metallic Ni peaks were observed (44.5°, 51.8°, and 76.3°) [2, 3]. After the sample was reduced for 120 hours, higher Ni peaks were observed. The new peaks at 31.9°, 34.8°, 38.7°, and 56.2° of the reduced samples were from an orthorhombic crystal system of alumina, indicating the phase change of alumina support after reduction at 850 °C [4]. The peaks at 29.3° and 48.5° of the reduced samples were from nickel carbide [5], which was due to the carbon formation from the Boudouard reaction ($2CO \rightleftharpoons CO_2+C$). The strong peaks at 26.3° and 65° for the sample reduced for 120 hours were from SiO_2 [6], since

quartz fiber was applied to support the catalyst in the reduction process and some quartz

fiber may have been mixed with the sample.

REFERENCES

1.   X.H. Liang, L.F. Hakim, G.-D. Zhan, J.A. McCormick, S.M. George, A.W. Weimer, J.A. Spencer II, K.J. Buechler, J. Blackson, C.J. Wood, J. Am. Ceram. Soc. 90 (2007) 57-63.

2.   Y.G. Chen, J. Ren, Catal. Lett. 29 (1994) 39-48.

3.   H.E. Swanson, E. Tatge, R.K. Fuyat, (1953).

4.   B. Ollivier, R. Retoux, P. Lacorre, D. Massiot, G. Ferey, J. Mater. Chem. 7 (1997) 1049-1056.

5.   Y.-X. Zhao, C.W. Bowers, I.L. Spain, Carbon 26 (1988) 291-293.

6.   W.A. Bassett, D. Lapham, Am. Mineral. 42 (1957) 548-555.
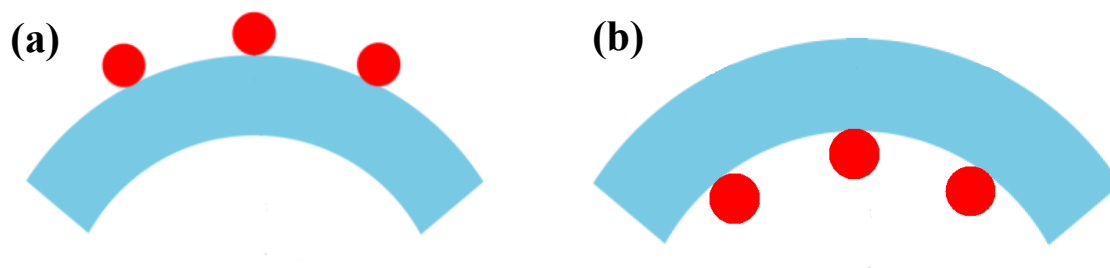
Fig. S1. Catalyst nanoparticles supported on (a) convex surface and (b) concave surface. There is more interfacial contact between nanoparticles and the concave surface, as compared to the case of a convex surface.

Fig. S2. Photo of fresh and used ALD Ni/γ-Al$_2$O$_3$ catalysts. The white particles in the used catalyst are quartz sands, and the darker color is from coking.
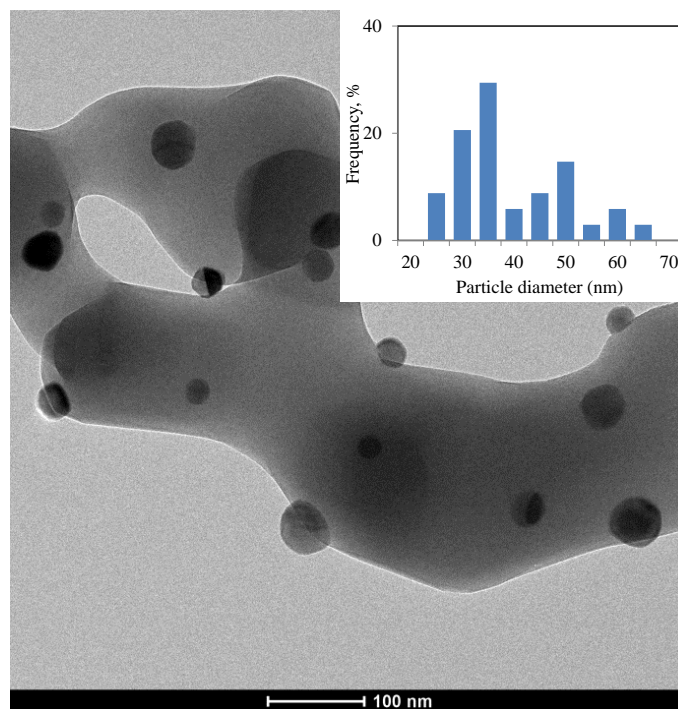
Fig. S3. TEM image of an ALD Ni/NP-Al$_2$O$_3$ catalyst after three cycles of DRM reactions. The inset image shows the size distribution of Ni nanoparticles. The alumina nanoparticles supports were sintered to form larger particles.
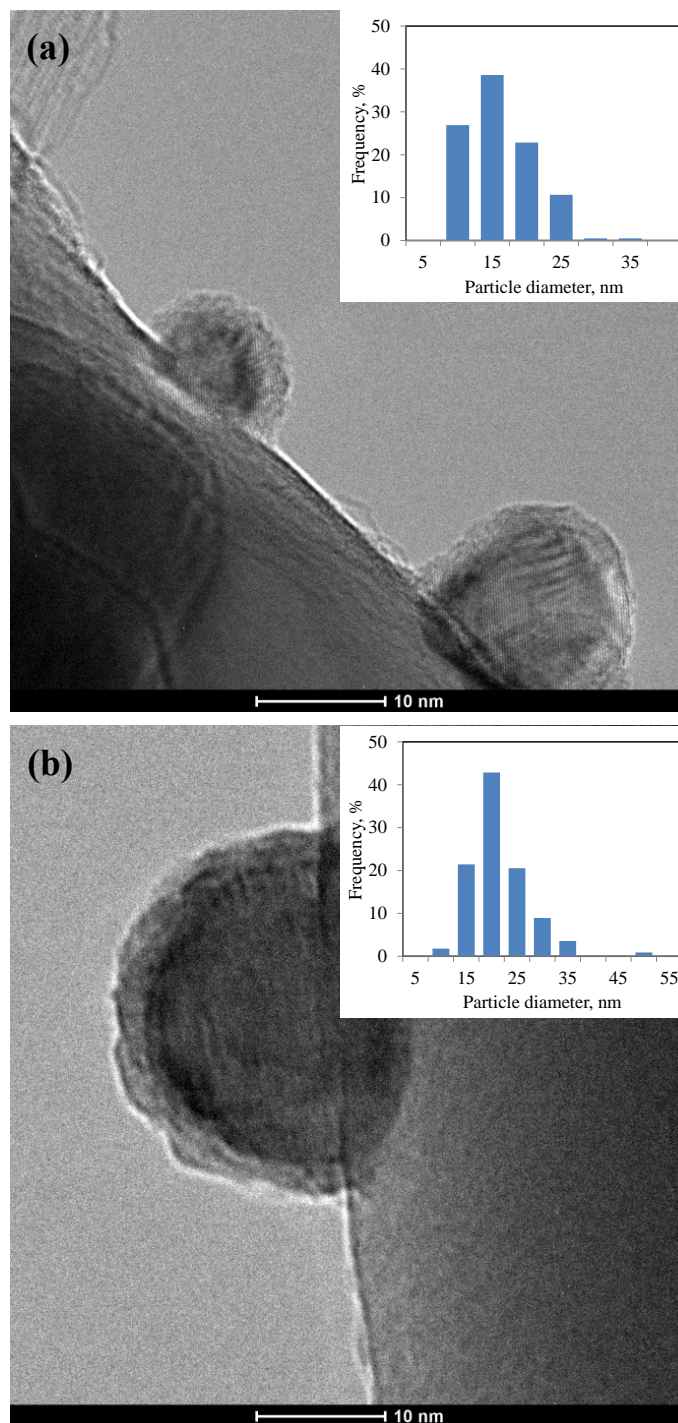
Fig. S4. TEM images of an ALD Ni/NP-Al$_2$O$_3$ catalyst (a) after 50 h of DRM reaction at 700 °C and (b) after 50 h of DRM reaction at 850 °C. The inset figures show the size distributions of Ni nanoparticles.
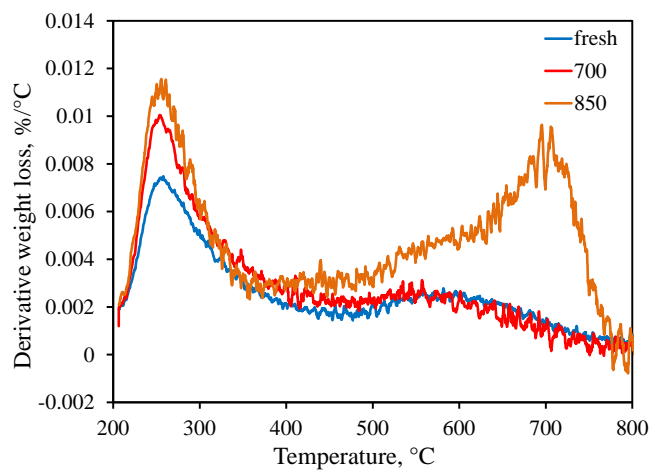
Fig. S5. DTG analysis of a fresh ALD Ni/NP-Al$_2$O$_3$ catalyst and the catalysts used at 700 °C for 50 h and at 850 °C for 50 h, respectively.
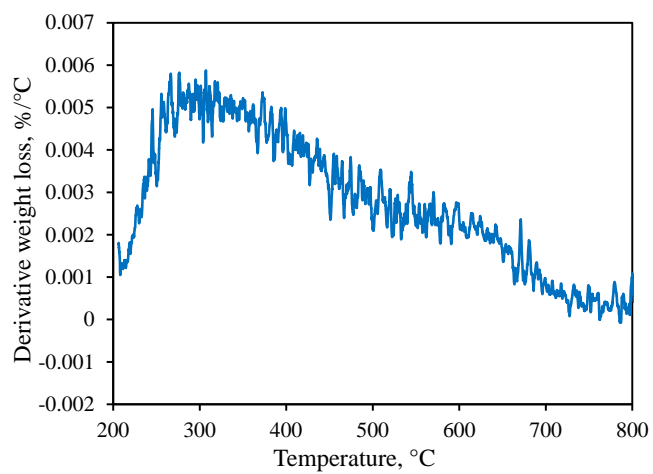
Fig. S6. DTG analysis of γ-Al$_2$O$_3$ nanoparticles.
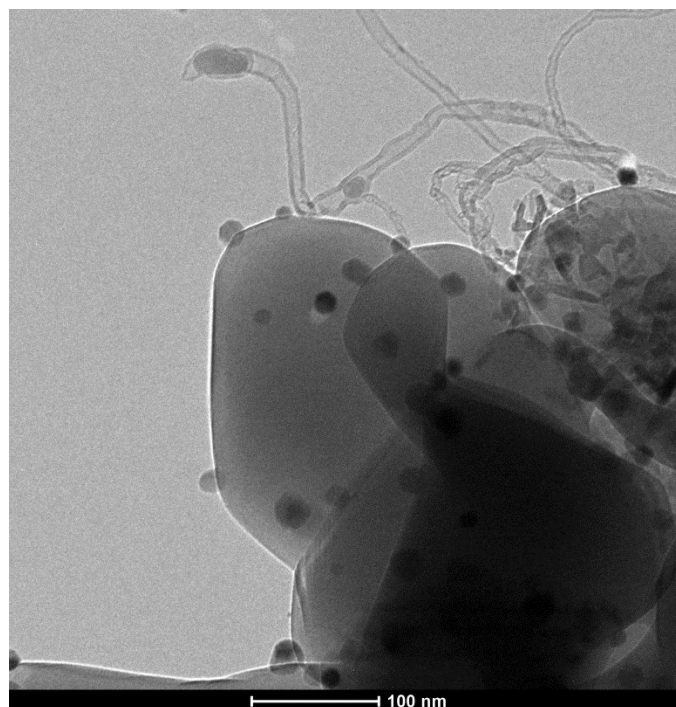
Fig. S7. TEM images of an ALD Ni/NP-Al$_2$O$_3$ catalyst after 50 h of DRM reaction at 850 °C. Carbon nanotubes can be observed on the catalyst used at 850 °C.
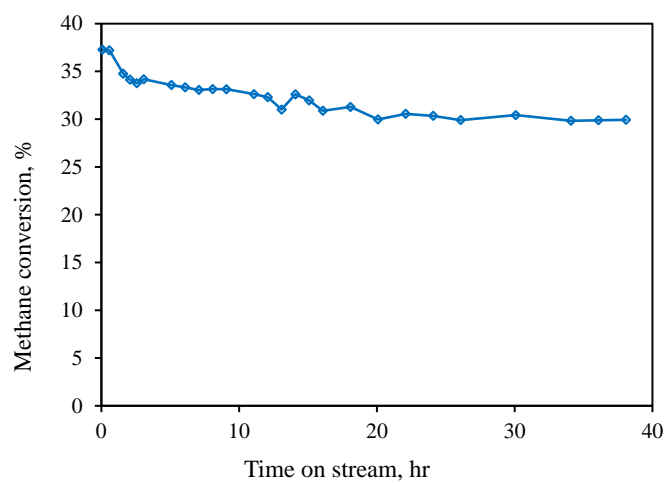
Fig. S8. Methane conversion of dry reforming of methane catalyzed by ALD Ni/NP-Al$_2$O$_3$ at 700°C. The ALD Ni/NP-Al$_2$O$_3$ catalyst was reduced at 700 °C for 1 h and then directly used for DRM at 700 °C.
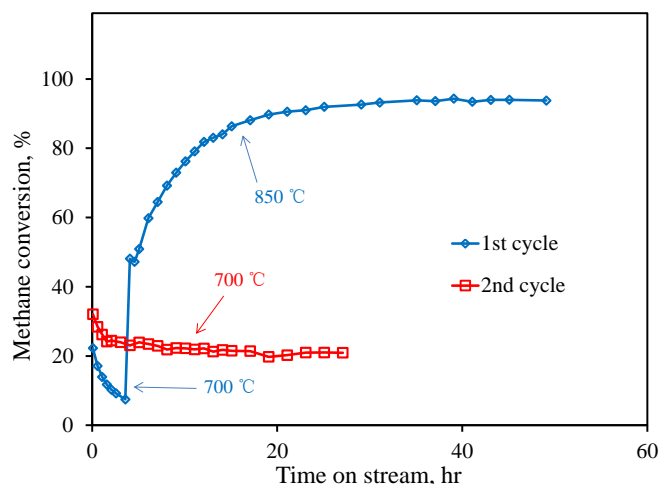
Fig. S9. Methane conversion of dry reforming of methane catalyzed by an ALD Ni/γ-Al$_2$O$_3$ catalyst reduced by carbon monoxide and hydrogen mixture. The fresh ALD Ni/γ-Al$_2$O$_3$ catalyst was reduced in 16% H$_2$, 20% CO (H$_2$/CO ratio was similar to the gas mixture of H$_2$ and CO in the product of DRM at 850 °C) and 64% Ar (with a total flow rate of 100 sccm) at 850 °C for 10 h.
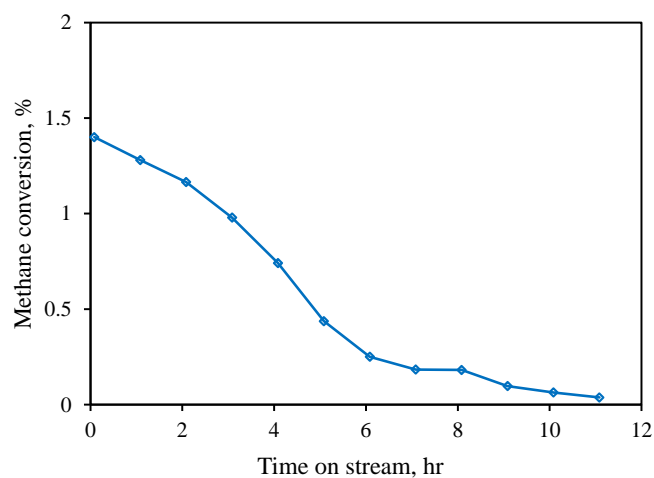
Fig. S10. Methane conversion of dry reforming of methane catalyzed by methane reduced ALD Ni/γ-Al$_2$O$_3$. The fresh ALD Ni/γ-Al$_2$O$_3$ catalyst was reduced in 20% CH$_4$ and 80% Ar (with a total flow rate of 100 sccm) at 850 °C for 10 h.
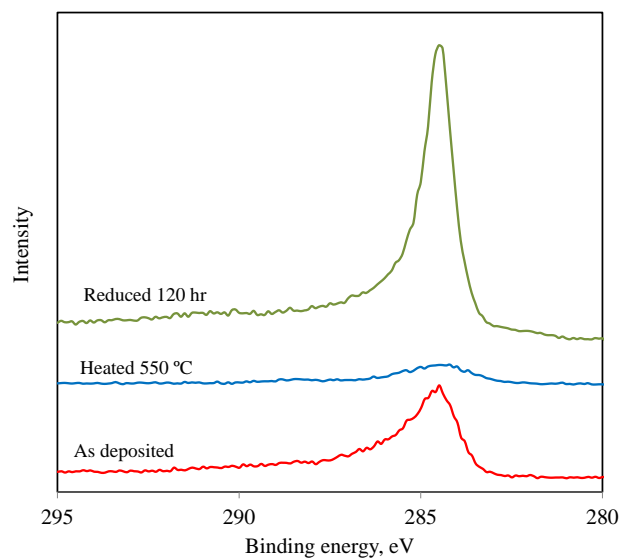
Fig. S11. High resolution XPS spectra of carbon (1s) of as-deposited ALD 4-Ni/γ-Al$_2$O$_3$ sample and the sample oxidized at 550 °C before and after reduction.
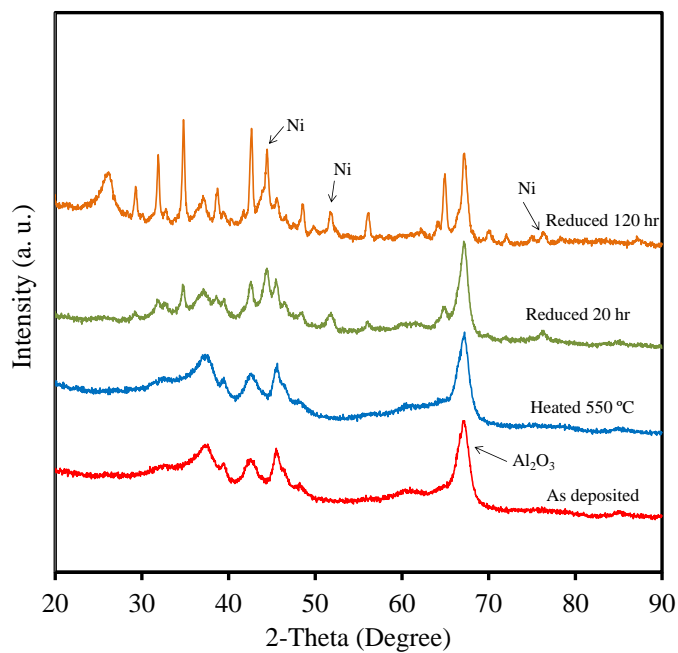
Fig. S12. XRD spectra of as-deposited ALD 4-Ni/γ-Al$_2$O$_3$ sample and the sample first oxidized at 550 °C and then reduced at 850 °C for different lengths of time.

V. NANO-ENGINEERED NICKEL CATALYSTS SUPPORTED ON 4-CHANNEL A-AL2O3 HOLLOW FIBERS FOR DRY REFORMING OF METHANE

Zeyu Shang

Department of Chemical and Biochemical Engineering, Missouri University of Science and Technology, Rolla, Missouri 65409, United States

Shiguang Li

Gas Technology Institute, 1700 South Mount Prospect Road, Des Plaines, Illinois 60018, United States

Qingfa Wang

Department of Chemical and Biochemical Engineering, Missouri University of Science and Technology, Rolla, Missouri 65409, United States

Key Laboratory for Green Chemical Technology of the Ministry of Education, School of Chemical Engineering and Technology, Tianjin University, 92 Weijin Road, Tianjin 300072, P. R. China

Xuehong Gu

State Key Laboratory of Materials-Oriented Chemical Engineering, College of Chemistry and Chemical Engineering, Nanjing Tech University, 5 Xinmofan Road, Nanjing 210009, P.R. China

Xinhua Liang

Department of Chemical and Biochemical Engineering, Missouri University of Science

and Technology, Rolla, Missouri 65409, United States

ABSTRACT

A nickel (Ni) nanoparticle catalyst, supported on 4-channel α-Al$_2$O$_3$ hollow fibers, was synthesized by atomic layer deposition (ALD). Highly-dispersed Ni nanoparticles were successfully deposited on the outside surface and inside porous structure of hollow fibers. The catalyst was employed to catalyze dry reforming of methane (DRM) reaction and showed a methane reforming rate of 2040 $Lh^{-1}g_{Ni}^{-1}$ at 800 °C. NiAl$_2$O$_4$ spinel was formed when Ni nanoparticles were deposited on alpha-alumina substrates by ALD, which could enhance the Ni-support interaction. Different cycles (2, 5, and 10) of Al$_2$O$_3$ ALD films were applied on the Ni/hollow fiber catalysts to further improve the interaction between the Ni nanoparticles and the hollow fiber support. Both the catalyst activity and stability were improved with the deposition of Al$_2$O$_3$ ALD films. Among the overcoated catalysts, the catalyst with 5 cycles of Al$_2$O$_3$ ALD showed the best performance.

Topical Heading: Reaction Engineering, Kinetics and Catalysis

Keywords: atomic layer deposition (ALD), nickel nanoparticles, dry reforming of methane (DRM), hollow fiber

1. INTRODUCTION

The dry reforming of methane (DRM, $CH_4+CO_2 \rightarrow 2H_2+2CO$), has been proposed as an important reaction for the utilization of carbon dioxide. In this reaction, syngas (carbon monoxide and hydrogen) is produced and can be employed in Fischer−Tropsch synthesis (FTS) to produce liquid hydrocarbons, or converted to methanol or dimethyl ether in catalytic processes.[1,2] The H_2/CO ratio of syngas produced by the DRM reaction is lower than 1 due to the accompanied reverse water-gas shift reaction ($CO_2+H_2 \rightleftharpoons CO+H_2O$). Such syngas is suitable for FTS reaction to produce chemicals with high values, since the lower H_2/CO ratio in the feedstock gas could lead to a higher selectivity of C_{5+} in the products of FTS.[3,4] Nickel-based catalysts[5,6] were popularly investigated for DRM because of the relatively low cost and adequate availability. The main drawback of Ni-based catalysts for industrial application is the deactivation of the catalyst caused by coking and/or sintering.[7] It is highly desirable to develop a coking- and sintering-resistant Ni-based catalyst.

The formation of $NiAl_2O_4$ spinel is favorable in reducing the coking and retarding the sintering.[8,9] Therefore, alumina was widely employed as catalysts support for DRM reactions. Atomic layer deposition (ALD), has been reported to prepare Ni nanoparticles for DRM reactions. Gould et al.[10] deposited Ni nanoparticles (~3 nm) on nonporous γ-Al_2O_3 nanoparticles for DRM reaction. Our recent work revealed that the interaction between the alumina support and the ALD Ni nanoparticles was the key for the high activity and stability of ALD Ni nanoparticles for DRM reaction.[11] The formation of $NiAl_2O_4$ spinel

increased the thermal stability of the catalyst, and partial reduction of $NiAl_2O_4$ spinel to metallic Ni under the reductive atmosphere in DRM reaction at 850 °C greatly increased the catalytic activity.[11]

Though γ-Al_2O_3 was widely used as support for Ni-based catalysts, it is not suitable for the methane reforming process due to phase transformation at elevated temperatures, which also accompanies with coarsening and marked decrease in surface area.[12,13] Among different phases of Al_2O_3, α-Al_2O_3 is the most thermally and mechanically stable phase, which makes it more suitable for industrial applications. α-Al_2O_3 has been employed to prepare industrial packed bed catalyst support.[14] The packed bed reactor has advantages of reduced surface area loss caused by attrition, and low maintenance and operation cost. The geometric surface area to volume ratio of the industrial catalyst is a major factor, which affects the catalyst activity. Therefore, development of strong shaped catalyst with a large surface area and voidage is highly desirable. Ceramic hollow fiber has high packing density due to its high surface area per unit volume, which is important for the catalysts in industrial process.[15,16] Generally, it is relatively hard to form $NiAl_2O_4$ spinel on α-Al_2O_3 supported Ni catalysts.[17] In this report, we deposited highly dispersed Ni nanoparticles on a novel four-channel α-Al_2O_3 hollow fibers with geometric surface area to volume as high as 3,000 m^2/m^3 by ALD and applied this catalyst for DRM reaction. The 4-channel hollow fiber had a higher surface area per unit volume and mechanical strength than conventional single-channel ceramic hollow fibers and some other conventional industrial catalyst supports. To increase the interaction between Ni nanoparticles and α-Al_2O_3 hollow fibers, a few cycles

of alumina ALD were applied. The Ni catalyst supported on α-Al_2O_3 hollow fiber had higher catalytic activity than the previously reported ALD Ni/γ-Al_2O_3 catalyst in DRM reaction under the same operation conditions.

2. EXPERIMENTAL

2.1. Catalyst Preparation. The synthesis of 4-channel α-Al_2O_3 hollow fibers (Figure 1) was described in detail elsewhere.[18] Ni nanoparticles were deposited by ALD using bis(cyclopentadienyl)nickel (NiCp$_2$, Alfa Aesar) and hydrogen as precursors in a viscous flow reactor at 300 °C. The solid NiCp$_2$ precursor was loaded into a heated bubbler and carried by nitrogen gas into the ALD reactor. Five cycles of Ni ALD were applied on the α-Al_2O_3 hollow fibers and the catalyst was labeled as Ni/α-Al_2O_3-HF. In addition, we also attempted to coat Al_2O_3 thin films onto the Ni/α-Al_2O_3-HF by ALD in the same reactor at 177 °C using trimethylaluminum (TMA, Sigma-Aldrich) and water as precursors to increase the interaction between the Ni nanoparticles and alumina catalyst support. In that case, different cycles (2, 5, and 10) of Al_2O_3 ALD films were coated on the Ni/α-Al_2O_3 HF catalyst. The catalysts were labeled as 2Al_2O_3-Ni/α-Al_2O_3-HF, 5Al_2O_3-Ni/α-Al_2O_3-HF, and 10Al_2O_3-Ni/α-Al_2O_3-HF, respectively. For the ease of characterization, another sample of Ni nanoparticles supported on nonporous α-Al_2O_3 nanoparticles (US Research Nanomaterials) was synthesized by applying 5 cycles of Ni ALD on the nonporous α-Al_2O_3 nanoparticles in a fluidized bed reactor, as described in detail previously.[19] This sample was labeled as Ni/α-Al_2O_3-NPs. To demonstrate that ALD is a better way to synthesize Ni

nanoparticles as compared to conventional impregnation method, another batch of Ni

catalyst supported on four-channel α-Al$_2$O$_3$ hollow fibers was synthesized by impregnation

method. The α-Al$_2$O$_3$ hollow fibers were added into an aqueous solution of Ni(NO$_3$)$_2$·6H$_2$O

(Fisher Chemical) and dried at 110 °C with continuously stirring. The sample was then

calcined in air at 550 °C for 6 hours. This sample was labeled as IM-Ni/α-Al$_2$O$_3$-HF.

Figure 1. Photos of four-channel structured α-Al$_2$O$_3$ hollow fibers.

2.2. Dry reforming of Methane. DRM reactions were carried out in a quartz tube

reactor (10 mm in diameter), and quartz wool was employed to support the catalyst.

Different amount of catalysts for catalysts with different Ni contents were loaded into the

reactor to keep the Ni contents consistent (~0.73 mg). Hollow fiber supported catalysts were cut into short pieces (~1 cm in length) and stacked in the reactor tube. A thermal couple was employed to measure the reactor temperature. All catalysts were reduced for one hour in an atmosphere of 20% H2 and 80% Ar (with a total flow rate of 100 sccm) at 700 °C before the DRM reaction. A mixture of methane and carbon dioxide (60 sccm, CH_4/CO_2=1:1) was introduced into the reactor at different temperatures for the DRM reaction. The gas flow rates were controlled by MKS® mass flow controllers. The catalysts were regenerated after certain length of reaction time and then applied to catalyze the DRM reaction again. In a typical regeneration process, the catalyst was first oxidized at 700 °C in 20% O_2 and 80% Ar for one hour and then reduced in 20% H_2 and 80% Ar at the same temperature for one hour. The reaction products were analyzed by an online gas chromatograph (SRI 8610C) equipped with a 6-foot HAYESEP D column, a 6-foot MOLECULAR SIEVE 13X column, and a thermal conductivity detector (TCD).

2.3. Catalyst Characterization. Inductively coupled plasma-atomic emission spectroscopy (ICP-AES) was employed to investigate the Ni content of the catalysts. Transmission electron microscopy (TEM) was applied to observe the Ni nanoparticles. The specific surface areas of the catalysts were calculated using the Brunauer–Emmett–Teller (BET) method from the N_2 adsorption isotherms of the catalysts obtained at -196 °C using a Quantachrome Autosorb-1. The Ni redox status and the interaction between the Ni nanoparticles and the alumina support was investigated by X-ray photoelectron spectroscopy (XPS). The XPS spectra were recorded with a Kratos Axis 165 X-ray

photoelectron spectrometer using a monochromatic Al Kα radiation (hν = 1486.6 eV), at a take-off angle of 0°. The C (1s), Ni (2p) core level spectra were recorded at a pass energy of 20 eV. All binding energy values were corrected based on C (1s) signal at 284.5 eV.

3. RESULTS AND DISCUSSION

3.1. Characterization of Ni Catalyst. Ni content is 0.12 wt.% after 5 cycles of Ni ALD deposited on the α-Al$_2$O$_3$ hollow fibers, determined by ICP−AES. The Ni loadings were 2.91 wt.% and 0.47 wt.% for Ni/α-Al$_2$O$_3$-NPs and IM-Ni/α-Al$_2$O$_3$-HF catalysts, respectively. Since it's very difficult to prepare cross-sectioned samples of Ni/α-Al$_2$O$_3$-HF catalyst for TEM analysis, TEM was applied on the Ni/α-Al$_2$O$_3$-NPs particles (~80 nm in diameter). Figure 2 shows a TEM image of Ni/α-Al$_2$O$_3$-NPs catalyst. The black spots in the figure are Ni nanoparticles, and the inset figure shows an average Ni nanoparticle size of about 3.1 nm, which is close to the value reported by Medlin's group[20] and our previous work.[11,21] It is reasonable to expect that the Ni nanoparticles deposited on the hollow fibers by ALD should have a similar particle size.

Al-Megeren et al.[14] compared different industrial catalysts for methane reforming and found out that the best catalyst was a 10-hole catalyst consisting of pure α-Al$_2$O$_3$, which showed a geometric surface area to volume ratio of 2,013 m^2/m^3 and a BET surface area of 3.0-3.5 m^2/g. In this study, the BET surface area and the geometric surface area to volume ratio of the 4-channel α-Al$_2$O$_3$ hollow fiber were 4.76 m^2/g and 3,000 m^2/m^3, respectively. The higher geometric surface area to volume ratio of the 4-channel structured

hollow fiber is due to the higher specific surface area. Since the geometric surface area is an important factor for the catalyst activity, the 4-channel hollow fiber is expected to be a better support for industrial methane reforming catalyst.[14] As compared to conventional impregnation method, ALD was demonstrated to be a better method to prepare alumina supported Ni nanoparticle catalyst for DRM reaction due to the highly dispersed Ni nanoparticles and the formation of $NiAl_2O_4$ spinel during ALD.[11] Therefore, it is anticipated that the ALD synthesized $Ni/\alpha-Al_2O_3$-HF would show excellent performance for DRM reaction.
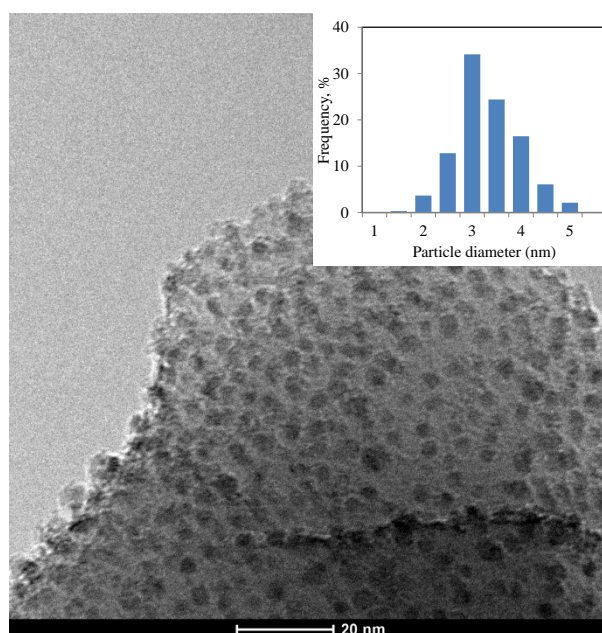

Figure 2. TEM image of Ni nanoparticles deposited on nonporous alumina nanoparticles. The inset image shows the size distribution of Ni nanoparticles.

High resolution XPS on Ni (2p) was employed on the ALD (15 cycles) Ni nanoparticles supported on nonporous α-Al$_2$O$_3$ nanoparticles. As shown in Figure 3, a strong peak at 852.5 eV represents metallic Ni[22] and the small peak at 855.8 eV represents NiAl$_2$O$_4$ spinel.[23] Only little amount of NiO was observed at 861 eV.[24] Typically, the NiAl$_2$O$_4$ spinel can be formed by calcination of Ni/alumina samples at a relative high temperature in the presence of oxygen. It was reported that NiAl$_2$O$_4$ spinel could be formed by calcining Ni/α-Al$_2$O$_3$ sample prepared by impregnation method at 1300 °C, but not at 800 °C.[17,25] However, in this study, NiAl$_2$O$_4$ was formed in the as-deposited Ni/α-Al$_2$O$_3$-NPs by ALD. This was also observed in as-deposited ALD synthesized Ni/gamma-alumina catalysts, as reported in our previous study.[11] Obviously, the synthesis of Ni nanoparticles using ALD technique would be different from some other conventional methods, such as impregnation method. The ALD synthesized Ni nanoparticles would have stronger interaction with the support due to the existence of NiAl$_2$O$_4$.

3.2. Dry Reforming of Methane. The Ni/α-Al$_2$O$_3$-HF, Ni/α-Al$_2$O$_3$-NPs, and IM-Ni/α-Al$_2$O$_3$-HF catalysts were employed to catalyze the DRM reaction, and the results are shown in Figure 4. The reaction catalyzed by Ni/α-Al$_2$O$_3$-HF was first carried out at 850 °C. The methane reforming rate was 2150 Lh^{-1}g$_{Ni}^{-1}$ at the beginning and decreased with the increase in reaction time, which could be due to the sintering of Ni nanoparticles or the poisoning of the catalyst by some gas molecules or both. The methane reforming rate was later stabilized at 1970 Lh^{-1}g$_{Ni}^{-1}$ after 36 hours of reaction. After the reaction temperature decreased to 800 °C, the methane reforming rate increased to 2060 Lh^{-1}g$_{Ni}^{-1}$ and slightly

decreased to 2020 $Lh^{-1}g_{Ni}^{-1}$ in 48 hours. The decrease of methane reforming rate at 800 °C was due to the further sintering of Ni nanoparticles or coking of the catalyst or both. The increase of methane reforming rate (after the reaction temperature decreased from 850 °C to 800 °C) was due to the sweep of Ar gas (the flow of CO_2 and CH_4 was stopped and only pure Ar was introduced into the reactor) when the reaction temperature decreased from 850 °C to 800 °C.
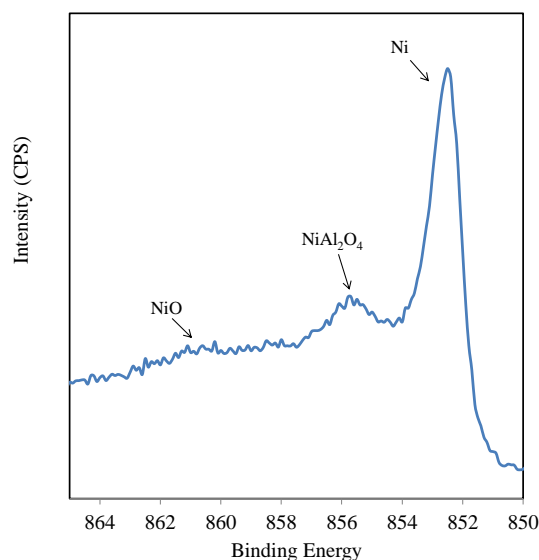
Figure 3. High resolution XPS spectrum of Ni (2p) of as-prepared Ni/alpha-alumina catalysts with 15 cycles of Ni ALD deposited on alpha-alumina nanoparticles.

To confirm this, another two DRM reactions were carried out using the regenerated Ni/α-Al_2O_3-HF catalyst. One reaction was carried out at 850 °C for 48 hours and pure Ar was introduced into the reactor to flush the catalyst for 30 min at 850 °C and the DRM
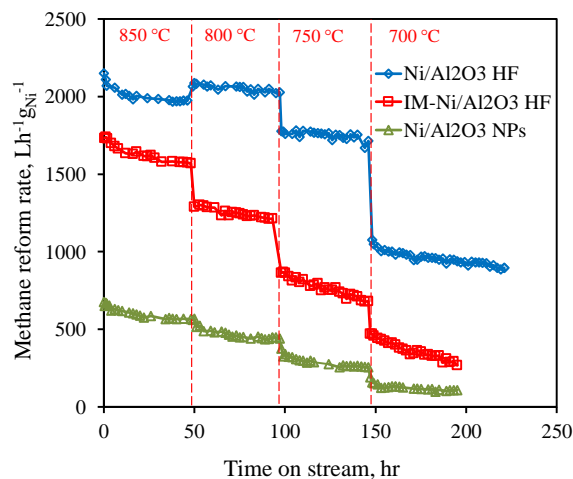
Figure 4. Methane reforming rate of dry reforming of methane catalyzed by Ni/α-Al$_2$O$_3$-HF, Ni/α-Al$_2$O$_3$-NPs, and IM-Ni/α-Al$_2$O$_3$-HF catalysts.

reaction was carried out at 850 °C again. As shown in Figure 5a, the catalyst activity increased after the sweep of Ar. The other reaction was carried out at different temperatures (from 850 °C to 700 °C), but the mixture of CO$_2$ and CH$_4$ was kept passing through the reactor while decreasing the reaction temperature and the catalyst did not show an activity increase after the reaction temperature decreased from 850 °C to 800 °C (Figure 5b). From these sets of experiments, it is demonstrated that the increase of methane reforming rate of Ni/α-Al$_2$O$_3$-HF catalyst after the reaction temperature decreased to 800 °C (Figure 4) was due to the sweep of Ar. This could be due to the fact that the sweep of Ar at high temperatures could remove some poisonous gas molecules (e.g., CO) adsorbed on the active metal nanoparticles. This was further verified since the catalyst showed much lower activities at lower temperatures without Ar passing through while decreasing reaction temperature (Figure 5b).
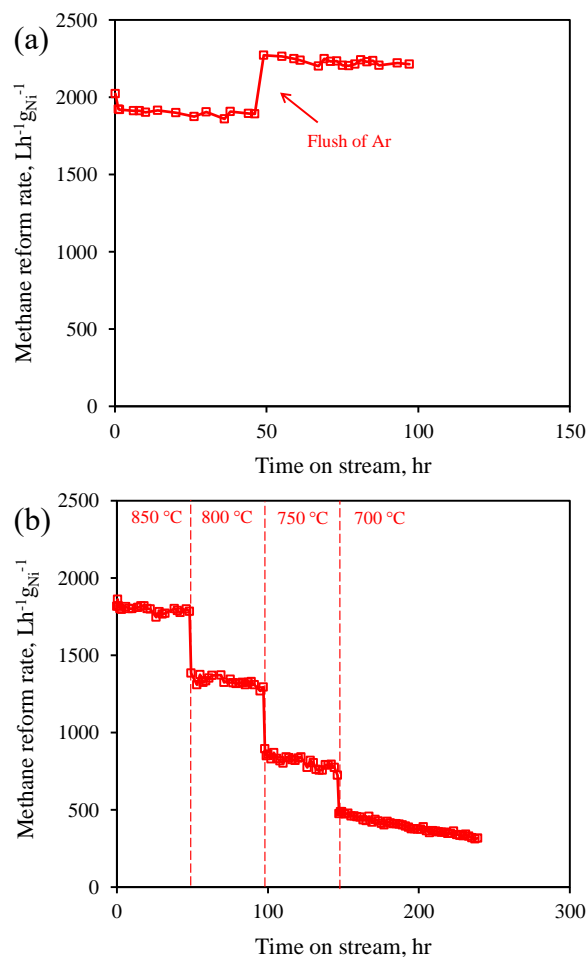
Figure 5. Methane reforming rate of dry reforming of methane catalyzed by Ni/α-Al$_2$O$_3$-HF: (a) after 48 hours of reaction at 850 °C, pure Ar flushed the catalyst for 30 min, and (b) at different temperatures, the mixture of methane and carbon dioxide (60 sccm, CH$_4$/CO$_2$=1:1) was kept passing through the reactor, while decreasing reaction temperatures.

The methane reforming rate decreased to 1780 Lh^{-1}g$_{Ni}^{-1}$ when the reaction temperature decreased to 750 °C and slightly decreased to 1760 Lh^{-1}g$_{Ni}^{-1}$ in 48 hours. When the reaction temperature decreased to 700 °C, the methane reforming rate decreased to 1070 Lh^{-1}g$_{Ni}^{-1}$ and further decreased to 900 Lh^{-1}g$_{Ni}^{-1}$ after 70 hours. This quicker decrease

of catalyst activity at 700 °C compared to that at 750 °C could be due to the fact that coking was more severe at 700 °C, since there would be heavier coking at lower temperatures.[2]

To verify that the hollow fiber structure is beneficial for the catalyst performance, the Ni/α-Al$_2$O$_3$-NPs catalyst was also employed to catalyze DRM reaction at the same temperatures. As shown in Figure 4, the Ni/α-Al$_2$O$_3$-NPs catalyst showed a much worse performance than the Ni/α-Al$_2$O$_3$-HF catalyst. For example, the Ni/α-Al$_2$O$_3$-NPs catalyst showed an average methane reforming rate of 470 Lh^{-1}g$_{Ni}$$^{-1}$ at 800 °C, which is more than 1500 Lh^{-1}g$_{Ni}$$^{-1}$ lower than that of the Ni/α-Al$_2$O$_3$-HF catalyst. The better performance of Ni/α-Al$_2$O$_3$ HF catalyst, as compared to Ni/α-Al$_2$O$_3$ NPs catalyst, should be due to the combined effect of the high spatial dispersion of Ni nanoparticles and the porous structures inside the hollow fiber, which could help limit the sintering of Ni nanoparticles.

The results of DRM reaction catalyzed by IM-Ni/α-Al$_2$O$_3$-HF are also showed in Figure 4. The catalyst showed both lower activity and lower stability as compared to Ni/α-Al$_2$O$_3$-HF. For example, the IM-Ni/α-Al$_2$O$_3$-HF catalyst showed an average methane reforming rate of 1230 Lh^{-1}g$_{Ni}$$^{-1}$ at 800 °C, which is more than 800 Lh^{-1}g$_{Ni}$$^{-1}$ lower than that of Ni/α-Al$_2$O$_3$-HF catalyst. This indicates that ALD is a better way to prepare Ni nanoparticles for DRM reaction than the conventional impregnation method. The IM-Ni/α-Al$_2$O$_3$-HF catalyst showed better performance as compared to Ni/α-Al$_2$O$_3$-NPs, which could also demonstrate that the four-channel hollow fibers are better catalysts supports as compared to the nonporous α-Al$_2$O$_3$ nanoparticles.

These three reactions demonstrated that it is suitable to fabricate α-Al$_2$O$_3$ four-channel hollow fiber supported Ni nanoparticle catalyst by ALD for methane reforming reactions. However, the Ni-support interaction of Ni/α-Al$_2$O$_3$ hollow fiber is not strong enough. Recently, it was demonstrated that an over-coating of alumina ALD films on Ni nanoparticles catalyst could increase the interaction between the Ni nanoparticles and alumina catalyst support.[26] In this study, to increase Ni-support interaction, Ni/α-Al$_2$O$_3$-HF catalyst was coated with different thicknesses of alumina films by ALD. All three coated catalysts 2Al$_2$O$_3$-Ni/α-Al$_2$O$_3$-HF, 5Al$_2$O$_3$-Ni/α-Al$_2$O$_3$-HF, and 10Al$_2$O$_3$-Ni/α-Al$_2$O$_3$-HF were employed to catalyze the DRM reaction and the results are shown in Figure 6a. The DRM results of Ni/α-Al$_2$O$_3$-HF catalyst are also shown in Figure 6a for the ease of comparison. As shown in the figure, all three alumina coated catalysts showed an increase of methane reforming rates after reaction temperature decreased to 800 °C and only pure Ar was passing though the reaction when decreasing the reaction temperature for all reactions. This can further demonstrate the increase of activity of ALD Ni/hollow fiber catalyst after sweep of Ar is not accidental. Among these catalysts, the 2Al$_2$O$_3$-Ni/α-Al$_2$O$_3$-HF catalyst showed the highest activity at 850 °C, and the methane reforming rate stabilized at 2040 Lh^{-1}g$_{Ni}$$^{-1}$. The methane reforming rate slightly increased to 2165 Lh^{-1}g$_{Ni}$$^{-1}$ after the reaction temperature decreased to 800 °C and decreased to 2050 Lh^{-1}g$_{Ni}$$^{-1}$ in 48 hours. When the reaction temperature decreased to 750 °C, the methane reforming rate decreased to 1865 Lh^{-1}g$_{Ni}$$^{-1}$, and further decreased to 1740 Lh^{-1}g$_{Ni}$$^{-1}$ in 48 hours. The methane reforming rate decreased from 1250 Lh^{-1}g$_{Ni}$$^{-1}$ to 690 Lh^{-1}g$_{Ni}$$^{-1}$ in 48 hours at 700 °C.
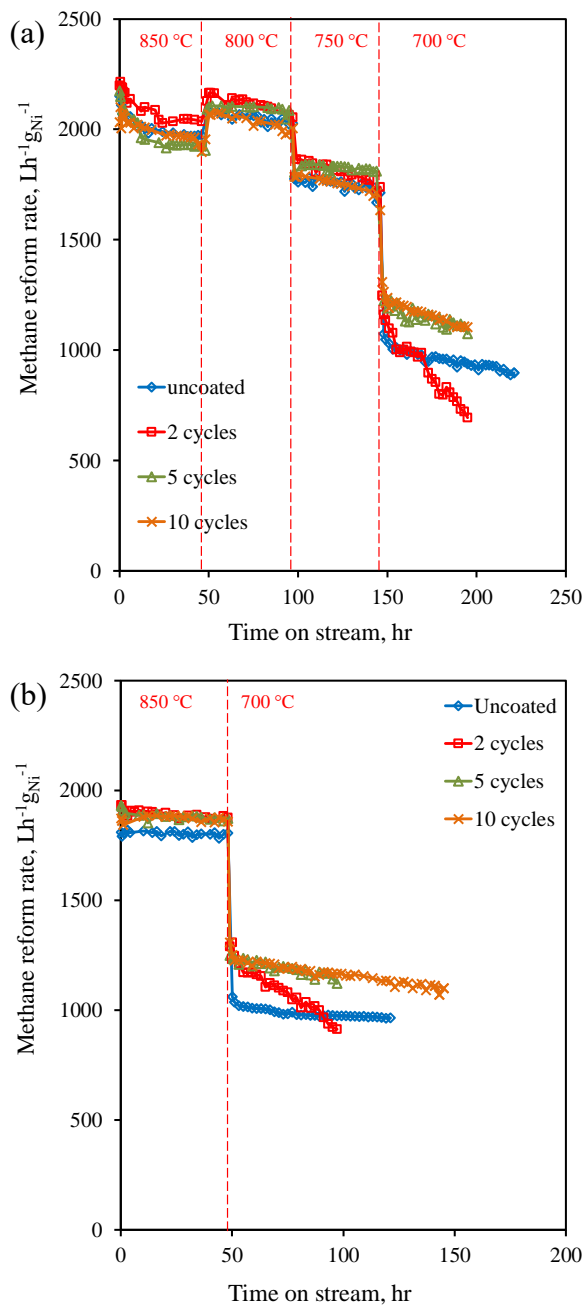
Figure 6. Methane reforming rate of (a) first cycle and (b) second cycle of dry reforming of methane reactions catalysed by Ni/α-Al$_2$O$_3$-HF, 2Al$_2$O$_3$-Ni/α-Al$_2$O$_3$-HF, 5Al$_2$O$_3$-Ni/α-Al$_2$O$_3$-HF, and 10Al$_2$O$_3$-Ni/α-Al$_2$O$_3$-HF.

The higher activities of $2Al_2O_3$-Ni/α-Al_2O_3-HF catalyst at 850 °C, 800 °C, and 750 °C, as compared to those of the naked catalyst, are due to the fact that 2 cycles of Al_2O_3 ALD could improve the interaction between the Ni nanoparticles and the hollow fiber support, which could retard the sintering of Ni nanoparticles. The worse performance of $2Al_2O_3$-Ni/α-Al_2O_3-HF catalyst at 700 °C, as compared to that of the naked catalyst, could be due to the fact that coking was more severe for the $2Al_2O_3$-Ni/α-Al_2O_3-HF catalyst at 700 °C. However, the exact reason is still not clear since the morphology of Ni nanoparticles could influence the coking resistance of the catalyst.[27]

The $5Al_2O_3$-Ni/α-Al_2O_3-HF catalyst showed slightly lower activity at beginning, as compared to that of the $2Al_2O_3$-Ni/α-Al_2O_3-HF catalyst, but much higher stability through the whole reaction process. For the reaction catalyzed by the $5Al_2O_3$-Ni/α-Al_2O_3-HF catalyst, the methane reforming rate was also decreased at the beginning of the reaction, and the result is similar to that of the reaction catalyzed by naked catalyst. The methane reforming rate also increased after the reaction temperature decreased to 800 °C. The methane reforming rate at 800 °C only slightly decreased from 2105 $Lh^{-1}g_{Ni}^{-1}$ to 2095 $Lh^{-1}g_{Ni}^{-1}$ in 48 hours. When the reaction temperature decreased to 750 °C, the methane reforming rate decreased to 1835 $Lh^{-1}g_{Ni}^{-1}$, and slightly decreased to 1815 $Lh^{-1}g_{Ni}^{-1}$ in 48 hours. The methane reforming rate decreased to 1220 $Lh^{-1}g_{Ni}^{-1}$ after the reaction temperature decreased to 700 °C, and further decreased to 1110 $Lh^{-1}g_{Ni}^{-1}$ in 48 hours. It was reported that the growth rate of alumina ALD is about 0.1-0.2 nm per cycle,[28] so 5 cycles of alumina films is less than 1 nm thick. Therefore, the enhanced performance of

the catalyst should not result from stabilization of Ni particles by alumina film encapsulation. The enhanced Ni-support interaction is the key.

The lower activity of the $5Al_2O_3$-Ni/α-Al_2O_3-HF catalyst at the beginning of the reaction compared to that of the $2Al_2O_3$-Ni/α-Al_2O_3-HF catalyst indicates that 5 cycles of Al_2O_3 ALD may block some reactive sites. However, the $5Al_2O_3$-Ni/α-Al_2O_3-HF catalyst showed much better overall performance as compared to the $2Al_2O_3$-Ni/α-Al_2O_3-HF catalyst. This is due to the fact that 5 cycles of Al_2O_3 ALD worked better in retarding the sintering of Ni nanoparticles. Therefore, it can be concluded that stronger interaction between Ni nanoparticles and hollow fiber could be formed after 5 cycles of Al_2O_3 ALD, as compared to the case of 2 cycles of Al_2O_3 ALD. This can also be proved by the higher stability of the $5Al_2O_3$-Ni/α-Al_2O_3-HF catalyst. The $5Al_2O_3$-Ni/α-Al_2O_3-HF also showed a better performance at 700 °C as compared to the Ni/α-Al_2O_3-HF catalyst, which was due to the stronger interaction between the Ni nanoparticles and the catalyst support of the $5Al_2O_3$-Ni/α-Al_2O_3-HF catalyst.

As shown in Figure 6a, the $10Al_2O_3$-Ni/α-Al_2O_3-HF catalyst showed a higher activity and stability at 700 °C compared to the naked catalyst, indicating that the overcoating of 10 cycles of Al_2O_3 ALD still can improve the catalyst performance. However, the $10Al_2O_3$-Ni/α-Al_2O_3-HF catalyst showed a lower activity and stability, as compared to the $5Al_2O_3$-Ni/α-Al_2O_3-HF catalyst at 800 °C and 750 °C. This could be due to the fact that 10 cycles of Al_2O_3 ALD film was too thick and more reactive sites were blocked.

Table 1. Catalytic activities comparison of different catalysts in DRM reaction.

Catalyst	Methane reforming rate ($Lh^{-1}g_{Ni}^{-1}$)			
	850 °C[a]	800 °C	750 °C	700 °C[b]
Ni/α-Al$_2$O$_3$-HF	1970	2040	1770	980
2Al$_2$O$_3$-Ni/α-Al$_2$O$_3$-HF	2040	2120	1775	915
5Al$_2$O$_3$-Ni/α-Al$_2$O$_3$-HF	1970	2100	1825	1160
10Al$_2$O$_3$-Ni/α-Al$_2$O$_3$-HF	1970	2040	1750	1160
ALD Ni/porous γ-Al$_2$O$_3$[11]	1840	1740	1320	720
Ni/MgAl$_2$O$_4$[29]	N/A	N/A	1300	N/A
Inverse Ni/Al$_2$O$_3$ catalyst[30]	N/A	1500	N/A	N/A
ALD Ni/dense γ-Al$_2$O$_3$[10]	N/A	N/A	N/A	700

[a]The methane reforming rates at 850 °C in this work are stabilized value after 48 hours of reaction.
[b]The methane reforming rates at 700 °C in this work are the average value of the reaction at the first 48 hours at 700 °C.

The catalytic activities of different Ni-based catalysts are compared, as shown in Table 1. The hollow fiber supported ALD Ni nanoparticle catalyst showed a high methane reforming rate at lower temperatures even after a long time of reaction at higher temperatures. Compared to our previous results[11] and the results reported by other groups, the 5Al$_2$O$_3$-Ni/α-Al$_2$O$_3$-HF catalyst demonstrated the best performance. Therefore, 5

cycles of Al_2O_3 ALD is an optimal Al_2O_3 ALD film thickness to enhance the catalyst performance. The high activity of the catalyst should attribute to the highly dispersed Ni nanoparticles deposited by ALD, and the strong interaction between the Ni nanoparticles and the support.

All four catalysts were regenerated and employed to catalyze the DRM reactions again. The reactions were carried out at 850 °C for 48 hours and then the reaction temperature was directly decreased to 700 °C. For the reaction catalyzed by the Ni/α-Al_2O_3-HF, the methane reforming rate at 850 °C was about 1810 $Lh^{-1}g_{Ni}^{-1}$, which is 160 $Lh^{-1}g_{Ni}^{-1}$ lower than that in the first cycle (Figure 6b). This is probably due to the sintering of Ni nanoparticles during the first cycle of reaction. The methane reforming rate did not decrease in 48 hours for the reaction at 850 °C, indicating the high thermal stability of the catalyst. The catalyst activity at 700 °C was similar to that of the 1st cycle of reaction. The decrease of catalyst activity at 700 °C should be due to the coking of the catalyst.[2] All three Al_2O_3 ALD overcoated catalysts gave 1870 $Lh^{-1}g_{Ni}^{-1}$ of average methane reforming rates at 850 °C and there was almost no decrease in 48 hours of reaction. The decreases of methane reforming rate indicate that there was slightly sintering of Ni nanoparticles after reaction at 850 °C in the 1st cycle reactions for all three coated catalysts. The decreases of methane reforming rates for 5Al_2O_3-Ni/α-Al_2O_3-HF and 10Al_2O_3-Ni/α-Al_2O_3-HF catalysts were much lower compared to that of the naked catalyst, thus it is demonstrated that the alumina ALD overcoating could inhibit sintering of Ni nanoparticles. The catalysts overcoated with 5 and 10 cycles of alumina ALD showed much higher methane reforming

rate at 700 °C as compared to the naked catalyst in the 2nd cycle of reactions. This further verifies that the overcoating of Al$_2$O$_3$ ALD films is helpful for catalyst performance enhancement.

4. CONCLUSION

Highly dispersed nickel nanoparticles were deposited on the porous structure of alpha-alumina 4-channel hollow fibers by ALD. The Ni catalysts were used for DRM reactions and showed excellent performance due to the high dispersion of Ni nanoparticles and the strong interaction between Ni nanoparticles and the alpha-alumina support. Ultra-thin alumina ALD films were deposited on the catalyst to further increase the catalyst activity and stability. It is believed that the improved performance of coated catalysts was resulted from the overcoating of alumina ALD films on the catalyst, which increased the interaction between the Ni nanoparticles and the support. The success of synthesizing these catalysts opens up a new strategy for preparing supported Ni catalysts for industry applications.

ACKNOWLEDGEMENTS

Correspondence concerning this article should be addressed to X. Liang at liangxin@mst.edu.

LITERATURE CITED

1.   Wood DA, Nwaoha C, Towler BF. Gas-to-liquids (GTL): A review of an industry offering several routes for monetizing natural gas. *Journal of Natural Gas Science and Engineering.* 2012;9:196-208.

2.   Rostrup-Nielsen JR, Sehested J, Nørskov JK. Hydrogen and synthesis gas by steam-and CO_2 reforming. *Advances in catalysis.* 2002;47:65-139.

3.   Zhou W, Chen J-G, Fang K-G, Sun Y-H. The deactivation of Co/SiO_2 catalyst for Fischer–Tropsch synthesis at different ratios of H_2 to CO. *Fuel Processing Technology.* 2006;87(7):609-616.

4.   Dry ME. The Fischer–Tropsch process: 1950–2000. *Catalysis Today.* 2002;71(3-4):227-241.

5.   Barroso-Quiroga MM, Castro-Luna AE. Catalytic activity and effect of modifiers on Ni-based catalysts for the dry reforming of methane. *International Journal of Hydrogen Energy.* 2010;35(11):6052-6056.

6.   Therdthianwong S, Therdthianwong A, Siangchin C, Yongprapat S. Synthesis gas production from dry reforming of methane over Ni/Al_2O_3 stabilized by ZrO_2. *International Journal of Hydrogen Energy.* 2008;33(3):991-999.

7. Pompeo F, Nichio NN, Gonzalez MG, Montes M. Characterization of Ni/SiO$_2$ and Ni/Li-SiO$_2$ catalysts for methane dry reforming. *Catalysis Today.* 2005;107-08:856-862.

8. Chen YG, Ren J. Conversion of methane and carbon dioxide into synthesis gas over alumina-supported nickel catalysts. Effect of Ni-Al$_2$O$_3$ interactions. *Catalysis Letters.* 1994;29(1-2):39-48.

9. Hou ZY, Yokota O, Tanaka T, Yashima T. Investigation of CH4 reforming with CO$_2$ on meso-porous Al$_2$O$_3$-supported Ni catalyst. *Catalysis Letters.* 2003;89(1-2):121-127.

10. Gould TD, Izar A, Weimer AW, Falconer JL, Medlin JW. Stabilizing Ni catalysts by molecular layer deposition for harsh, dry reforming conditions. *ACS Catalysis.* 2014;4(8):2714-2717.

11. Shang ZY, Li SG, Li L, Liu GZ, Liang XH. Highly Active and Stable Alumina Supported Nickel Nanoparticle Catalysts for Dry Reforming of Methane. *Applied Catalysis B: Environmental.* 2017;201:302-309.

12. Santos PS, Santos HS, Toledo SP. Standard transition aluminas. Electron microscopy studies. *Materials Research.* 2000;3(4):104-114.

13. Dynys FW, Halloran JW. Alpha alumina formation in alum‐derived gamma alumina. *Journal of the American Ceramic Society.* 1982;65(9):442-448.

14. Al-Megeren H, Xiao T. *Natural Gas Dual Reforming Catalyst and Process:* INTECH Open Access Publisher; 2012.

15. Li JS, Wang LJ, Hao YX, Liu XD, Sun XY. Preparation and characterization of Al$_2$O$_3$ hollow fiber membranes. *Journal of membrane science.* 2005;256(1-2):1-6.

16. Pan XL, Xiong GX, Sheng SS, Stroh N, Brunner H. Thin dense Pd membranes supported on α-Al$_2$O$_3$ hollow fibers. *Chemical Communications.* 2001(24):2536-2537.

17. Hou ZY, Yokota O, Tanaka T, Yashima T. Characterization of Ca-promoted Ni/α-Al$_2$O$_3$ catalyst for CH4 reforming with CO$_2$. *Applied Catalysis A: General.* 2003;253(2):381-387.

18. Shi ZZ, Zhang YT, Cai C, Zhang C, Gu XH. Preparation and characterization of α-Al$_2$O$_3$ hollow fiber membranes with four-channel configuration. *Ceramics International.* 2015;41(1):1333-1339.

19. Liang XH, Hakim LF, Zhan GD, et al. Novel processing to produce polymer/ceramic nanocomposites by atomic layer deposition. *Journal of the American Ceramic Society.* 2007;90(1):57-63.

20. Gould TD, Lubers AM, Neltner BT, et al. Synthesis of supported Ni catalysts by atomic layer deposition. *Journal of Catalysis.* 2013;303:9-15.

21. Jiang CJ, Shang ZY, Liang XH. Chemoselective transfer hydrogenation of nitroarenes catalyzed by highly dispersed, supported nickel nanoparticles. *ACS Catalysis.* 2015;5(8):4814-4818.

22. Ertl G, Hierl R, Knözinger H, Thiele N, Urbach HP. XPS study of copper aluminate catalysts. *Applications of Surface Science.* 1980;5(1):49-64.

23. Salvati Jr L, Makovsky LE, Stencel JM, Brown FR, Hercules DM. Surface spectroscopic study of tungsten-alumina catalysts using X-ray photoelectron, ion scattering, and Raman spectroscopies. *The Journal of Physical Chemistry.* 1981;85(24):3700-3707.

24. Mansour AN. Characterization of NiO by XPS. *Surface Science Spectra.* 1994;3(3):231-238.

25. Molina R, Poncelet G. α-Alumina-supported nickel catalysts prepared with nickel acetylacetonate. 2. A study of the thermolysis of the metal precursor. *The Journal of Physical Chemistry B.* 1999;103(51):11290-11296.

26. Gao Z, Dong M, Wang GZ, et al. Multiply Confined Nickel Nanocatalysts Produced by Atomic Layer Deposition for Hydrogenation Reactions. *Angewandte Chemie International Edition.* 2015;54(31):9006-9010.

27. Liu CJ, Ye JY, Jiang JJ, Pan YX. Progresses in the Preparation of Coke Resistant Ni‐Based Catalyst for Steam and CO$_2$ Reforming of Methane. *ChemCatChem.* 2011;3(3):529-541.

28. Groner MD, Fabreguette FH, Elam JW, George SM. Low-temperature Al$_2$O$_3$ atomic layer deposition. *Chemistry of Materials.* 2004;16(4):639-645.

29.   Guo JJ, Lou H, Zhao H, Chai DF, Zheng XM. Dry reforming of methane over nickel catalysts supported on magnesium aluminate spinels. *Applied Catalysis A: General*. 2004;273(1-2):75-82.

30.   Baktash E, Littlewood P, Schomacker R, Thomas A, Stair PC. Alumina coated nickel nanoparticles as a highly active catalyst for dry reforming of methane. *Applied Catalysis B: Environmental.* 2015;179:122-127.

SECTION

2. CONCLUSIONS AND FUTURE WORK

2.1. CONCLUSIONS

In this dissertation, ALD/MLD was employed to synthesize size-selective catalysts and supported Ni catalysts. Ultra-thin porous alumina shells were deposited on Pt/SiO_2 catalyst by oxidation of alucone MLD films to synthesize a novel size-selective catalyst. The thickness of porous alumina shells can be precisely controlled in nanometer scale by MLD. The average pore size of the porous shells was 0.6 nm. The porous shells could allow smaller molecules to pass through and access to the active sites, but prevent large molecules from accessing the active sites. The size-selective effect of the porous alumina shells was verified by liquid-phase hydrogenation of n-hexene and cis-cyclooctene, in which n-hexene has a smaller molecule size as compared to cis-cyclooctene. The catalyst showed high selectivity in catalyzing hydrogenation of olefins. Importantly, the mass diffusion limitation was not significant due to the ultra-thin films. The success of depositing porous shells by oxidation of hybrid films deposited by MLD opens up a new method for preparing size-selective catalysts. However, the activity decreased after the deposition of porous shells due to the contact areas between the active sites and porous shells.

An improved size-selective catalyst with an ultra-thin porous shell and gaps between metal nanoparticles and porous shells was synthesized. A sacrificial layer of thiol-SAMs were selectively deposited on the surface of metal nanoparticles before the alucone

MLD films were deposited on catalyst surface. The thiol-SAMs and organic components in the alucone MLD films were removed by oxidation in air, and gaps and porous structures in the MLD films were formed. The selectivity and activity of the catalysts were tested by hydrogenation reactions of n-hexene and cis-cyclooctene. The new nanostructured catalyst showed high selectivity in catalyzing hydrogenation of olefins and higher catalytic activity as compared to that of the catalyst without gaps. Both size-selective catalysts with and without gaps were analyzed by CO-chemisorption to determine the Pt dispersion. The catalyst with gaps showed higher Pt dispersion as compared to the catalyst without gaps, which supported the conclusion that the introduction of gaps could effectively reduce the contact areas between the active sites and porous shells. The success of this gap-forming strategy provides a new method for retaining the activity of size-selective catalysts, especially those structures consisting of a metal core and a porous shell.

Supported Ni nanoparticles were synthesized by depositing Ni nanoparticles on different substrates by ALD. Highly dispersed Ni nanoparticles (average particle size: 2.4 nm) were deposited on porous silica gel particles. The synthesized Ni/silica gel catalysts can activate hydrazine hydrate as a reducing agent in the transfer hydrogenation of aromatic nitro compounds into the corresponding aromatic amines with high yield. The synthesized Ni/silica gel catalyst showed much higher activity as compared to some other catalysts prepared by conventional liquid-phase based methods. The Ni/silica gel catalyst can be recycled from the solution by a magnet since the catalyst was highly magnetic. The recycled catalyst was employed to catalyze hydrogenation of nitroarenes and still showed

high yield to corresponding aromatic amines. This work has extended the utility of a readily available catalyst (Ni/SiO_2) toward new applications in catalysis and organic chemistry.

Ni nanoparticles were also deposited on both nonporous gamma-alumina nanoparticles and porous gamma-alumina particles by ALD. The ALD synthesized porous γ-Al_2O_3 supported Ni catalyst showed both high activity and stability in catalyzing DRM reaction. The porous alumina supported catalyst showed better performance than nonporous alumina supported catalyst. $NiAl_2O_4$ spinel was formed after Ni nanoparticles were deposited on the porous γ-Al_2O_3 support by ALD, which were reduced to metallic Ni at 850 °C under the reductive atmosphere of DRM reaction, but could not be reduced by hydrogen alone at 850 °C. The formation of $NiAl_2O_4$ spinel greatly increased the catalyst stability due to the strong interaction between the Ni nanoparticles and porous γ-Al_2O_3 support and the reduction of $NiAl_2O_4$ greatly increased the catalyst activity.

Ni nanoparticles were also deposited on alpha-alumina NPs and alpha-alumina hollow fibers with four-channel configuration by ALD. Less $NiAl_2O_4$ spinel was formed on alpha-alumina NPs by ALD, as compared to the Ni NPs on γ-Al_2O_3 support by ALD. The synthesized catalysts were employed for DRM reaction and showed excellent performance. To increase the Ni nanoparticles and alpha-alumina support interaction, different thicknesses of ultra-thin alumina films were deposited on the Ni/hollow fiber catalyst by ALD, and the catalyst activity and stability were both improved by the overcoating of alumina ALD films. Among the overcoated catalysts, the catalyst with 5 cycles of alumina ALD showed the best performance. It is believed that the overcoating of

alumina ALD films on the catalyst increased the interaction between the Ni nanoparticles and the support.

2.2. FUTURE WORK

For the size-selective catalyst, the size-selective effects can be realized by the porous shells, and the contact areas between the active sites and porous shells can be reduced a lot by introducing gaps between them to maintain a high catalytic activity. However, this porous shell may not suitable for some other reactants since the average pore size is only 0.6 nm. In order to solve this problem, different MLD precursors can be employed for the deposition of hybrid films, since the pore size of the formed porous shells is related to the carbon chain length in the precursors. The relationship between the average pore size and carbon chain length in the precursors can be investigated to design porous shells for application of different reactions. In addition, the formed porous alumina shells are not stable in water, which limits the application of this porous shell. Porous titania shells can be employed for such size-selective reactions due to its better stability in water.

For DRM reaction, even though the synthesized supported Ni nanoparticles catalyst showed excellent performance in catalyzing the DRM reaction, different methods still can be employed to further improve the catalyst performance. Bimetallic catalyst system is one important way to improve the catalyst performance. Different bimetallic systems (e.g., Ni-Co, Ni-Pt, Ni-Rh, and Ni-Pd) catalysts can be employed for DRM reaction. Different methods, such as impregnation method and ALD, can also be employed to synthesize the

bimetallic catalysts. Catalysts with different metal ratios should be investigated to figure

out the optimized metal ratios. In addition, different promoters (e.g., MgO, CaO, ZrO_2,

La_2O_3, and CeO_2) can be applied on the supported Ni catalysts. The influence of the amount

of promoters on catalyst performance should also be investigated to find out an optimized

Ni-promoter ratio.

BIBLIOGRAPHY

1.	Goodman, C. H. L.; Pessa, M. V., *Journal of Applied Physics* **1986,** 60, (3), R65-R82.

2.	Niinistö, L., *Current Opinion in Solid State and Materials Science* **1998,** 3, (2), 147-152.

3.	Suntola, T., *Thin Solid Films* **1992,** 216, (1), 84-89.

4.	Suntola, T.; Antson, J., Method for producing compound thin films. Patent, U. S.,**1977**.

5.	Aleskovskii, V.; Kol'tsov, S. In *Some characteristics of molecular layering reactions*, Abstract of Scientific and Technical Conference, Goskhimizdat, Leningrad, **1965**.

6.	Hakim, L. F.; McCormick, J. A.; Zhan, G. D.; Weimer, A. W.; Li, P.; George, S. M., *Journal of the American Ceramic Society* **2006,** 89, (10), 3070-3075.

7.	George, S. M.; Ott, A. W.; Klaus, J. W., *The Journal of Physical Chemistry* **1996,** 100, (31), 13121-13131.

8.	Jung, Y. S.; Cavanagh, A. S.; Riley, L. A.; Kang, S. H.; Dillon, A. C.; Groner, M. D.; George, S. M.; Lee, S. H., *Advanced Materials* **2010,** 22, (19), 2172-2176.

9.	Jung, Y. S.; Cavanagh, A. S.; Dillon, A. C.; Groner, M. D.; George, S. M.; Lee, S. H., *Journal of The Electrochemical Society* **2010,** 157, (1), A75-A81.

10.	Shim, J. H.; Chao, C. C.; Huang, H.; Prinz, F. B., *Chemistry of Materials* **2007,** 19, (15), 3850-3854.

11.	Chao, C. C.; Hsu, C. M.; Cui, Y.; Prinz, F. B., *ACS nano* **2011,** 5, (7), 5692-5696.

12.	Sneh, O.; Clark-Phelps, R. B.; Londergan, A. R.; Winkler, J.; Seidel, T. E., *Thin solid films* **2002,** 402, (1-2), 248-261.

13.	Kim, H., *Journal of Vacuum Science & Technology B* **2003,** 21, (6), 2231-2261.

14.	Lu, J. L.; Fu, B. S.; Kung, M. C.; Xiao, G. M.; Elam, J. W.; Kung, H. H.; Stair, P. C., *Science* **2012,** 335, (6073), 1205-1208.

15. Li, J. H.; Liang, X. H.; King, D. M.; Jiang, Y. B.; Weimer, A. W., *Applied Catalysis B: Environmental* **2010,** 97, (1-2), 220-226.

16. Riha, S. C.; Klahr, B. M.; Tyo, E. C.; Seifert, S.; Vajda, S.; Pellin, M. J.; Hamann, T. W.; Martinson, A. B. F., *ACS nano* **2013,** 7, (3), 2396-2405.

17. Groner, M. D.; Fabreguette, F. H.; Elam, J. W.; George, S. M., *Chemistry of Materials* **2004,** 16, (4), 639-645.

18. Cameron, M. A.; Gartland, I. P.; Smith, J. A.; Diaz, S. F.; George, S. M., *Langmuir* **2000,** 16, (19), 7435-7444.

19. Stuyven, G.; De Visschere, P.; Hikavyy, A.; Neyts, K., *Journal of crystal growth* **2002,** 234, (4), 690-698.

20. Elam, J. W.; Schuisky, M.; Ferguson, J. D.; George, S. M., *Thin Solid Films* **2003,** 436, (2), 145-156.

21. Klaus, J. W.; Ferro, S. J.; George, S. M., *Thin Solid Films* **2000,** 360, (1-2), 145-153.

22. Aaltonen, T.; Alén, P.; Ritala, M.; Leskelä, M., *Chemical Vapor Deposition* **2003,** 9, (1), 45-49.

23. Aaltonen, T.; Ritala, M.; Sajavaara, T.; Keinonen, J.; Leskelä, M., *Chemistry of materials* **2003,** 15, (9), 1924-1928.

24. Lim, B. S.; Rahtu, A.; Gordon, R. G., *Nature materials* **2003,** 2, (11), 749-754.

25. Elam, J. W.; Zinovev, A. V. V.; Pellin, M. J.; Comstock, D. J.; Hersam, M. C., *ECS Transactions* **2007,** 3, (15), 271-278.

26. Christensen, S. T.; Elam, J. W.; Lee, B.; Feng, Z.; Bedzyk, M. J.; Hersam, M. C., *Chemistry of Materials* **2009,** 21, (3), 516-521.

27. Elam, J. W.; Zinovev, A.; Han, C. Y.; Wang, H. H.; Welp, U.; Hryn, J. N.; Pellin, M. J., *Thin Solid Films* **2006,** 515, (4), 1664-1673.

28. Christensen, S. T.; Elam, J. W.; Rabuffetti, F. A.; Ma, Q.; Weigand, S. J.; Lee, B.; Seifert, S.; Stair, P. C.; Poeppelmeier, K. R.; Hersam, M. C.; Bedzyk, M. J., *small* **2009,** 5, (6), 750-757.

29. Feng, H.; Elam, J. W.; Libera, J. A.; Setthapun, W.; Stair, P. C., *Chemistry of Materials* **2010,** 22, (10), 3133-3142.

30.   Lashdaf, M.; Krause, A. O. I.; Lindblad, M.; Tiitta, A.; Venalainen, T., *Applied Catalysis A: General* **2003,** 241, (1-2), 65-75.

31.   Liang, X. H.; Jiang, C. J., *Journal of Nanoparticle Research* **2013,** 15, (9), 1890.

32.   Hsu, I. J.; Kimmel, Y. C.; Jiang, X. G.; Willis, B. G.; Chen, J. G., *Chemical Communications* **2012,** 48, (7), 1063-1065.

33.   Gould, T. D.; Lubers, A. M.; Neltner, B. T.; Carrier, J. V.; Weimer, A. W.; Falconer, J. L.; Medlin, J. W., *Journal of Catalysis* **2013,** 303, 9-15.

34.   Backman, L. B.; Rautiainen, A.; Lindblad, M.; Krause, A. O. I., *Applied Catalysis A: General* **2009,** 360, (2), 183-191.

35.   Du, Y.; George, S. M., *The Journal of Physical Chemistry C* **2007,** 111, (24), 8509-8517.

36.   Dameron, A. A.; Seghete, D.; Burton, B. B.; Davidson, S. D.; Cavanagh, A. S.; Bertrand, J. A.; George, S. M., *Chemistry of Materials* **2008,** 20, (10), 3315-3326.

37.   Yoshimura, T.; Tatsuura, S.; Sotoyama, W., *Applied Physics Letters* **1991,** 59, (4), 482-484.

38.   Yoshimura, T.; Tatsuura, S.; Sotoyama, W.; Matsuura, A.; Hayano, T., *Applied Physics Letters* **1992,** 60, (3), 268-270.

39.   Shao, H. I.; Umemoto, S.; Kikutani, T.; Okui, N., *Polymer* **1997,** 38, (2), 459-462.

40.   Kim, A.; Filler, M. A.; Kim, S.; Bent, S. F., *Journal of the American Chemical Society* **2005,** 127, (16), 6123-6132.

41.   Lee, J. S.; Lee, Y. J.; Tae, E. L.; Park, Y. S.; Yoon, K. B., *Science* **2003,** 301, (5634), 818-821.

42.   Haq, S.; Richardson, N. V., *The Journal of Physical Chemistry B* **1999,** 103, (25), 5256-5265.

43.   Putkonen, M.; Harjuoja, J.; Sajavaara, T.; Niinistö, L., *Journal of Materials Chemistry* **2007,** 17, (7), 664-669.

44.   Yoshimura, T.; Ito, S.; Nakayama, T.; Matsumoto, K., *Applied Physics Letters* **2007,** 91, (3), 033103.

45.   Adamczyk, N. M.; Dameron, A. A.; George, S. M., *Langmuir* **2008,** 24, (5), 2081-2089.

46. George, S. M.; Yoon, B.; Dameron, A. A., *Accounts of Chemical Research* **2009,** 42, (4), 498-508.

47. Peng, Q.; Gong, B.; VanGundy, R. M.; Parsons, G. N., *Chemistry of Materials* **2009,** 21, (5), 820-830.

48. Yoon, B.; O'Patchen, J. L.; Seghete, D.; Cavanagh, A. S.; George, S. M., *Chemical Vapor Deposition* **2009,** 15, (4‐6), 112-121.

49. Liang, X. H.; Yu, M.; Li, J. H.; Jiang, Y. B.; Weimer, A. W., *Chemical Communications* **2009**, (46), 7140-7142.

50. Gong, B.; Peng, Q.; Parsons, G. N., *The Journal of Physical Chemistry B* **2011,** 115, (19), 5930-5938.

51. Liang, X. H.; Li, J. H.; Yu, M.; McMurray, C. N.; Falconer, J. L.; Weimer, A. W., *ACS Catalysis* **2011,** 1, (10), 1162-1165.

52. Gould, T. D.; Izar, A.; Weimer, A. W.; Falconer, J. L.; Medlin, J. W., *ACS Catalysis* **2014,** 4, (8), 2714-2717.

53. Young, L. B.; Butter, S. A.; Kaeding, W. W., *Journal of Catalysis* **1982,** 76, (2), 418-432.

54. Cook, B. R.; Reinert, T. J.; Suslick, K. S., *Journal of the American Chemical Society* **1986,** 108, (23), 7281-7286.

55. Lee, G. S.; Maj, J. J.; Rocke, S. C.; Garces, J. M., *Catalysis Letters* **1989,** 2, (4), 243-247.

56. Tada, M.; Sasaki, T.; Iwasawa, Y., *The Journal of Physical Chemistry B* **2004,** 108, (9), 2918-2930.

57. Weisz, P. B.; Frilette, V. J., *The Journal of Physical Chemistry* **1960,** 64, (3), 382-382.

58. Xu, W. Q.; Yin, Y. G.; Suib, S. L.; O'Young, C. L., *The Journal of Physical Chemistry* **1995,** 99, (2), 758-765.

59. Chen, N. Y.; Garwood, W. E., *Journal of Catalysis* **1978,** 52, (3), 453-458.

60. Yang, H. Q.; Chong, Y. Z.; Li, X. K.; Ge, H.; Fan, W. B.; Wang, J. G., *Journal of Materials Chemistry* **2012,** 22, (18), 9069-9076.

61.   Corma, A.; Das, D.; García, H.; Leyva, A., *Journal of Catalysis* **2005,** 229, (2), 322-331.

62.   Mori, K.; Hara, T.; Mizugaki, T.; Ebitani, K.; Kaneda, K., *Journal of the American Chemical Society* **2004,** 126, (34), 10657-10666.

63.   Choi, E.; Lee, C.; Na, Y.; Chang, S., *Organic Letters* **2002,** 4, (14), 2369-2371.

64.   Collier, P.; Golunski, S.; Malde, C.; Breen, J.; Burch, R., *Journal of the American Chemical Society* **2003,** 125, (41), 12414-12415.

65.   Marshall, S. T.; O'Brien, M.; Oetter, B.; Corpuz, A.; Richards, R. M.; Schwartz, D. K.; Medlin, J. W., *Nature materials* **2010,** 9, (10), 853-858.

66.   Kahsar, K. R.; Schwartz, D. K.; Medlin, J. W., *ACS Catalysis* **2013,** 3, (9), 2041-2044.

67.   Sedmak, G.; Hočevar, S.; Levec, J., *Journal of Catalysis* **2003,** 213, (2), 135-150.

68.   Thomas, J. M.; Raja, R.; Lewis, D. W., *Angewandte Chemie International Edition* **2005,** 44, (40), 6456-6482.

69.   Joo, S. H.; Park, J. Y.; Tsung, C. K.; Yamada, Y.; Yang, P. D.; Somorjai, G. A., *Nature Materials* **2009,** 8, (2), 126-131.

70.   Park, J. N.; Forman, A. J.; Tang, W.; Cheng, J. H.; Hu, Y. S.; Lin, H. F.; McFarland, E. W., *Small* **2008,** 4, (10), 1694-1697.

71.   Ge, J. P.; Zhang, Q.; Zhang, T. R.; Yin, Y. D., *Angewandte Chemie International Edition* **2008,** 47, (46), 8924-8928.

72.   Zhang, Z. W.; Zhou, Y. M.; Zhang, Y. W.; Sheng, X. L.; Zhou, S. J.; Xiang, S. M., *RSC Advances* **2014,** 4, (75), 40078-40084.

73.   Xu, Y.; Ma, J. Q.; Xu, Y. F.; Xu, L.; Xu, L.; Li, H. X.; Li, H., *RSC Advances* **2013,** 3, (3), 851-858.

74.   Forman, A. J.; Park, J. N.; Tang, W.; Hu, Y. S.; Stucky, G. D.; McFarland, E. W., *ChemCatChem* **2010,** 2, (10), 1318-1324.

75.   Nishiyama, N.; Ichioka, K.; Park, D. H.; Egashira, Y.; Ueyama, K.; Gora, L.; Zhu, W. D.; Kapteijn, F.; Moulijn, J. A., *Industrial & Engineering Chemistry Research* **2004,** 43, (5), 1211-1215.

76. Højholt, K. T.; Laursen, A. B.; Kegnæs, S.; Christensen, C. H., *Topics in Catalysis* **2011,** 54, (16-18), 1026-1033.

77. Mielby, J.; Abildstrøm, J. O.; Wang, F.; Kasama, T.; Weidenthaler, C.; Kegnaes, S., *Angewandte Chemie International Edition* **2014,** 53, (46), 12513-12516.

78. Lu, G.; Li, S. Z.; Guo, Z.; Farha, O. K.; Hauser, B. G.; Qi, X. Y.; Wang, Y.; Wang, X.; Han, S. Y.; Liu, X. G.; DuChene, J. S.; Zhang, H.; Zhang, Q. C.; Chen, X. D.; Ma, J.; Loo, S. C. J.; Wei, W. D.; Yang, Y. H.; Hupp, J. T.; Huo, F. W., *Nature Chemistry* **2012,** 4, (4), 310-316.

79. Li, S. W.; Boucheron, T.; Tuel, A.; Farrusseng, D.; Meunier, F., *Chemical Communications* **2014,** 50, (15), 1824-1826.

80. Li, S. W.; Tuel, A.; Laprune, D.; Meunier, F.; Farrusseng, D., *Chemistry of Materials* **2015,** 27, (1), 276-282.

81. Yu, C. Z.; Liu, B.; Hu, L. Q., *The Journal of Organic Chemistry* **2001,** 66, (3), 919-924.

82. Saha, A.; Ranu, B., *The Journal of Organic Chemistry* **2008,** 73, (17), 6867-6870.

83. Lou, X. B.; He, L.; Qian, Y.; Liu, Y. M.; Cao, Y.; Fan, K. N., *Advanced Synthesis & Catalysis* **2011,** 353, (2‐3), 281-286.

84. Cardenas-Lizana, F.; Gomez-Quero, S.; Keane, M. A., *Catalysis Communications* **2008,** 9, (3), 475-481.

85. Shimizu, K.-i.; Miyamoto, Y.; Satsuma, A., *Journal of Catalysis* **2010,** 270, (1), 86-94.

86. Dey, R.; Mukherjee, N.; Ahammed, S.; Ranu, B. C., *Chemical Communications* **2012,** 48, (64), 7982-7984.

87. Petkar, D. R.; Kadu, B. S.; Chikate, R. C., *RSC Advances* **2014,** 4, (16), 8004-8010.

88. Wen, H. L.; Yao, K. S.; Zhang, Y. D.; Zhou, Z. M.; Kirschning, A., *Catalysis Communications* **2009,** 10, (8), 1207-1211.

89. Antonetti, C.; Oubenali, M.; Galletti, A. M. R.; Serp, P.; Vannucci, G., *Applied Catalysis A: General* **2012,** 421, 99-107.

90. Lu, Y. M.; Zhu, H. Z.; Li, W. G.; Hu, B.; Yu, S. H., *Journal of Materials Chemistry A* **2013,** 1, (11), 3783-3788.

91.   Mahata, N.; Cunha, A. F.; Orfao, J. J. M.; Figueiredo, J. L., *Applied Catalysis A: General* **2008,** 351, (2), 204-209.

92.   Zhou, W.; Chen, J. G.; Fang, K. G.; Sun, Y. H., *Fuel Processing Technology* **2006,** 87, (7), 609-616.

93.   Dry, M. E., *Catalysis Today* **2002,** 71, (3-4), 227-241.

94.   Wang, H. Y.; Ruckenstein, E., *Applied Catalysis A: General* **2000,** 204, (1), 143-152.

95.   Wang, R.; Xu, H. Y.; Liu, X. B.; Ge, Q. J.; Li, W. Z., *Applied Catalysis A: General* **2006,** 305, (2), 204-210.

96.   O'Connor, A. M.; Schuurman, Y.; Ross, J. R. H.; Mirodatos, C., *Catalysis Today* **2006,** 115, (1-4), 191-198.

97.   Damyanova, S.; Pawelec, B.; Arishtirova, K.; Martinez Huerta, M. V.; Fierro, J. L. G., *Applied Catalysis B: Environmental* **2009,** 89, (1-2), 149-159.

98.   Wisniewski, M.; Boréave, A.; Gélin, P., *Catalysis Communications* **2005,** 6, (9), 596-600.

99.   Schulz, P. G.; Gonzalez, M. G.; Quincoces, C. E.; Gigola, C. E., *Industrial & Engineering Chemistry Research* **2005,** 44, (24), 9020-9029.

100.   Carrara, C.; Munera, J.; Lombardo, E. A.; Cornaglia, L. M., *Topics in Catalysis* **2008,** 51, (1-4), 98-106.

101.   Chen, J. X.; Yao, C. C.; Zhao, Y. Q.; Jia, P. H., *International Journal of Hydrogen Energy* **2010,** 35, (4), 1630-1642.

102.   Barroso-Quiroga, M. M.; Castro-Luna, A. E., *International Journal of Hydrogen Energy* **2010,** 35, (11), 6052-6056.

103.   Therdthianwong, S.; Therdthianwong, A.; Siangchin, C.; Yongprapat, S., *International Journal of Hydrogen Energy* **2008,** 33, (3), 991-999.

104.   Rostrupnielsen, J. R.; Hansen, J. H. B., *Journal of Catalysis* **1993,** 144, (1), 38-49.

105.   Hou, Z. Y.; Chen, P.; Fang, H. L.; Zheng, X. M.; Yashima, T., *International Journal of Hydrogen Energy* **2006,** 31, (5), 555-561.

106.   Pompeo, F.; Nichio, N. N.; González, M. G.; Montes, M., *Catalysis Today* **2005,** 107-08, 856-862.

107. Rostrup-Nielsen, J. R.; Sehested, J.; Nørskov, J. K., *Advances in Catalysis* **2002,** 47, 65-139.

108. Bengaard, H. S.; Nørskov, J. K.; Sehested, J.; Clausen, B. S.; Nielsen, L. P.; Molenbroek, A. M.; Rostrup-Nielsen, J. R., *Journal of Catalysis* **2002,** 209, (2), 365-384.

109. Zhang, C. X.; Yue, H. R.; Huang, Z. Q.; Li, S. R.; Wu, G. W.; Ma, X. B.; Gong, J. L., *ACS Sustainable Chemistry & Engineering* **2013,** 1, (1), 161-173.

110. Liu, C. J.; Ye, J. Y.; Jiang, J. J.; Pan, Y. X., *ChemCatChem* **2011,** 3, (3), 529-541.

111. Pan, Y. X.; Liu, C. J.; Shi, P., *Journal of Power Sources* **2008,** 176, (1), 46-53.

112. Rezaei, M.; Alavi, S. M.; Sahebdelfar, S.; Bai, P.; Liu, X. M.; Yan, Z. F., *Applied Catalysis B: Environmental* **2008,** 77, (3-4), 346-354.

113. Roh, H. S.; Jun, K. W., *Catalysis Surveys from Asia* **2008,** 12, (4), 239-252.

114. Santos, P. S.; Santos, H. S.; Toledo, S. P., *Materials Research* **2000,** 3, (4), 104-114.

115. Dynys, F. W.; Halloran, J. W., *Journal of the American Ceramic Society* **1982,** 65, (9), 442-448.

116. Al-Megeren, H.; Xiao, T. C., *Natural Gas Dual Reforming Catalyst and Process*. INTECH Open Access Publisher: **2012**.

117. Shi, Z. Z.; Zhang, Y. T.; Cai, C.; Zhang, C.; Gu, X. H., *Ceramics International* **2015,** 41, (1), 1333-1339.

VITA

The author, Zeyu Shang was born in Inner Mongolia, China. He entered Beijing University of Chemical Technology, China in 2008. He received his B.E degree with a major in Chemical Engineering and Technology from Beijing University of Chemical Technology in June 2012. In August 2012, he came to the USA and attended Missouri University of Science & Technology. He received a Doctor of Philosophy degree in Chemical Engineering from Missouri University of Science and Technology in December 2017.